CHAPTER VI

ELECTROSPUN MEH-PPV:PCL NANOFIBERS FOR TISSUE ENGINEERING APPLICATIONS

The current chapter epitomized the synergistic effect of nanofiber feature, surface functionalization of electrospun Poly[2-methoxy-5-(2-ethylhexyloxy)-1,4-phenylenevinylene] (MEH-PPV) based materials and electrical stimulation in neuronal growth for potential application in neural tissue engineering. Herein, the synthesis and optimization of electrically conductive, porous, mechanically strong and bioactive MEH-PPV:PCL nanofibers with blended form with variation in the volume ratio of the constituents by simple electrospinning process and core-sheath morphology with variation in diameter with varying flow rate by coaxial electrospinning along with post-synthesis surface functionalization using APTES and 1,6-Hexanediamine in order to incorporate amine functionality on the surface. The detailed physico-chemical characterization of all the electrsopun meshes have been carried out with the help of SEM, TEM, XRD,TGA, I-V measurement, FT-IR and XPS. The biological characterization has been carried out with the help of Hemolysis activity assay, MTS proliferation assy with 3T3 fibroblasts and a neuronal model rat PC12 cell line, beta (III) tubulin immunochemistry and cell adhesion test by SEM. Electrical stimulation of PC12 cells has been accommplished to explore the potential of these materials in neural tissue engineering.

6.1 Introduction

Neural regeneration following injury remains a significant challenge with major implications for patient quality of life. Complications associated with damage to sensory and motor neural pathways may result in severe pain and malfunction of organs including the digestive tract, heart and sex organs [251]. Current clinical treatments for peripheral nerve injury are surgical end to end anastomoses and autologous nerve grafts. There is no effective treatment for damage to the central

nervous system (CNS) or for absolute nerve tissue regeneration [418]. There are several disadvantages to autografting and allografting, including loss of function at the donor site, mismatch of nerve cable dimensions between the donor graft and recipient nerve, and the need for multiple surgeries [418-420]. Thus, at present there is no universally accepted treatment available for nerve regeneration and in the majority of cases it is still not possible. Neuronal repair stands out among other tissue repair strategies due to the anatomical and functional complexity of the nervous system, and the inefficiency of conventional repair approaches [421, 422]. In fact, satisfactory outcomes are usually limited to relatively minor injuries to the peripheral nervous system.

Electroactive polymeric biomaterial scaffolds offer the potential for a new approach to neural stimulation using their conductive properties to stimulate directive, rapid axonal growth for nerve regeneration [120, 196, 423-425]. With the advent of nanotechnology and the use of electrospinning techniques, biomaterial scaffolds may be synthesized as non-woven, three dimensional, porous and nanofibrous scaffolds with suitable mechanical properties to mimic the native extracellular matrix (ECM) [180, 422, 426]. In addition, it is possible to develop unique co-polymer blends to best stimulate enhanced neural growth patterns for neural tissue engineering applications. Bioelectricity plays an integral role in maintaining normal biological functions via cranial, spinal and peripheral neural networks which signal for example muscle contraction and wound healing in bone, cartilage, skin, connective tissue [120, 418, 427]. Specifically, the electrical signal in the peripheral nervous system accelerates axonal regeneration and elongation and enhances expression of neurotrophic factors and the biological activity of Schwann cells [196, 251]. In this regard, conducting polymers (CPs) offer excellent control over the level and duration of the electrical stimulus [418, 423]. CPs have a higher charge injection limit with improved charge-discharge characteristics leading to enhanced charge transportation to cells for membrane depolarization. This, in turn, can improve the adhesion and proliferation of nerve cells including the promotion of axonal growth [170, 327]. Additionally, CPs possess very good electrical and optical properties, a high conductivity/weight ratio and can be made biocompatible, biodegradable and porous [139, 196, 429]. The chemical, electrical and physical properties of CPs can be altered to suit specific applications by incorporating different functionality even after synthesis. The beneficial effect of electrical stimulation (ES) on neurite formation and neurite

outgrowth was shown using PPy, PAni and PEDOT with PC12 cells, retinal ganglion cell (RGC), dorsal root ganglion (DRG), and nerve stem cells [196]. However, ES of cells using the polymers other than PPy is limited. One of the major problems associated with these polymers is poor solubility, which often challenges to fabricate nanofibrous biomaterial scaffold. Within this study, we introduce a new CP, poly[2-methoxy-5-(20-ethyl-hexyloxy)-1,4-phenylene vinylene] (MEH-PPV) into the tissue engineering research to fabricate conductive nanofibrous biomaterial scaffold [167]. MEH-PPV has not been assessed for tissue engineering applications before, although it offers an interesting property for biological application since it allows the immobilization of biomolecules due to its high density holes-traps [73]. MEH-PPV is a p-type semiconducting polymer that has low conductivity due to its low hole and electron mobilities [73, 81-83], and is currently used in electronic applications such as LEDs [56-58], and photovoltaic cells [64]. However, suitable doping can improve its conductivity for desired applications. For example, Shin Sakiyama *et al.* demonstrated remarkable improvement in the conductivity of MEH-PPV using $FeCl_3$ (p-type dopant) and Cs_2CO_3 (n-type dopant) [81-83]. Despite its better solubility in common organic solvent when compared to the other CPs discussed above, direct electrospinning of MEH-PPV to a uniformly distributed, one-dimensional nanofiber free from bead formation is difficult [431]. Blending with other natural or synthetic polymers that are biocompatible, biodegradable and easily electrospinnable may be a means to overcome this limitation. The aliphatic linear polyester, polycaprolactone (PCL) is a potential candidate, with attractive electrospinnability due to its good rheological and viscoelastic properties [432]. Electrospun PCL scaffolds have already been widely studied for various tissue engineering applications owing to its biocompatibility, biodegradability and mechanical properties [433].

Furthermore, the cell attachment on the biomaterial scaffold is one of the prerequisites for normal cellular functions for tissue engineering applications [233, 234, 434]. To address the poor surface hydrophilicity of CPs, their surfaces were modified with cell adhesive biomolecules such as fibronectin, laminin, collagen, RGD peptide etc. to impart bioactivity [188, 401, 435]. Unfortunately, these surface modification processes are costly and complex involving multiple conjugation steps. Therefore, an easy and inexpensive way is highly desirable to overcome these demerits, which does not need additional biomolecule treatment for cell adhesion. Surface amination may be an attractive option to achieve positively charged surface

under physiological conditions and thereby, enable the biomaterial surface to interact electrostatically with the negatively charged cell surface for permitting cell adhesion [436]. Besides, amine can also interact with the cell surface proteins through amide bond formation [437-439].

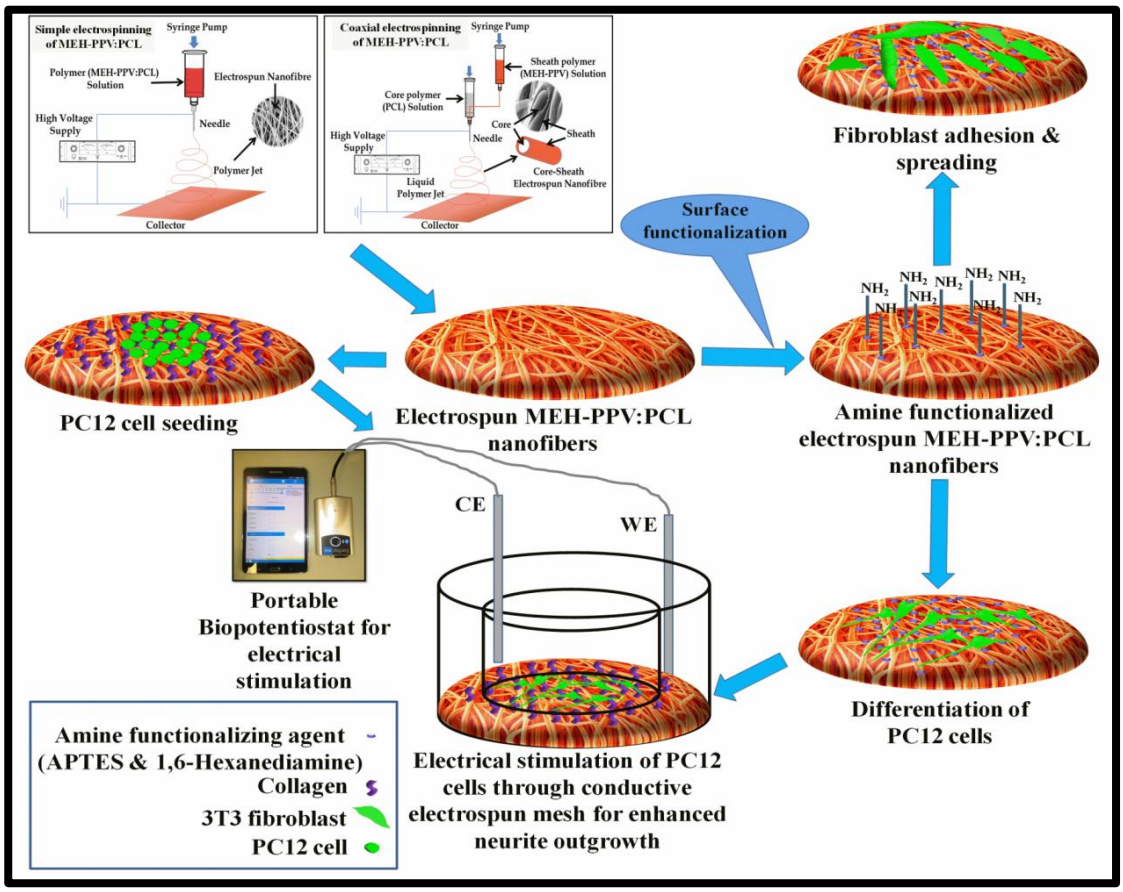

Figure 6.1. Schematic illustration of simple and coaxial electrospinning of MEH-PPV:PCL nanofibers in blended form and core-sheath morphology along surface amination by post-surface functionalization by APTES and 1,6-hexanediamine for 3T3 fibroblasts adhesion and spreading and neuronal growth of differentiated PC12 cells under electrical stimulation.

In the present study, we report for the first time the electrospinning of a blend of $FeCl_3$ doped MEH-PPV with PCL and an investigation of the impact of various composition ratios on electrospun fiber physical, chemical and biological properties. Here, we also report the coaxial electrospinning of conductive core-sheath nanofibers of PCL (core) and MEH-PPV (sheath) at different flow rates to obtain a more conductive scaffold for effective electrical stimulation of cells. Surface

functionalization of the electroactive biomaterials with amino group may replace the need of ECM proteins like collagen, fibronectin, laminin etc. to interact with the integrin proteins on the cell surface for necessary cell-biomaterial interactions. The rationale behind this approach is the favorable interaction between the amino ($-NH_2$) groups on surface functionalized biomaterial and the carboxyl (COOH) terminals of the integrin proteins on the cell surface through the formation of amide bonds [437-439]. In order to functionalize the surface of the electroactive biomaterial, 3-aminopropyltriethoxysilane (APTES) and 1,6-Hexanediamine are used. APTES and 1,6-Hexanediamine are commonly used in biomedical applications due to their simplistic structure and minimal cost for biomolecule immobilization [440-443]. The aim of this study is to investigate the combined effect of nanofiber structure, surface functionalization and electrical stimulation through these electrospun conductive nanofiber meshes on neurite formation and neurite outgrowth using PC12 cells. The flowchart of the present research is shown with the help of a schematic illustration in **Figure 6.1**. If successful MEH-PPV based scaffolds could ultimately be used to design nerve guidance channels and bridge the gap between two damaged nerves.

6.2 Physicochemical characterization

6.2.1 Electron microscopy

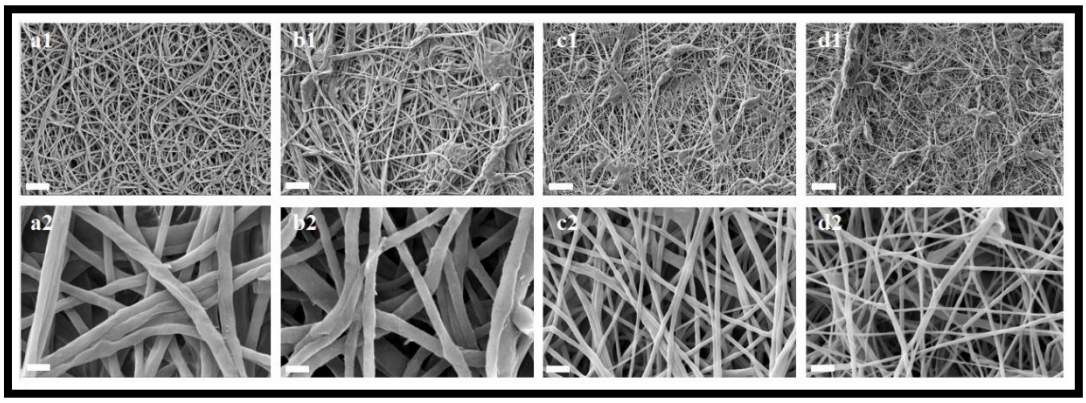

Figure 6.2. Scanning electron micrographs of electrospun nanofibers prepared by simple electrospinning of blend of MEH-PPV and PCL at various volume ratios. a1 & a2: SEN1 (20:80), b1 & b2: SEN2 (40:60), c1 & c2: SEN3 (50:50) and d1 & d2: SEN4 (60:40). Suffix '1' and '2' stand for magnification at 5 K and 50 K, respectively. Scale bar: 4 μm (a1, b1, c1 & d1) and 400 nm (a2, b2, c2 & d2).

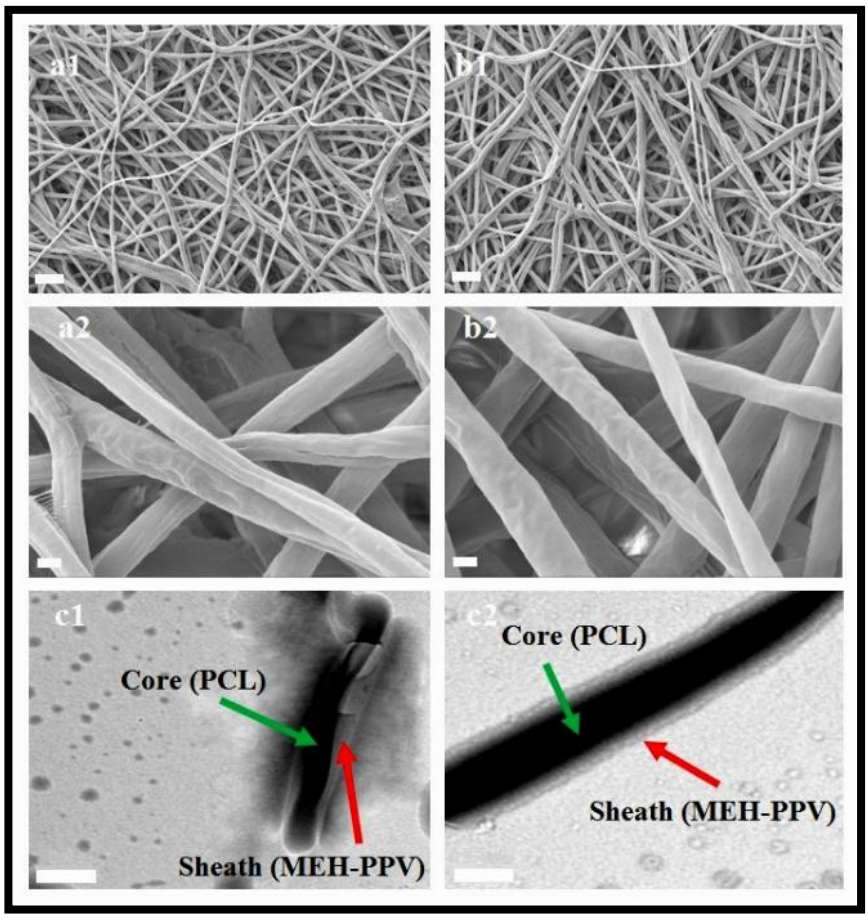

Figure 6.3. Scanning electron micrographs of CSN1 (a1 & a2) and CSN2 (b1 & b2), acquired at two different magnifications of 5 K and 50 K. Transmission electron micrographs of CSN1 (c1) and CSN2 (c2) showing the formation of nanofibers with core-sheath morphology. Scale bar = 4 μm (a1 & b1), 300 nm (a2 & b2) and 500 nm (c1 & c2).

Scanning electron micrographs confirm the formation of nanofibers of MEH-PPV:PCL by a simple electrospinning method [**Figure 6.2**]. The electrospun meshes obtained by varying MEH-PPV to PCL volume ratios of 20:80, 40:60, 50:50 and 60:40 were named as SEN1, SEN2, SEN3 and SEN4, respectively. The core-sheath fibres electrospun at a flow rate of 0.6 mL/h and 1mL/h were denoted as CSN1 and CSN2. The diameter of nanofibers produced by simple electrospinning method varied with the variation of the volume ratio of MEH-PPV to PCL. SEN1, having the lowest volume percent of MEH-PPV to PCL (20:80 v/v) had the largest diameter of 324 ± 70 nm. The diameters of SEN2 (40:60 v/v), SEN3 (50:50 v/v) and SEN4 (60:40) were

measured to be 280 ± 82 nm, 198 ± 30 nm and 132 ± 53 nm using Carl Zeiss Software. The scanning electron micrographs of electrospun nanofibers prepared by a simple electrospinning process further confirm an increase in bead formation with an increase in MEH-PPV concentration due to its poor electrospinning ability. However, SEN1 and core-sheath nanofibers were free from beaded fibres. It is believed that the poor electrospinning ability of MEH-PPV, may be the reason for the decrease in fibre diameter with increase in MEH-PPV concentration [444, 445]. The nanofibers produced by a core-sheath electrospinning method were found to have a larger diameter than the nanofibers produced by a simple electrospinning method as shown in **Figure 6.3**. CSN1 [**Figure 6.3 (a1 & a2)**], electrospun at a flow rate of 0.6 mL/h, had a diameter of 526 ± 60 nm, whereas CSN2 [**Figure 6.3 (b1 & b2)**], electrospun at flow rate of 1 mL/h, had fibre diameter of 630 ± 137 nm. Core-sheath morphology of CSN1 and CSN2 was confirmed by transmission electron micrographs in **Figure 6.3 (c1 & c2)**, respectively. The core (PCL) thickness of CSN1 and CSN2 was measured to be 255 ± 62 nm and 409 ± 91 nm, respectively, from TEM images using ImageJ software. These results are consistent with earlier reports that higher flow rate produces nanofibers of larger diameter [446-448].

6.2.2 X-ray diffraction analysis

The XRD patterns of the blended and core-sheath nanofibers show two sharp diffraction peak at 2θ = 21.5° and 23.7° corresponding to (110) and (200) planes of orthorhombic crystalline structures of PCL as shown in **Figure 6.4** and **Figure 6.5** [449]. According to previous reports, MEH-PPV also shows its characteristics peaks at 2θ = 21.5° and 28.2° corresponding to the diffractions from (110) and (210) plane of the monoclinic unit cell of the PPV crystal [450, 451]. The XRD patterns of CSN1 and CSN2 also display the peak at 2θ = 28.6°, however, the signal is small but broad, indicating amorphous nature short range arrangement of MEH-PPV chain. Moreover, two other peaks at 2θ = 13.1° and 15.6° with very small intensities appear in the XRD patterns of CSN1 and CSN2. Similar peaks were also observed by Abbassi *et al.* for pure MEH-PPV [452]. The low intensities of XRD peaks for MEH-PPV can be attributed to the lower concentration of MEH-PPV (0.5 wt%) as compared to that of PCL (14 wt%). The XRD results provide initial confirmation of the presence of both PCL and MEH-PPV in the as-synthesized electrospun meshes and their crystalline

structures. However, the crystallinity is predicted to arise from crystalline nature of PCL only [453].

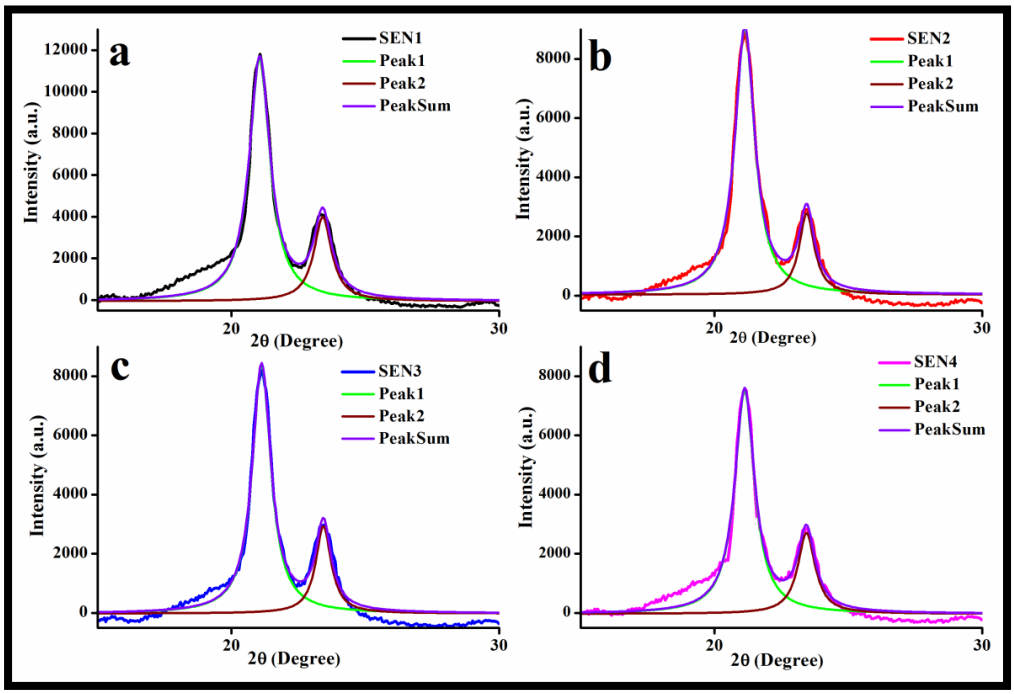

Figure 6.4. X-ray diffraction patterns of (a) SEN1, (b) SEN2, (c) SEN3 and (d) SEN4 as labeled along with a Voigtian fit of the x-ray profile that best describes the x-ray pattern of the blended electrospun nanofibers of MEH-PPV and PCL.

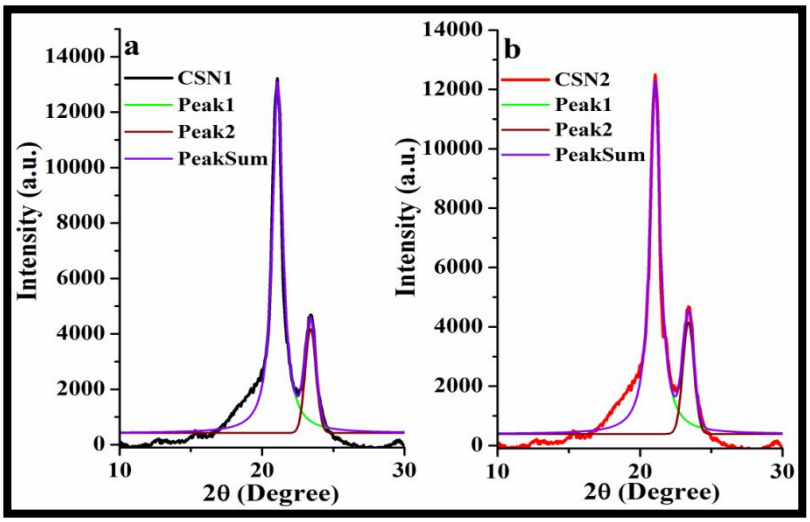

Figure 6.5. X-ray diffraction patterns of (a) CSN1 and (b) CSN2 as labeled along with a Voigtian fit of the x-ray profile that best describes the x-ray pattern of the core-sheath electrospun nanofibers.

Table 6.1. Characteristics of the X-ray diffraction peaks of blended MEH-PPV:PCL nanofibers and core-sheath MEH-PPV:PCL nanofibers corresponding to (110) and (200) reflections.

Sample	Peaks (hkl)	*d* (Å)	*L* (Å)	Strain (*e*) (%)
SEN1	(110)	4.17	53.87	0.11
SEN2		4.14	48.08	0.23
SEN3		4.13	46.46	0.24
SEN4		4.12	39.34	0.31
CSN1		4.11	34.23	0.53
CSN2		4.07	36.12	0.76
SEN1	(200)	3.85	43.84	0.18
SEN2		3.86	42.31	0.20
SEN3		3.78	43.33	0.28
SEN4		3.75	40.33	0.35
CSN1		3.77	37.45	0.43
CSN2		3.68	35.44	0.42

6.2.3 Thermogravimetric (TGA) analysis

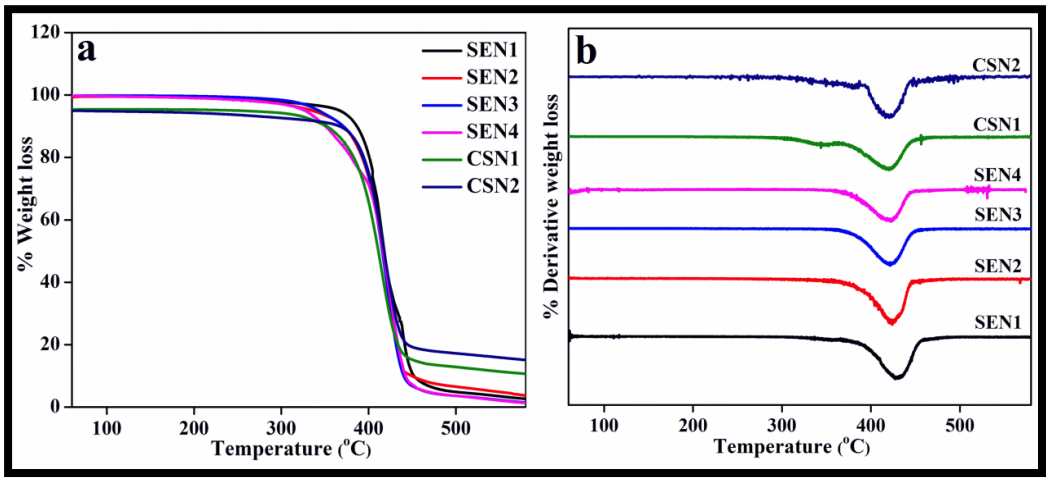

Figure 6.6. (a) TGA thermograms and (b) DTG plots of blended and core-sheath MEH-PPV:PCL nanofibers.

Table 6.2. Major thermal degradation temperatures and corresponding weight loss of the blended and core-sheath MEH-PPV:PCL nanofibers.

Sample name	Starting degradation temperature (^oC)	Major degradation temperature (^oC)	% Weight loss
SEN1	356	430	64
SEN2	343	424	68
SEN3	325	421	71
SEN4	318	419	74
CSN1	307	420	65
CSN2	299	419	61

Thermal stability of different electrospun nanofibers have been investigated with the help of thermogravimetric analyzer at a heating rate of 30°C/min under nitrogen atmosphere. The TGA thermograms and DTG plots of the blended MEH-PPV:PCL nanofibers and core-sheath MEH-PPV:PCL electrospun nanofibers are shown in **Figure 6.6 (a) & (b)**. It has been observed that all the electrospun nanofibers show one stage decomposition process in nitrogen environment up to 600°C. However, the starting and maximum decomposition temperatures are different for different electrospun nanofibers and the observations are depicted in **Table 6.2**. The pure MEH-PPV shows two stage decomposition process in nitrogen environment: the major weight loss occurs at 413°C in the first stage, while the second decomposition occurs at 783°C [454-456]. The major decomposition of PCL also occurs at 433°C in nitrogen environment at a heating rate of 30°C/min [457]. It has been observed that electrospun nanofibers prepared from the blend of MEH-PPV and PCL reveal the major degradation temperature in the range of 419-430°C. The blended electrospun nanofibers show the shifting of the major degradation temperature towards lower temperature with increasing concentration of MEH-PPV [**Table 6.2**]. The core-sheath nanofibers, i.e., CSN1 and CSN2 also depict major degradation at 420°C and 419°C, respectively. The results further indicates that the decomposition process starts at lower temperature for the blended electrospun nanofibers with higher concentration MEH-PPV in the blend as shown in **Table 6.2**. The decomposition of the core-sheath nanofibers starts even at lower temperature than that of the blended nanofibers with the highest MEH-PPV concentration. Moreover, the weight loss of the core-sheath nanofibers and the blended nanofibers with the higher MEH-PPV concentration are greater at the maximum degradation temperature [**Table 6.2**]. The results suggest that

the reduction in the thermal stability of the blended nanofibers with increasing MEH-PPV concentration is due to the lower thermal stability of MEH-PPV than that of PCL. The lower thermal stability of the core-sheath nanofibers is also assigned to MEH-PPV present on the sheath of the core-sheath nanofibers.

6.2.4 Current-voltage (I-V) characteristics

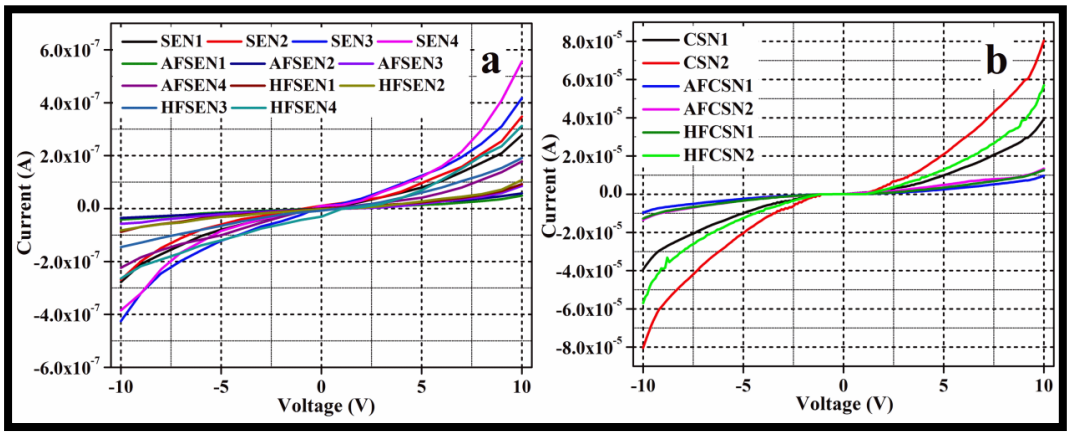

Figure 6.7. Room temperature (300 K) *I-V* characteristics of (a) blended MEH-PPV:PCL nanofibers and (b) core-sheath MEH-PPV:PCL nanofibers.

Figure 6.7 (a) & (b) show the room temperature (300 K) *I-V* characteristics of non-functionalized and surface functionalized electrospun nanofibers produced by a simple electrospinning and coaxial electrospinning process, respectively. The *I-V* characteristics of all the electrospun nanofibers show nonlinear behavior which is quite symmetric with respect to the both polarity in the applied voltage range of -10 V to +10 V. In case of the electrospun nanofibers prepared from the blend of MEH-PPV and PCL, the value of current is higher at a particular voltage for higher concentration of $FeCl_3$ doped MEH-PPV [**Figure 6.7 (a)**]. The core-sheath nanofibers show improved *I-V* characteristics with higher value of current when compared to the nanofibers prepared from the blend of MEH-PPV and PCL by simple electrospinning process [**Figure 6.7 (b)**]. The higher concentration of charge carriers with increasing concentration of $FeCl_3$ doped MEH-PPV results higher value of current as observed in the *I-V* characteristics of the nanofibers prepared by simple electrospinning process, whereas $FeCl_3$ doped MEH-PPV on the surface of the core-sheath nanofibers contributes towards the improved *I-V* characteristics.

Moreover, the *I-V* characteristics of all the electrospun nanofibers after surface functionalization by APTES and 1,6-Hexanediamine demonstrate slightly lower value of current at a particular applied voltage than that of their non-functionalized counterparts [**Figure 6.7 (a) & (b)**]. However, it has been observed that 1,6-Hexanediamine functionalized blended MEH-PPV:PCL nanofibers (HFSEN1, HFSEN2, HFSEN3, and HFSEN4) and core-sheath MEH-PPV:PCL nanofibers (HFCSN1 and HFCSN2) show better I-V characteristics than those of APTES functionalized blended MEH-PPV:PCL nanofibers (AFSEN1, AFSEN2, AFSEN3, and AFSEN4) and core-sheath MEH-PPV:PCL nanofibers (AFCSN1 and AFCSN2) [**Figure 6.7 (a) & (b)**].

However, the measurement of sheet resistance (R_s) demonstrates no significant change in conductive properties of the electrospun meshes after surface functionalization with APTES and 1,6-Hexanediamine. The sheet resistance (R_s) values of different electrospun nanofibers, which have been calculated using the formula given below [139, 155]:

$$Sheet\ resistance\ (R_s) = R \times \frac{W}{D} \qquad 6.1$$

Where W is the sample width and D is the distance between the two probes of the source meter. R is determined from the inverse of the slope of the *I-V* characteristics. The measured sheet resistance (R_s) values for all the electrospun nanofibers before and after surface functionalization have been presented in **Table 6.3**. The sheet resistance (R_s) of electrospun nanofibers produced by simple electrospinning method decreases with increase in MEH-PPV concentration [**Table 6.3**]**.** The decrease in sheet resistance with increase in MEH-PPV concentration, in turn, implies increase in surface conductivity of the electrospun nanofibers. With the highest concentration of conducting polymer (MEH-PPV) doped with $FeCl_3$, SEN4 has been found to possess the lowest sheet resistance (R_s) among the nanofibers prepared by simple electrospinning process. This proposition has been further supported by lower sheet resistance (R_s) of core-sheath nanofibers, where sheath material is only conductive MEH-PPV with non-conductive PCL in the core [**Table 6.3**]. Slight enhancement in sheet resistance (R_s) values of the functionalized electrospun meshes was observed without any change in the nature of I-V characteristics. This slight increase in surface resistivity values of the functionalized electrospun meshes is attributed to the loss of π–π conjugation in MEH-PPV

backbone during functionalization. The results demonstrate that functionalization was performed without much affecting the conductive properties of MEH-PPV.

The log-log plot of the positive side of the corresponding *I-V* data can provide a better insight into the conduction mechanisms in the different electrospun nanofibers [345]. The log-log plots show two distinct regions with a gradual transition between the two regions: one in one in the lower voltage region (0<V<3 for SEN1, SEN2, AFSEN1, AFSEN2, HFSEN1 and HFSEN2; 0<V<2 for SEN3, SEN4, AFSEN3, AFSEN4, AFCSN1, AFCSN2, HFSEN3, HFSEN4, HFCSN1, and HFCSN2) and other is in the higher voltage region (3<V<10 for SEN1, SEN2, AFSEN1, AFSEN2, HFSEN1 and HFSEN2 and 2<V<10 SEN3, SEN4, AFSEN3, AFSEN4, AFCSN1, AFCSN2, HFSEN3, HFSEN4, HFCSN1, and HFCSN2) [**Figure 6.8 & Figure 6.9**]. These two distinct linear regions on the log-log plot can be fitted to a power law equation with different exponents, expressed as:

$$I = KV^m \qquad 6.2$$

where K is a constant and m is the exponent, which can be obtained from the slope of the fitted curve. At lower voltage region, the exponent (m_1) is nearly unity and at higher voltage region, the exponent (m_2) is different from unity as shown in **Figure 6.8 (a1-d3) & Figure 6.9 (a1-b3)**. It indicates that at lower voltage region, the current varies linearly with voltage suggesting the charge transport mechanism is Ohmic, whereas current varies non-linearly at higher voltage region suggesting space charge limited conduction (SCLC). The observed *I-V* characteristics, with two power law regions are consistent with the space-charge limited conduction (SCLC) due to the presence of trapped charges in MEH-PPV [458]. At low voltages, the number of injected electrons is very small as compared to the intrinsic carriers making the charge transport mechanism Ohmic. As the bias voltage is increased above 2-3 V, a transition from Ohmic to non-Ohmic behaviour takes place, when the density of the injected carriers becomes comparable to the density of the thermally generated free carriers and SCLC occurs. The bias voltage at which the transition from Ohmic to non-Ohmic behaviour occurs is called the critical voltage (V_c) and can be expressed as follows [346]:

$$V_c = \frac{8}{9}\frac{qp_o d^2}{\varepsilon_o \varepsilon_r \theta} \qquad 6.3$$

where p_o is the density of thermally generated charge carriers, d is the sample thickness, ε_o the permittivity in free space and ε_r is the dielectric constant of the

sample. The trap factor given by, $\theta = p/(p+p_t)$, where p is the density of free charge carriers and p_t is the density of trapped charge carriers, increases due to increase in the free charge carrier density (p) in the sample.

Table 6.3. Calculated sheet resistance (R_s) values of the different electrospun meshes prepared by simple electrospinning and coaxial electrospinning process. Sheet resistance (R_s) data were expressed as Mean ± S.D (n=3).

Sample name	Sheet resistance (R_s) (Ω)	Critical voltage (V_c) V
SEN1	$5.27 \pm 1.73 \times 10^7$	2.81
SEN2	$3.17 \pm 1.03 \times 10^7$	2.39
SEN3	$1.52 \pm 0.93 \times 10^7$	1.90
SEN4	$2.45 \pm 2.02 \times 10^6$	1.33
CSN1	$2.04 \pm 1.15 \times 10^5$	1.05
CSN2	$1.35 \pm 0.65 \times 10^5$	1.13
AFSEN1	$9.44 \pm 2.05 \times 10^7$	3.07
AFSEN2	$8.51 \pm 1.89 \times 10^7$	2.71
AFSEN3	$5.13 \pm 1.24 \times 10^7$	2.02
AFSEN4	$5.32 \pm 1.11 \times 10^6$	1.91
AFCSN1	$3.33 \pm 1.47 \times 10^5$	1.24
AFCSN2	$2.69 \pm 1.34 \times 10^5$	1.40
HFSEN1	$8.56 \pm 1.85 \times 10^7$	3.02
HFSEN2	$7.76 \pm 2.19 \times 10^7$	2.61
HFSEN3	$4.44 \pm 0.87 \times 10^7$	2.00
HFSEN4	$3.67 \pm 1.54 \times 10^6$	1.45
HFCSN1	$2.16 \pm 1.24 \times 10^7$	1.19
HFCSN2	$1.82 \pm 1.11 \times 10^6$	1.27

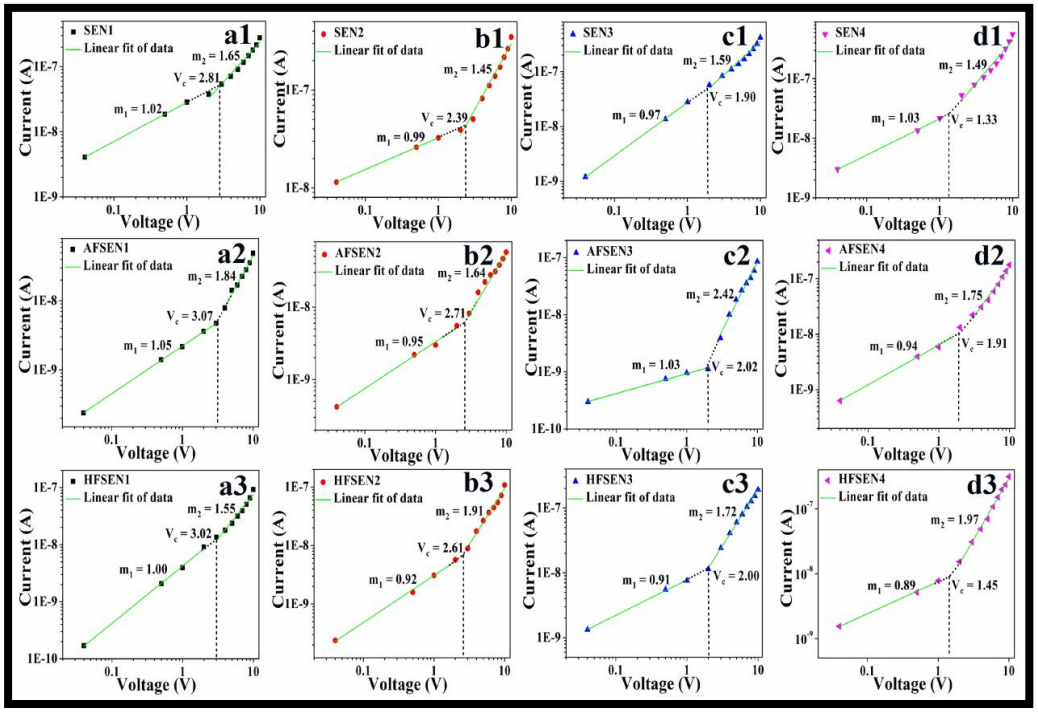

Figure 6.8. Plots of forward *I-V* data on a log-log scale for (a1) SEN1, (b1) SEN2, (c1) SEN3, (d1) SEN4, (a2) AFSEN1, (b2) AFSEN2, (c2) AFSEN3, (d2) AFSEN4, (a3) HFSEN1, (b3) HFSEN2, (c3) HFSEN3, and (d3) HFSEN4 at room temperature (300 K) showing the fitting parameters.

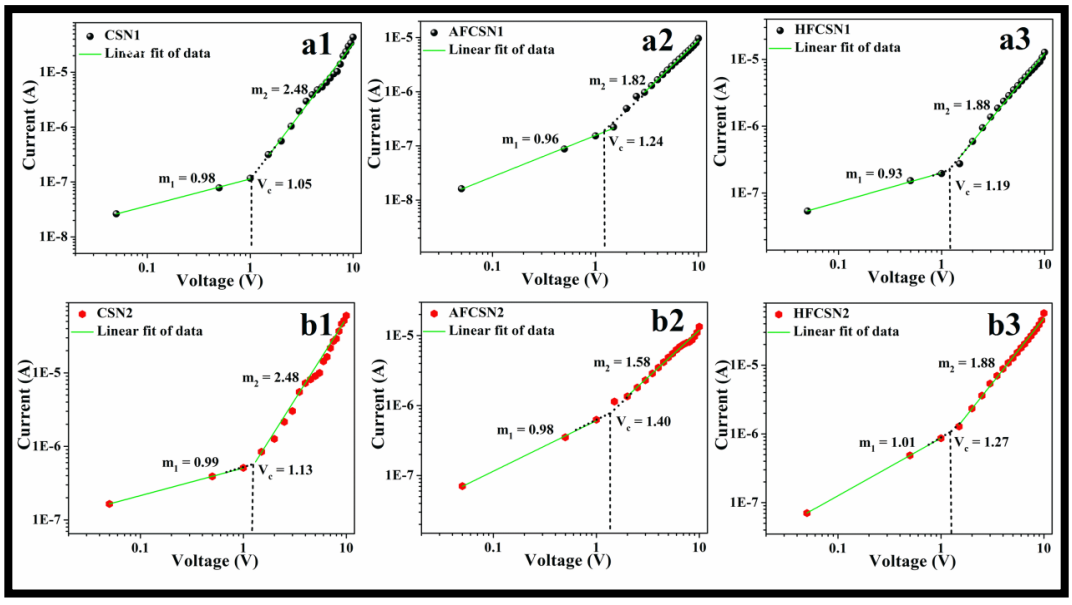

Figure 6.9. Plots of forward *I-V* data on a log-log scale for (a1) CSN1, (a2) AFCSN1, (a3) HFCSN1, (b1) CSN2, (b2) AFCSN2, and (b3) HFCSN2 at room temperature (300 K) showing the fitting parameters.

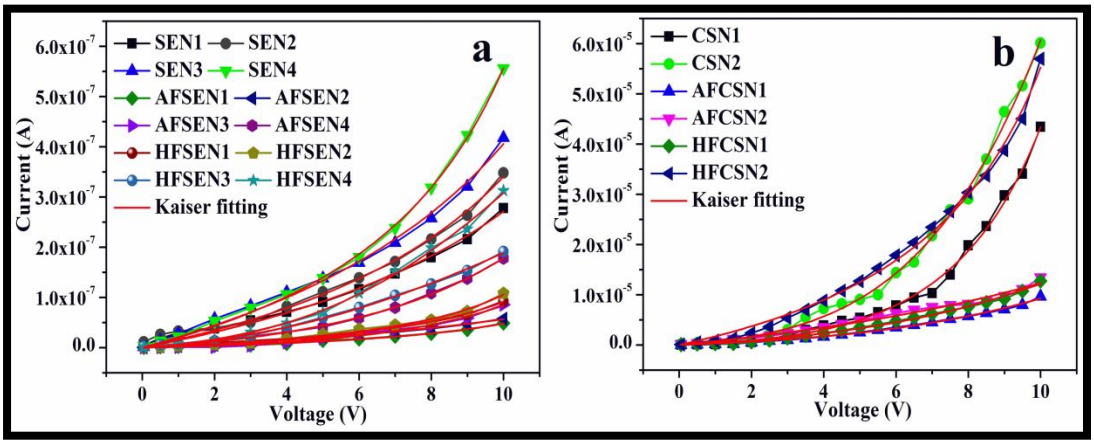

Figure 6.10. Positive sides of *I-V* characteristics of (a) non-functionalized and functionalized blended MEH-PPV:PCL nanofibers and (b) non-functionalized and functionalized core-sheath MEH-PPV:PCL nanofibers fitted with *Kaiser Equation*.

The critical voltages (V_c) determined from the log-log plot from the intersection of the two linear lines extended from the linear fit as shown in **Figure 6.8 & Figure 6.9** shift towards lower voltage side with increasing MEH-PPV concentration for the nanofibers prepared from simple electrospinning process. The core-sheath nanofibers have also lower critical voltages (V_c) [**Table 6.3**]. The lower values of V_c for the core-sheath nanofibers (CSN1<CSN2<HFCSN1<AFCSN1<HFCSN2<AFCSN1) and nanofibers with higher MEH-PPV concentration (SEN4<HFSEN4<SEN3<AFSEN4< HFSEN3 <AFSEN3<SEN2<HFSEN2<AFSEN2<SEN1<HFSEN1<AFSEN1) are assigned to the higher density of free charge carriers *(p)* due to $FeCl_3$ doped MEH-PPV, which results their improved conductive properties as compared to the blended MEH-PPV:PCL nanofibers, particularly SEN1, SEN2, SEN3 and their functionalized counterparts [**Table 6.3**]. In addition, the results demonstrate that 1,6-Hexanediamine functionalized nanofibers have lower values of V_c than those of their APTES functionalized counterparts [**Table 6.3**].

MEH-PPV has been reported to possess high density of holes and traps, for which it shows non-linear *I-V* characteristics. Kaiser *et al*. showed that such kind of non-linearity in *I-V* characteristics depends on applied electric field according to *Equation 6.4*:

$$G = \frac{I}{V} = \frac{G_0 \exp(V/V_0)}{1 + h[\exp(V/V_0) - 1]} \qquad 6.4$$

where G_0 is temperature dependence low field ($V \rightarrow 0$) conductance, $h = {}^{G_0}/_{G_h}$ (h < 1) results the decrease of *G* below the exponential increase at higher voltages *V* (G_h is the saturated conductance at high field). V_0 is the voltage scale factor that gives an exponential increase in conductance as *V* increases.

Table 6.4. Fitting parameters to *Kaiser equation* for blended MEH-PPV:PCL nanofibers and core-sheath MEH-PPV:PCL nanofibers before and after surface functionalization by APTES and 1,6-Hexanediamine.

Sample	G_o (S)	V_o (V)	h
SEN1	5.82×10^{-10}	2.93	0.017
SEN2	7.78×10^{-10}	2.56	0.034
SEN3	5.46×10^{-9}	2.07	0.031
SEN4	8.18×10^{-8}	1.42	0.093
CSN1	6.52×10^{-7}	1.25	0.152
CSN2	7.43×10^{-7}	1.16	0.235
AFSEN1	2.36×10^{-10}	3.31	0.010
AFSEN2	4.21×10^{-10}	2.87	0.018
AFSEN3	3.33×10^{-9}	2.28	0.022
AFSEN4	4.78×10^{-8}	1.87	0.067
AFCSN1	4.28×10^{-7}	1.42	0.124
AFCSN2	5.61×10^{-7}	1.45	0.181
HFSEN1	6.02×10^{-10}	3.11	0.015
HFSEN2	5.44×10^{-10}	2.68	0.025
HFSEN3	4.73×10^{-9}	2.12	0.029
HFSEN4	6.38×10^{-8}	1.51	0.079
HFCSN1	5.98×10^{-7}	1.34	0.147
HFCSN2	6.67×10^{-7}	1.31	0.206

The positive sides of the *I-V* data of all the materials were fitted according to *Kaiser equation* and are shown in **Figure 6.10 (a) & (b)**. The fitting parameters obtained from the Kaiser fitting are presented in **Table 6.4**. It shows that the low field

conductance (G_0) and the parameter h for the core-sheath nanofibers (both non-functionalized and functionalized) are greater than those of the blended nanofibers (both non-functionalized and functionalized). However, SEN4 with the highest MEH-PPV concentration [60% (v/v)] and their surface functionalized counterparts (AFSEN4 and HFSEN4) demonstrate the higher values of G_0 and h amongst all the blended electrospun nanofibers [**Table 6.4**]. The higher values of G_0 of the core-sheath nanofibers (both non-functionalized and functionalized) and SEN4 (both non-functionalized and functionalized) indicate the easier hopping of charge carriers throughout the polymer chains, while the higher values of h correspond to the increase in conductance at low field [**Table 6.4**]. It has been also observed that voltage scale factor (V_0) for the core-sheath nanofibers (both non-functionalized and functionalized) and SEN4 (both non-functionalized and functionalized) varies in a small range from 1.16 to 1.51 indicating almost similar non-linearities of their corresponding *I-V* characteristics [**Table 6.4**]. However, SEN1, SEN2, SEN3 and their surface functionalized counterparts demonstrate significant variation in non-linearities of their *I-V* characteristics (V_0 varies in the range 2.07-3.31) from those of the core-sheath nanofibers (both non-functionalized and functionalized) and SEN4 (both non-functionalized and functionalized).

6.2.5 Mechanical strength test

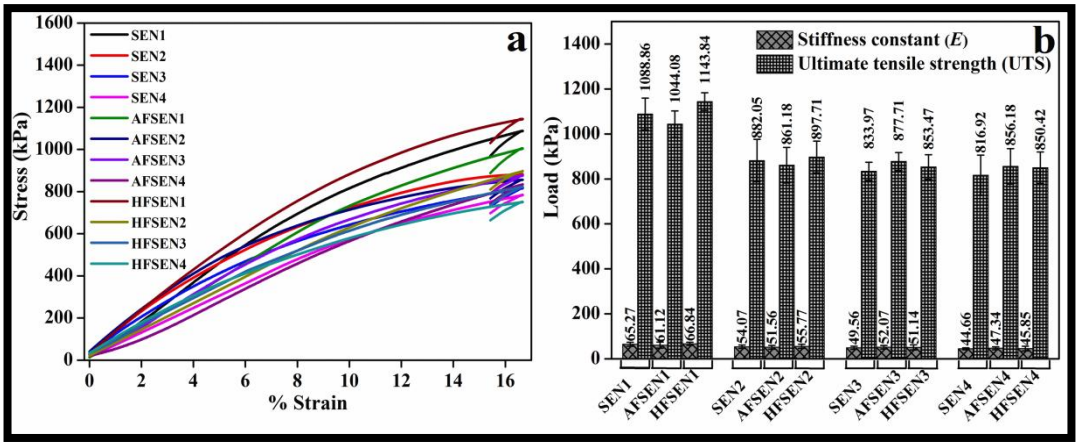

Figure 6.11. (a) Stress *vs* Strain curve and (b) comparison of Young Modulus or stiffness constant (*E*) and ultimate tensile strength (UTS) of blended MEH-PPV:PCL nanofibers prepared by simple electrospinning process before and after surface functionalization. Data were expressed as Mean ± S.D (n=3).

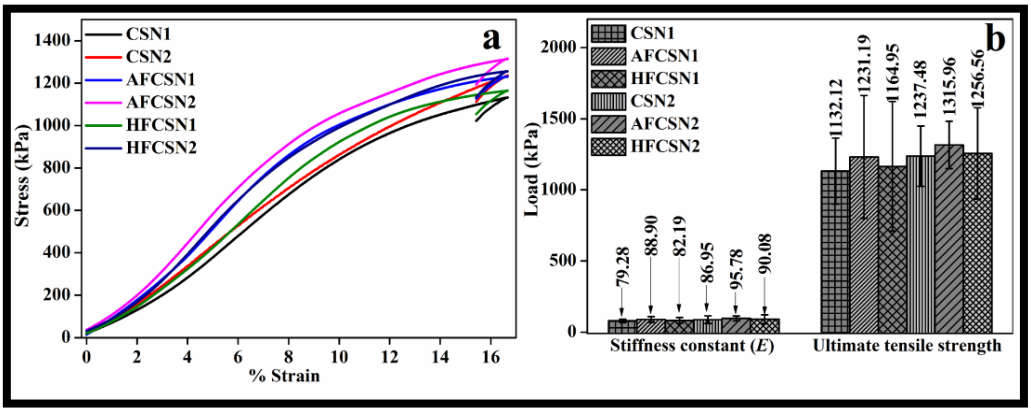

Figure 6.12. (a) Stress *vs* Strain curve and (b) comparison of Young Modulus or stiffness constant (*E*) and ultimate tensile strength (UTS) of the core-sheath MEH-PPV:PCL nanofibers prepared by coaxial electrospinning process before and after surface functionalization. Data were expressed as Mean ± S.D (n=3).

The biomaterial scaffolds desired for specific tissue engineering applications should possess superior mechanical properties to confirm the integrity and stability of implanted graft at the site of injury [121]. Moreover, the scaffolds for normal cell function should be strong. Therefore, the tensile strength test was performed to investigate the mechanical properties in terms of the stiffness constant (*E*) and ultimate tensile strength (UTS) of the non-functionalized and functionalized blended and core-sheath nanofibers. The stress *vs.* strain curves for the non-functionalized and functionalized blended electrospun nanofibers are shown in **Figure 6.11 (a)**, whereas for the non-functionalized and functionalized core-sheath electrospun nanofibers, they are shown in **Figure 6.12 (a)**. Mechanical properties, especially the Young's modulus or stiffness constant (*E*) and UTS of the scaffolds were derived from these curves and are presented in **Figure 6.11 (b)** (non-functionalized and functionalized blended electrospun nanofibers) and **Figure 6.12 (b)** (non-functionalized and functionalized core-sheath electrospun nanofibers). In case of the blended electrospun nanofibers, the nanofibrous meshes with larger fiber diameter demonstrate greater stiffness constant (*E*) and UTS in the order SEN1>SEN2>SEN3>SEN4 [**Figure 6.11 (b)**]. This proposition is also applied to the core-sheath nanofibers, as CSN2 with larger fiber diameter exhibits greater stiffness constant (*E*) and UTS than those of CSN1 with smaller diameter [**Figure 6.12 (b)**]. The core-sheath nanofibers possess larger fiber diameter as compared to the blended nanofibers and consequently, they exhibit

superior mechanical properties in terms of the stiffness constant (*E*) and UTS. These results are consistent with previous reports that thicker nanofibers have moderately higher stiffness constant [459]. The exact mechanical properties of MEH-PPV in non-woven nanofibrous mats have not been investigated prior to this study. However, the increase in the stiffness constant (*E*) with increase in fibre diameter can be correlated with the strong junctions in thicker fibres [460]. The lower value of the stiffness constant (*E*) of SEN2, SEN3 and SEN4 as compared to SEN1 and core-sheath nanofiber mat (CSN1 and CSN2) is also believed to be due to the presence of beaded fibres in the formers. The core-sheath nanofiber meshes of CSN1 and CSN2 have a higher stiffness constant (*E*) and UTS due to larger fiber diameter and core-sheath morphology.

Interestingly, in case of the core-sheath nanofibrous mats, both APTES and 1,6-Hexanediamine functionalized meshes demonstrate enhanced stiffness constant (*E*) and UTS as compared to their non-functionalized counterparts [**Figure 6.12 (b)**]. It can be assigned due to the cross-linking between the polymer chains occurred after functionalization. To speak more specifically, the APTES functionalized core-sheath meshes exhibit improved mechanical properties than the 1,6-Hexanediamine functionalized meshes. It is believed APTES plays a crucial role in cross-linking between the polymer chains or among the surrounding fibers in the mesh than 1,6-Hexanediamine. Because, it has been observed that the in the case of blended nanofibers, APTES functionalized meshes with higher MEH-PPV concentration, particularly, AFSEN3 and AFSEN4, demonstrate greater stiffness constant (*E*) and UTS than those of non-functionalized meshes (SEN3 and SEN4) and 1,6-Hexanediamine functionalized meshes (HFSEN3 and HFSEN4). However, 1,6-Hexanedimaine functionalized meshes of SEN1 and SEN2 with relatively lower MEH-PPV concentration but greater PCL concentration, i.e., HFSEN1 and HFSEN2 show greater stiffness constant (*E*) and UTS than those of SEN1, SEN2, AFSEN1 and AFSEN2 [**Figure 6.11 (a)**]. The results suggest that APTES has better ability to cross-link between the polymer chains or the surrounding nanofibers with more MEH-PPV on the surface as in the case of core-sheath nanofibers or SEN3 and SEN4, whereas 1,6-Hexanediamine causes cross-linking between the polymer chains or surrounding fibers having higher PCL concentration. Thus, the results further indicates that APTES and 1,6-Hexanediamine dominate selectively to enhance the mechanical properties of different electrospun nanofibrous meshes depending on the

type of its constituents. However, like the non-functionalized meshes, functionalized meshes also follow the proposition that nanofibrous meshes with larger fiber diameter exhibit better mechanical properties.

6.2.6 Stability test

To investigate the degradation and stability, all the electrospun meshes were incubated in a physiological solution of phosphate buffered saline (PBS, pH=7.4) at 37°C for 45 days as reported elsewhere [155]. Degradation and stability of the electrospun meshes were evaluated by SEM and measurements of current-voltage (*I-V*) characteristics after 45 days of incubation. Percentage of weight loss after 45 days has been measured using the following formula:

$$\%\, Weight\ loss = \frac{Change\ in\ weight\ after\ 45\ days\ (in\ mg)}{Original\ weight\ before\ 45\ days\ (in\ mg)} \times 100\% \qquad 6.5$$

The electrospun nanofibers have been characterized using SEM and percentage of weight loss was determined after 45 days to confirm any degradation occurred if any. For SEM images, the samples were washed with deionized water twice to remove salts and air dried. Measurements for *I-V* characteristics were performed three times for each sample and sheet resistance (R_s) values were determined as described above to check the stability of the conductive properties of the electrospun nanofibers in physiological condition. The SEM images of different blended MEH-PPV:PCL electrospun meshes and core-sheath MEH-PPV:PCL electrospun meshes after 45 days of incubation in PBS (pH=7.4) are shown in **Figure 6.13** and **Figure 6.14**, respectively. The measured fiber diameters, sheet resistance (R_s) values and percentage of weight loss after 45 days of incubation in PBS (pH=7.4) are presented in **Table 6.5**.

SEM micrographs of different blended and core-sheath nanofibers reveal no significant degradation observed to the nanofibers [**Figure 6.13 & Figure 6.14**]. The diameters of the nanofibers kept in PBS for 45 days have appeared to be slightly decreased from their counterparts that were not incubated in PBS [**Table 6.5**]. It has been observed that SEN1 and their functionalized counterparts (AFSEN1 and HFSEN1) with the highest concentration of biodegradable polymer, PCL demonstrate highest percent of weight loss amongst all the electrospun meshes [**Table 6.5**]. It has been further demonstrated that APTES and 1,6-Hexanediamine functionalized electrospun meshes show higher percent of weight loss than that of their non-

functionalized counterparts as shown in **Table 6.5**. However, APTES functionalized electrospun meshes reveal higher weight loss as compared to weight loss occurred to the 1,6-Hexanediamine functionalized electrospun meshes. This can be attributed to the hydrolysis behavior of APTES in PBS [440, 461]. The results suggest that surface functionalization causes enhancement in degradability of the electrospun nanofibers even though the degradation in terms of weight loss is much smaller in physiological condition after 45 days of incubation. Most importantly, the sheet resistance (R_s) values have not been observed to be decreased significantly from their counterparts without treatment with PBS [**Table 6.5**]. The results reveal that the electrospun nanofibers are stable enough in physiological solution due to nondegradable nature of MEH-PPV and slow degradation rate of PCL, which indicates the potential of these nanofibers as a conductive scaffold for tissue engineering applications, particularly for neural tissue engineering [432, 433].

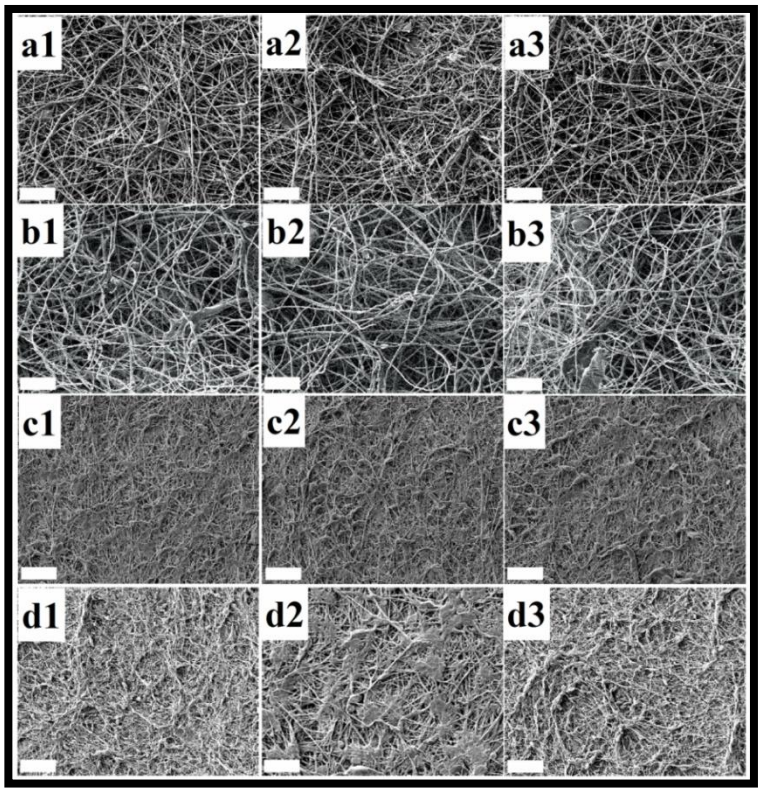

Figure 6.13. Scanning electron micrographs of (a1) SEN1, (a2) AFSEN1, (a3) HFSEN1, (b1) SEN2, (b2) AFSEN2, (b3) HFSEN2, (c1) SEN3, (c2) AFSEN3, (c3) HFSEN3, (d1) SEN4, (d2) AFSEN4 and (d3) HFSEN4 recorded after keeping in PBS (pH=7.4) for 45 days (Scale bar = 10 μm).

Table 6.5. Fiber diameters, sheet Resistance (R_s), and percentage of weight loss of the different blended MEH-PPV:PCL electrospun nanofibers and core-sheath MEH-PPV:PCL nanofibers before and after 45 days of incubation in PBS (pH=7.4).

Sample name	Diameter nm		Sheet Resistance (R_s) Ω		% Weight loss
	Before	After	Before	After	
SEN1	324±70	307±88	$5.27 \pm 1.73\times10^{7}$	$7.03 \pm 2.11\times10^{7}$	10.32
SEN2	280±82	275±56	$3.17 \pm 1.03\times10^{7}$	$4.31 \pm 1.25\times10^{7}$	6.45
SEN3	198±30	192±61	$1.52 \pm 0.93\times10^{7}$	$1.60 \pm 0.88\times10^{7}$	4.27
SEN4	132±53	130±44	$2.45 \pm 2.02\times10^{6}$	$2.15 \pm 1.13\times10^{6}$	3.54
CSN1	546±60	540±192	$2.04 \pm 1.15\times10^{5}$	$2.44 \pm 1.56\times10^{5}$	2.45
CSN2	630±137	617±140	$1.35 \pm 0.65\times10^{5}$	$2.01 \pm 1.15\times10^{5}$	2.79
AFSEN1	327±66	305 ±69	$9.44 \pm 2.05\times10^{7}$	$2.32 \pm 1.43\times10^{8}$	13.45
AFSEN2	282±47	271±74	$8.51 \pm 1.89\times10^{7}$	$9.72 \pm 3.03\times10^{7}$	8.71
AFSEN3	202±64	184±59	$5.13 \pm 1.24\times10^{7}$	$7.64 \pm 2.08\times10^{7}$	8.12
AFSEN4	139±55	113±39	$5.32 \pm 1.11\times10^{6}$	$6.46 \pm 2.17\times10^{6}$	9.56
AFCSN1	541±95	509±118	$3.33 \pm 1.47\times10^{5}$	$5.13 \pm 1.52\times10^{5}$	9.09
AFCSN2	660±151	648 ±162	$2.69 \pm 1.34\times10^{5}$	$4.14 \pm 1.84\times10^{5}$	7.89
HFSEN1	333±75	302±69	$8.56 \pm 1.85\times10^{7}$	$3.45 \pm 2.02\times10^{7}$	11.12
HFSEN2	288±89	268±91	$7.76 \pm 2.19\times10^{7}$	$9.82 \pm 1.67\times10^{7}$	5.55
HFSEN3	205±58	182 ±73	$4.44 \pm 0.87\times10^{7}$	$5.51 \pm 1.73\times10^{7}$	5.68
HFSEN4	135±63	131±52	$3.67 \pm 1.54\times10^{6}$	$4.32 \pm 2.11\times10^{6}$	4.65
HFCSN1	528±110	517±132	$2.16 \pm 1.24\times10^{7}$	$2.42 \pm 0.98\times10^{7}$	5.12
HFCSN2	643±144	637±140	$1.82 \pm 1.11\times10^{6}$	$2.18 \pm 0.78\times10^{6}$	3.52

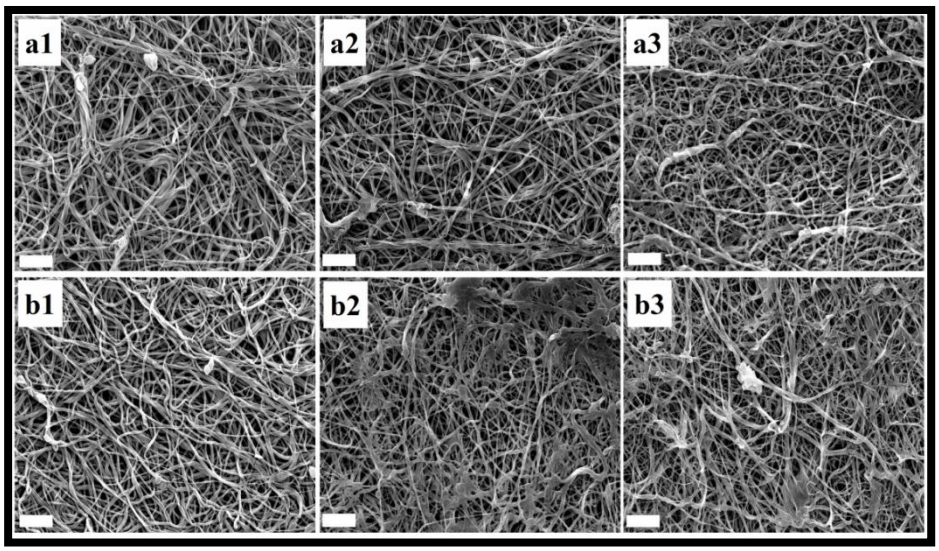

Figure 6.14. Scanning electron micrographs of CSN1 (a1), AFCSN1 (a2), HFCSN1 (a3), CSN2 (b1), AFCSN2 (b2) and HFCSN2 (b3), recorded after keeping in PBS (p^H=7.4) for 45 days (Scale bar = 10 μm).

6.2.7 Surface chemistry

6.2.7.1 FT-IR spectroscopy

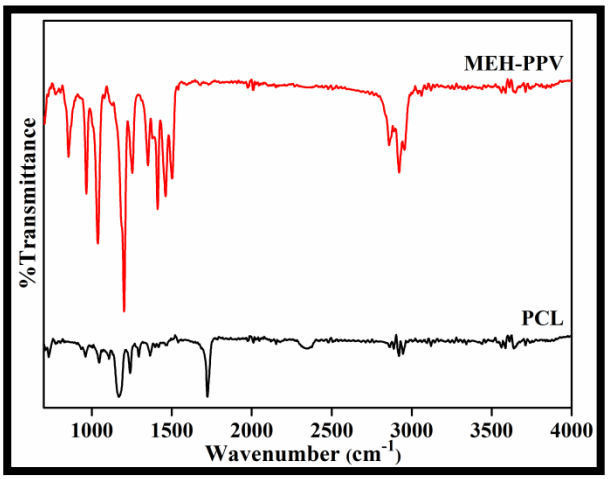

Figure 6.15. FT-IR spectra of pure PCL (black) and pure MEH-PPV (red).

Figure 6.15 shows the FT-IR spectra of pure PCL (black) and MEH-PPV (red). The FT-IR spectrum of pure PCL shows its characteristics vibrational bands around 1723 cm^{-1} and 3500 cm^{-1}, corresponding to C=O stretching of ester and O-H stretching in hydroxyl groups, respectively [462-464]. The symmetric and asymmetric C-O-C

stretching vibrations for PCL have been observed at 1172 cm^{-1} and 1240 cm^{-1}, respectively [462-464]. The weak vibrational band appeared at 1297 cm^{-1} corresponding to C–O and C–C stretching in the crystalline phase of PCL [462]. The symmetric and asymmetric CH_2 stretching vibrations in PCL appear in the range 2860-2894 cm^{-1} and 2916-2951 cm^{-1} respectively [462-264].

The FT-IR spectrum of MEH-PPV shown in **Figure 6.15** exhibits its characteristics peaks at 1677 cm^{-1} and 1501-1598 cm^{-1}, corresponding to C=C and C-C stretching in phenyl ring, respectively [465-467]. The aryl-alkyl ether (C-O-C) symmetric and asymmetric stretching vibrations in MEH-PPV appear at 1251 cm^{-1} and 1035 cm^{-1} respectively [466]. The bending (rocking) motion of CH_2 groups in the long aliphatic chain of MEH-PPV (attached with the ring via oxygen) appears at 768 cm^{-1} [465-467]. The small vibrational bands around 2860 cm^{-1} and 2922-2956 cm^{-1} in the FT-IR spectrum of MEH-PPV correspond to symmetric and asymmetric C-H stretch in -CH_2 group [465].

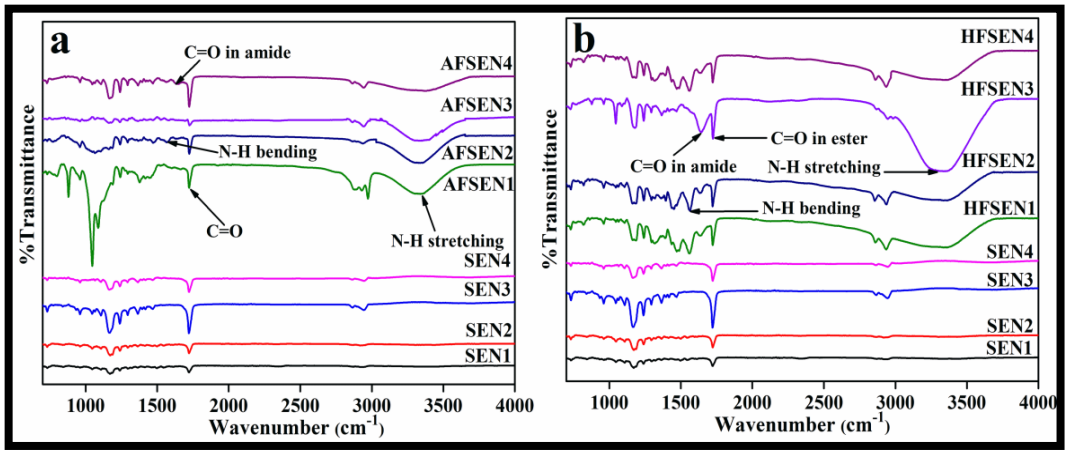

Figure 6.16. FT-IR spectra of blended MEH-PPV:PCL electrospun nanofibers before and after surface functionalization using (a) APTES and (b) 1,6-Hexanediamine.

Electrospun nanofibers produced by both a simple electrospinning process and coaxial electrospinning process showed characteristic vibrational bands for both MEH-PPV and PCL such as C=C stretch (1677 cm^{-1}), C-C ring stretch (1501-1598 cm^{-1}), aryl-alkyl ether (C-O-C) asymmetric stretch (1251 cm^{-1}) in MEH-PPV and similarly, C=O stretching of ester groups (1723 cm^{-1}), C-O and C-C stretching (1297 cm^{-1}), O–H stretching (3500-3600 cm^{-1}) in PCL as shown in **Figure 6.16 & Figure 6.17** . The weak bending vibration in the range 729-735 cm^{-1} is attributed to rocking motion of

CH_2 groups present in aliphatic chain of MEH-PPV and PCL. In particular, prominent but weak triplet in the 1500-1700 cm^{-1} region corresponding to C=C stretch of paraphenylene vinylene (PPV) ring in FTIR spectra of CSN1 and CSN2, indirectly indicates more exposure of MEH-PPV to IR [468]. The highest energy of these modes is not IR active on a symmetric ring and only very weakly active in MEH-PPV [469]. This observation indirectly indicates the presence of MEH-PPV in the sheath of the core-sheath nanofibers.

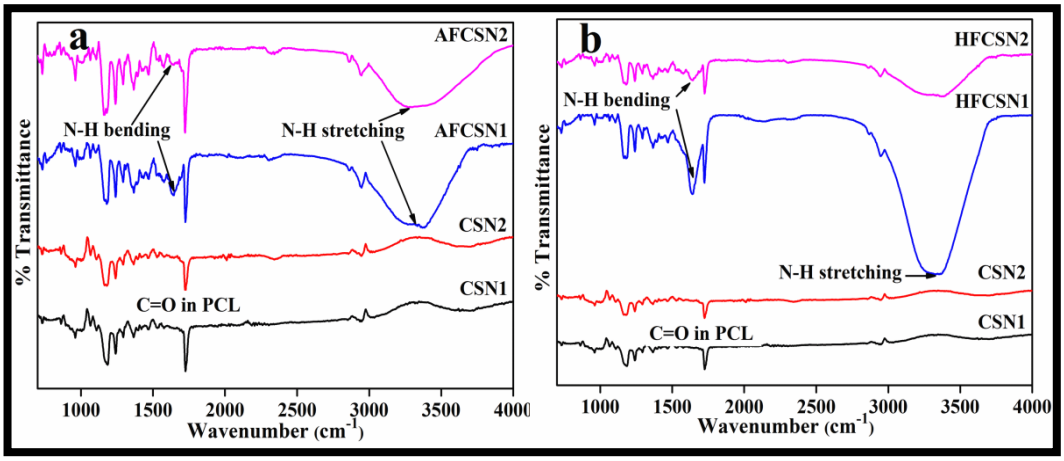

Figure 6.17. FT-IR spectra of core-sheath MEH-PPV:PCL nanofibers before and after surface functionalization using (a) APTES and (b) 1,6-Hexanediamine.

The FT-IR spectra of the APTES functionalized blended MEH-PPV:PCL nanofibers, shown in **Figure 6.16 (a)**, exhibit several new vibrational bands including the characteristics bands of PCL and MEH-PPV as appeared in the FT-IR spectra of the non-functionalized blended nanofibers. Particularly, the bands around 1560 cm^{-1} and 3500 cm^{-1} corresponding to C-N-H stretching/N-H bending and N-H stretching vibrations clearly indicates incorporation of amine functionality onto the blended nanofibers after surface functionalization by APTES. Besides, the characteristics band for Si-O appears in the range 1000-1100 with significantly higher intensities, which also overlaps with the characteristics bands of PCL and MEH-PPV [470]. A weak signal for C=O stretching in amide also appears in the FT-IR spectra of APTES functionalized nanofibers. The APTES functionalized core-sheath MEH-PPV:PCL nanofibers also reveals new vibrational bands in their FT-IR spectra around 1550-1567 cm^{-1} (N-H bending in secondary amine) and around 3350-3400 cm^{-1} (N-H

stretching in primary amine), indicating incorporation of amine functionality on the surface of the electrospun meshes [**Figure 6.17 (a)**].

The FT-IR spectra of 1,6-Hexanediamine functionalized blended and core-sheath nanofibers demonstrate the characteristics bands corresponding to N-H bending in secondary amine and N-H stretching in primary amine around 1550 cm^{-1} and 3400 cm^{-1}, respectively, which are not present in their non-functionalized counterparts [**Figure 6.16 (b) & Figure 6.17 (b)**]. More importantly, the C=O stretching in amide is distinct in the FT-IR spectra of the all the 1,6-Hexandeimaine functionalized nanofibers, indicating the incorporation of 1,6-Hexandeimaine onto the surface of the nanofibers through amide bond formation.

6.2.7.2 X-ray photoelectron spectroscopy

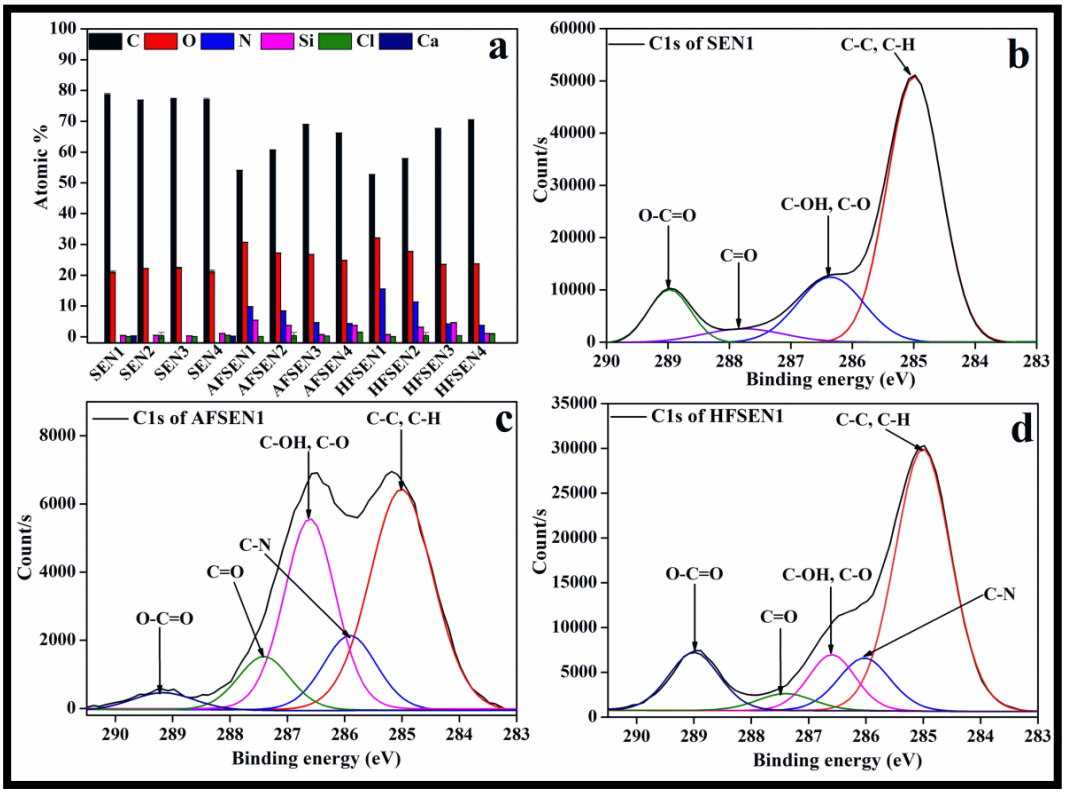

Figure 6.18. (a) Elemental composition in different blended MEH-PPV:PCL electrospun nanofibers before and after functionalization. Peak deconvolutions of high-resolution C1s XPS spectra of (b) SEN1 (c) AFSEN1 and (d) HFSEN1.

XPS analysis was carried out in order to understand the surface chemistry of the electrospun nanofibers and to further confirm the incorporation of amine functionality on the surface of the blended and core-sheath nanofibers after functionalization by

APTES and 1,6-Hexanediamine as indicated by the FT-IR results. Analysis of surface elemental composition of the non-functionalized and functionalized blended MEH-PPV:PCL nanofibers by XPS survey scans are shown in **Figure 6.18 (a)** and **Table 6.6**. Analysis of surface elemental composition by XPS survey scans showed that carbon (C1s) and oxygen (O1s) are the major compositions of all the blended electrospun nanofibers, with trace amounts of silicon (Si2p) and calcium (Ca2p) as external contaminants [**Figure 6.18 (a) & Table 6.6**]. The presence of atomic chlorine (Cl2p) marked in all the electrospun nanofibers demonstrate the doping level in MEH-PPV by $FeCl_3$. It has been observed that SEN4 and its functionalized counterparts, i.e., AFSEN4 and HFSEN4 possess highest atomic percent of Cl2p viz., 1.9%, 1.5% and 1%, respectively, among all the blended electrospun nanofibers due to highest MEH-PPV concentration in the blend [**Table 6.6**]. This observation is in well agreement of the improved conductive properties of SEN4 as discussed in **Section 6.2.4**. Furtthermore, all the APTES and 1,6-Hexanediamine functionalized blended nanofibers demonstrate the presence of nitogen (N1s) in their XPS survey scans as displayed in **Table 6.6**, confirming the incorporation amine functionality on the surface of the blended nanofibers after functionalization. Among them, AFSEN1, AFSEN2, HFSEN1 and HFSEN2 possess highest percent of atomic nitogen, viz. 9.8%, 8.4%, 15.5% and 11.3%, respectively [**Table 6.6**]. The C1s XPS spectra of SEN1, AFSEN1, and HFSEN1 along with their peak deconvolutions of are shown in **Figure 6.18 (b), (c) & (d)**, respectively. The details of peak deconvolutions of C1s spectra of these blended nanofibers are presented in **Table 6.7**. The C1s core-level spectrum of SEN1 can be deconvoluted into four peak components with binding energies (BEs) at about 284.99, 286.35, 287.79, and 288.96 eV, corresponding to C-C/C-H, C-OH/C-O, C=O and O=C-O species, respectively [**Figure 6.18 (b) & Table 6.7**] [366, 399, 400, 471-473]. Similarly, the C1s core-level spectra of AFSEN1 and HFSEN1 can be also deconvoluted into these four peak components with an additional peak at about 285.86 eV (AFSEN1) and 286.02 eV (HFSEN1) ascribed to C-N species [**Figure 6.18 (c) & (d)**] [366, 399, 400, 471-473].

Table 6.6. Elemental composition of non-functionalized and functionalized blended MEH-PPV:PCL electrospun nanofibers determined by XPS survey scans.

Material	C1s (%)	O1s (%)	N1s (%)	Cl2p (%)	Si2p (%)	Ca2p (%)
SEN1	78.7	21.1	-	0.1	0.4	0.3
SEN2	76.9	22.2	-	0.3	0.5	-
SEN3	77.3	22.4	-	0.4	0.3	-
SEN4	76.1	21.2	-	1.9	1.1	0.2
AFSEN1	56.1	30.7	9.8	0.1	3.4	-
AFSEN2	60.7	27.2	8.4	0.4	3.7	-
AFSEN3	69.2	26.7	4.6	0.3	0.7	-
AFSEN4	66.2	24.8	4.3	1.5	3.7	-
HFSEN1	52.7	32.1	15.5	0.1	0.7	-
HFSEN2	57.9	27.7	11.3	0.4	3.1	-
HFSEN3	67.7	23.5	4.2	0.4	4.6	0.3
HFSEN4	70.5	23.7	3.7	1	1.1	-

Table 6.7. Details of peak deconvolution of C1s narrow scan spectra of SEN1, AFSEN1, and HFSEN1.

Chemical group	Peak BE (eV)	Atomic % SEN1	Peak BE	Atomic % AFSEN1	Peak BE (eV)	Atomic % HFSEN1
C-C, C-H	284.99	65.82	285.17	44.19	285.02	57.24
C-N	-	-	285.95	12.69	286.03	11.5
C-OH, C-O	286.35	16.59	286.51	30.86	286.60	10.98
C=O	287.79	5.03	287.83	7.68	287.76	7
O-C=O	288.96	12.56	289.22	4.59	289.02	12.28

In addition, the C1s spectrum of AFSEN1 reveals remarkable increase in atomic percent of C-O species, which can be attributed to the incorporation of APTES on the surface consisting of three C-O bonds per molecule. The results confirm the successful incorporation of amine functionality on the surface of the blended MEH-PPV:PCL electrospun nanofibers after surface functionalization by APTES and 1,6-Hexanediamine. It is important to note that the C1s spectra of SEN1, AFSEN1 and

HFSEN1 reveals two common peaks corresponding to C=O and O=C-O species. The O=C-O species is ascribed to the ester groups of PCL [472, 473], while C=O species is potentially a contamination of amide in dimethylformamide (DMF) left out after electrospinning. DMF was used as a solvent during electrospinning of MEH-PPV:PCL blend. Although, the as-electrospun meshes were air dried for 24 h in order to evaporate the solvents, DMF may be still there since it is generally used as a solvent of low evaporation rate [474]. Moreover, the non-functionalized SEN1, AFSEN1 and HFSEN1 were cleaned with rigorous washing with alcohol/water solution and deionized water prior to XPS characterization. It seemed that the cleaning process is also unable to remove DMF and it is obvious because DMF can be hydrolyzed only by strong acids and bases, especially at elevated temperatures [474]. This suggest that the C=O species arises from the amide of DMF only, which is common to all the electrospun meshes.

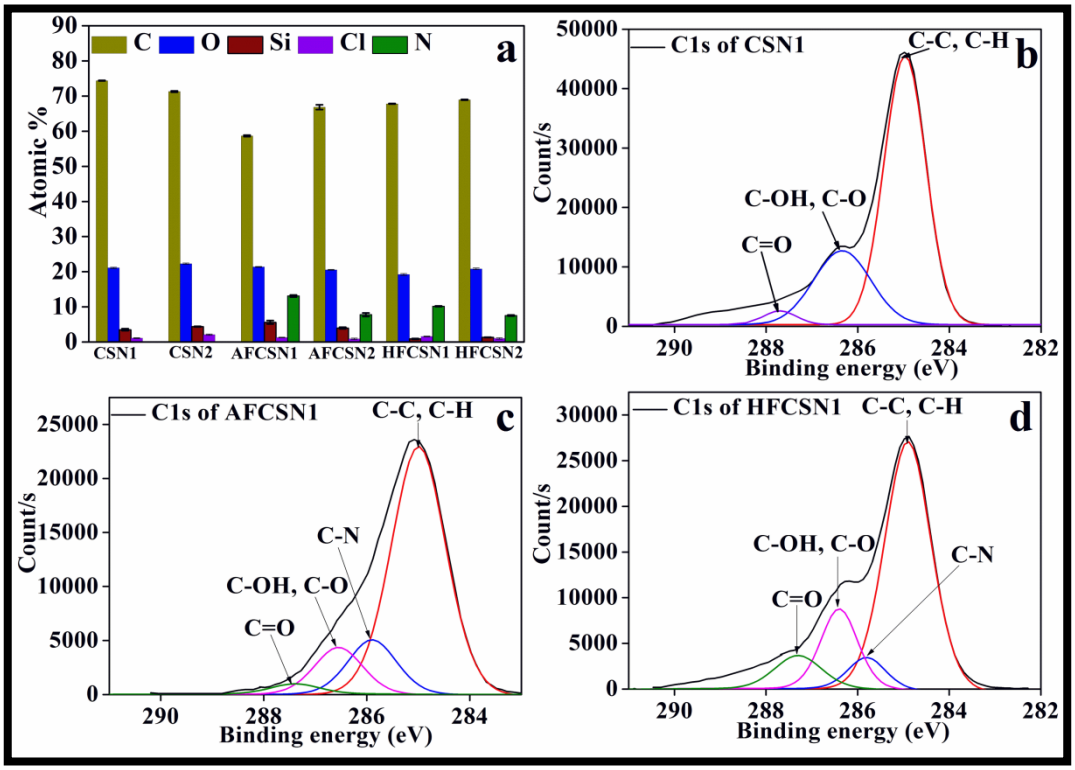

Figure 6.19. (a) Elemental composition in different cores-sheath MEH-PPV:PCL electrospun nanofibers before and after functionalization. Peak deconvolution of high-resolution C1s XPS spectra of (b) CSN1 (c) AFCSN1 and (d) HFCSN1.

Table 6.8. Elemental composition of non-functionalized and functionalized core-sheath MEH-PPV:PCL electrospun nanofibers determined by XPS survey scans.

Material	C1s (%)	O1s (%)	N1s (%)	Cl2p (%)	Si2p (%)
CSN1	74.4	21.1	-	1.1	3.5
CSN2	71.3	22.3	-	2.1	4.4
AFCSN1	58.7	21.4	13.1	1.3	5.6
AFCSN2	66.83	20.56	7.79	0.9	3.98
HFCSN1	67.81	19.23	10.16	1.6	0.9
HFCSN2	68.94	20.83	7.52	1	1.3

Table 6.9. Details of peak deconvolution of C1s narrow scan spectra of CSN1, AFCSN1, and HFCSN1.

Chemical group	Peak BE (eV)	Atomic % CSN1	Peak BE	Atomic % AFCSN1	Peak BE (eV)	Atomic % HFCSN1
C-C, C-H	284.99	78.59	285.01	56.63	284.94	63.25
C-N	-	-	285.91	18.95	285.76	9.65
C-OH, C-O	286.35	17.86	286.55	21.12	286.44	17.03
C=O	287.29	3.09	287.41	3.38	287.29	10.03

Elemental analysis of the non-functionalized and functionalized core-sheath nanofibers are shown in **Figure 6.19 (a)**. Analysis of surface elemental composition by XPS survey scans demonstrate the presence of nitrogen (N1s) on the surface of AFCSN1 (13.1%), AFCSN2 (7.79%), HFCSN1 (10.16%), and HFCSN2 (7.53%) indicating incorporation of amine functionality [**Table 6.8**]. It further shows that carbon (C1s) and oxygen (O1s) are the major compositions of the electrospun nanofibers, with trace amounts of silicon (Si2p) as external contaminant [**Table 6.8**]. The presence of atomic chlorine (Cl2p) has been marked in CSN1 (1.1%) and CSN2 (2.1%), which indicates the doping level in MEH-PPV by $FeCl_3$. Conductive properties of the core-sheath nanofibers are not much affected after surface functionalization as trace amount of chlorine was still present in AFCSN1 (1.3%), AFCSN2 (0.9%), HFCSN1 (1.6%) and HFCSN2 (1.0%) [**Table 6.8**]. The C1s core-level XPS spectra along with their peak deconvolution of CSN1, AFCSN1, and HFCSN1 are shown in **Figure 6.19 (b), (c) & (d)**, respectively. The details of peak

deconvolution of C1s spectra of these core-sheath nanofibers are presented in **Table 6.9**. The C1s core-level XPS spectrum of the non-functionalized CSN1 can be deconvoluted into three peak components at about 284.99, 286.35 and 287.29 eV corresponding to C-C/C-H, C-OH/C-O and C=O species, respectively [**Table 6.9**]. The C1s core-level spectra of AFCSN1 and HFCSN1 also demonstrate the presence of these three species in addition to a new peak at about 285.91 eV for C-N species, suggesting incorporation of amine functionality on the surface of the core-sheath nanofibers after functionalization [**Table 6.9**] [366, 472, 473]. The C1s core-level XPS spectra of the core-sheath nanofibers further demonstrate that there are no XPS peak for O-C=O species corresponding to ester groups of PCL, which confirms the lone presence of MEH-PPV on the sheath of the core-sheath nanofibers.

6.2.7.3 Mechanisms of surface functionalization

The blended MEH-PPV:PCL electrospun meshes and the electrospun core-sheath MEH-PPV:PCL meshes were surface functionalized by APTES and 1,6-Hexanediamine in order to introduce amine functionality on the surface. FT-IR and XPS results confirmed the incorporation of the amine functionality on the surface of the blended and core-sheath nanofibers after surface functionalization by APTES and 1,6-Hexanediamine, as described above. Based on the FT-IR and XPS results, the interaction mechanisms of PCL surface with APTES and 1,6-Hexanediamine have been proposed in **Scheme I** and **Scheme II** of **Figure 6.20**, respectively. Similarly, the probable interaction mechanisms of MEH-PPV with APTES and 1,6-Hexanediamine have been proposed based on the FT-IR and XPS results in **Scheme III** and **Scheme IV** of **Figure 6.21**, respectively.

The electrospun nanofibers, prepared from a blend of MEH-PPV and PCL at different volume ratio by simple electrospinning process, are believed to be a mixture of both MEH-PPV and PCL. During surface functionalization process, both MEH-PPV and PCL are believed to take part as suggested by FT-IR and XPS analysis. This means surface functionalization is expected to cause to aminolysis of MEH-PPV and PCL simultaneously.

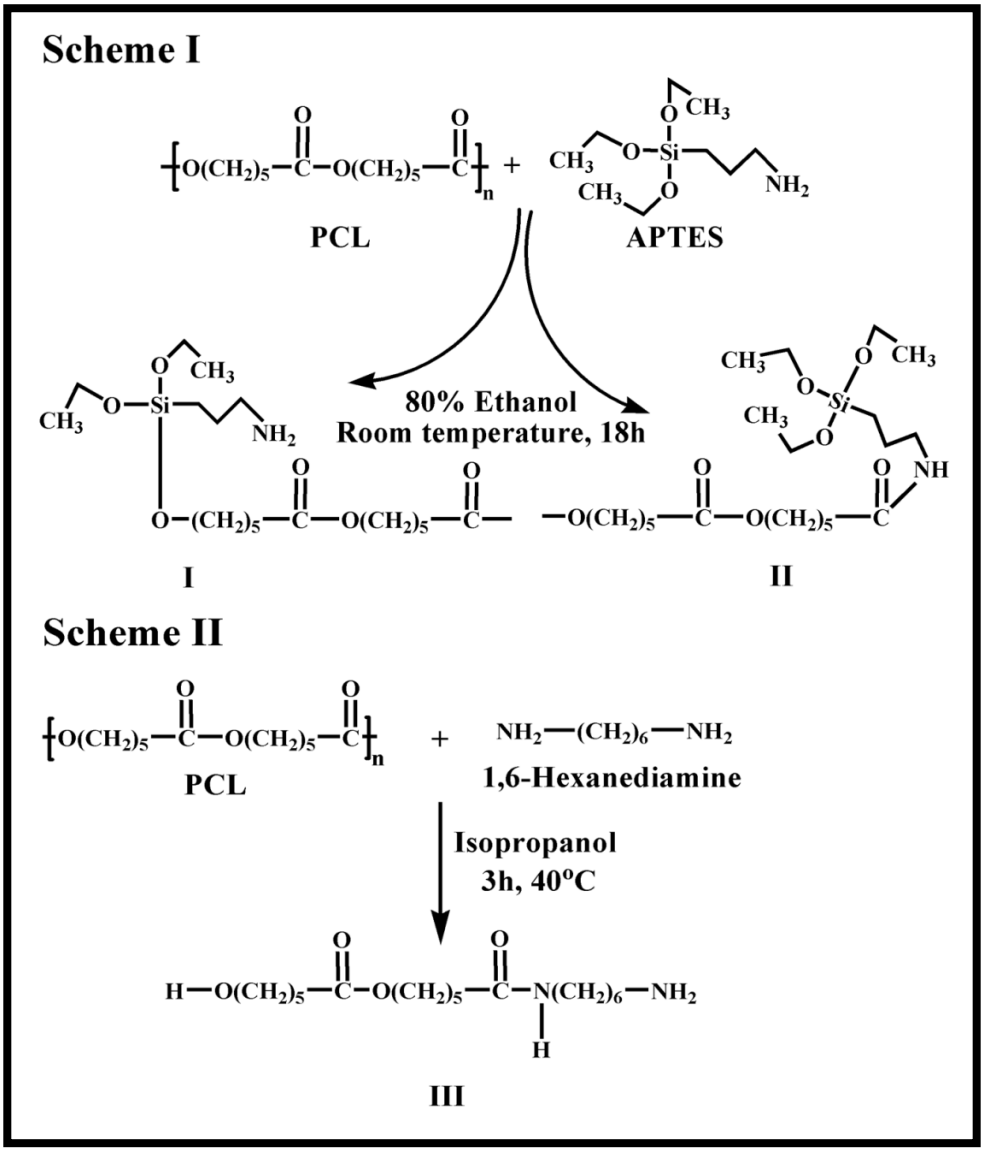

Figure 6.20. Probable interaction mechanisms of PCL with APTES (Scheme I) and MEH-PPV with 1,6-Hexanediamine (Scheme II) based on XPS and FTIR results.

We have proposed that PCL can interact with APTES in two ways as shown in **Scheme I**. APTES hydrolyzes rapidly in aqueous solution producing ethanol and trisilanols [50]. Only Si-C bond in APTES is hydrolytically stable and all ethoxy groups attached to Si are easily hydrolyzed in solution [440, 441, 466, 476]. Therefore, we speculate that silicon (Si) which is attached to primary amine ($-NH_2$) through three ethyl groups is stable enough in ethanol/water solution. The remaining ethoxy groups get hydrolyzed in solution leaving unsaturation in Si. On the other hand, PCL possess abundant ester groups (-COO-), which makes it viable the interaction of the unsaturated Si with the highly oxygenated PCL through formation

Si-O-C bond forming the final product **I** as shown in **Scheme I** [**Figure 6.20**]. This proposition is supported by the appearance of vibrational bands for Si-O bond with significantly higher intensities in the FT-IR spectra of APTES functionalized blended nanofibers [**Figure 6.16 (a)**]. Besides, the C1s core-level spectrum of AFSEN1 demonstrate slightly higher atomic percent of C=O in amide, indicating possible interaction of the primary amine (-NH_2) of APTES with the ester groups (-COO-) of PCL through secondary amide bond (-CONH-) formation, which gives the final product **II** as shown in Scheme I [**Figure 6.20**].

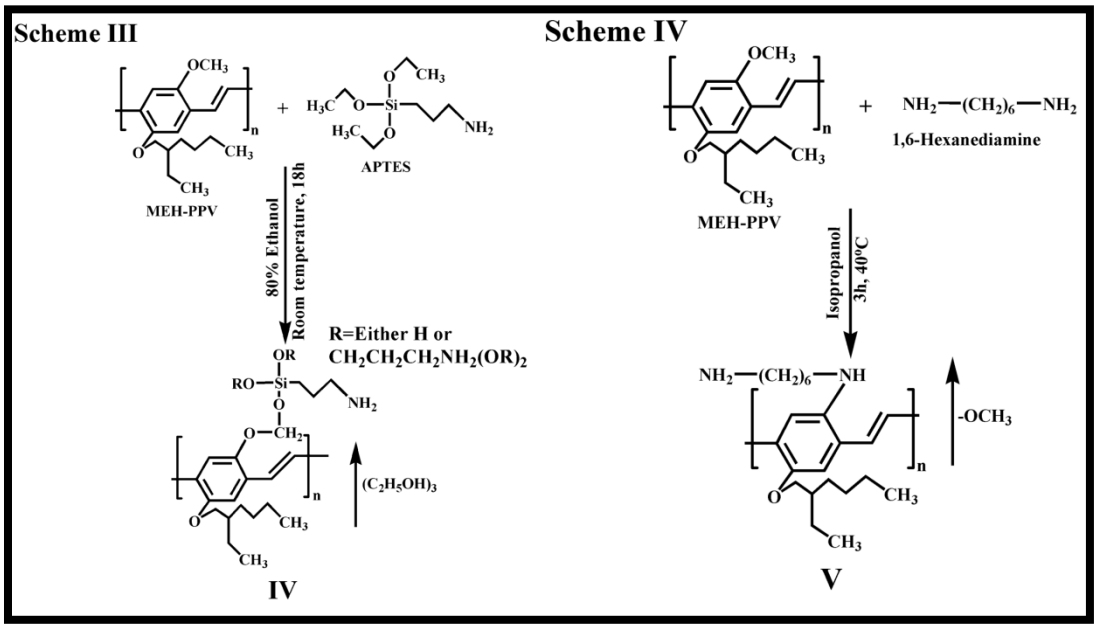

Figure 6.21. Probable interaction mechanisms of MEH-PPV with APTES (Scheme III) and MEH-PPV with 1,6-Hexanediamine (Scheme IV) based on XPS and FTIR results.

Turning on to the interaction mechanisms of PCL with 1,6-Hexanediamine, the ester groups (-COO-) of PCL interact with 1,6-Hexanedimaine through amide bond formation as depicted in **Scheme II** forming the final product **III** [**Figure 6.20**]. This proposition is also in agreement with FT-IR results (distinct C=O stretching and N-H bending in amide at about 1640 cm^{-1} and 1550 cm^{-1}, respectively) and XPS results (peak BE at about 287.83 eV corresponding C=O in amide with higher atomic percent), which confirms the amide bond formation between PCL and 1,6-Hexanediamine.

In case of core-sheath nanofibers, PCL is in the core of the electrospun nanofibers and hence, it will not interact with the functionalizing agents. Therefore, MEH-PPV, being the sheath material, has been taken into account to predict the functionalization mechanisms of the core-sheath nanofibers. During surface functionalization process, APTES in 80% ethanol solution undergoes hydrolysis and reacts with methoxy group in phenylene ring of MEH-PPV giving rise to the final product **IV** as shown in **Scheme III** of **Figure 6.21 [477]**. This proposition is also supported by the FT-IR results (Si-O bond vibration with slightly higher intensity in the range 1000-1100 cm^{-1}) [**Figure 6.17 (a)**] and XPS results (higher atomic percent of C-O species in C1s spectrum of AFCSN1) [**Figure 6.19 (c)**].

Scheme IV shows that 1,6-Hexanediamine can interact with MEH-PPV as follows: the nitrogen in one of the secondary amines of 1,6-Hexanediamine attacks the carbonyl carbon, forming a tetrahedral intermediate [478, 479]. Afterwards, the -OCH_3 (methoxy group in phenylene ring of MEH-PPV) leaves and the new C-N bond is formed giving the final product **V** as shown in **Scheme IV** [**Figure 6.21**]. This proposition is supported by FT-IR and XPS results as well as discussed in **Section 6.2.7.1** and **Section 6.2.7.2**.

6.3 Biological characterization

6.3.1 Hemolysis activity assay

The hemolysis activity of different blended MEH-PPV:PCL electrospun nanofibers and electrospun core-sheath MEH-PPV:PCL nanofibers is shown in **Figure 6.22 (a) & (b)**. The hemolysis activity of pure PCL (2.98%) is less than 5%, which indicates its hemocompatibility behaviour, while pure MEH-PPV (16.43%) has been found to hemolytic [**Figure 6.22 (a) & (b)**]. The biocompatibility of PCL is very well known, however, the hemocompatibility of MEH-PPV has been tested for the first time. **Figure 6.22 (a)** shows that the non-functionalized and APTES functionalized blended MEH-PPV:PCL electrospun meshes exhibit more than 5% hemolysis activity except the non-functionalized SEN1(4.5%) and functionalized AFSEN1 (4.73%). It has been observed that the blended nanofibers with increasing concentration of MEH-PPV reveal higher hemolytic activity due to the intrinsic hemolytic nature of MEH-PPV. The higher hemolytic activity of the APTES functionalized blended nanofibers except AFSEN1, can be ascribed due to the electrostatic interaction of the highly oxygenated

surface of the nanofibers with cell surface leading to cell rupture [319]. Interestingly, the 1,6-Hexanediamine blended nanofibers demonstrate significantly lower hemolysis activity when compared to that of the non-functionalized nanofibers ($p \leq 0.01$). It is because the incorporated non-toxic amine functionalities interact with cell surface covalently, possibly through formation of amide bond.

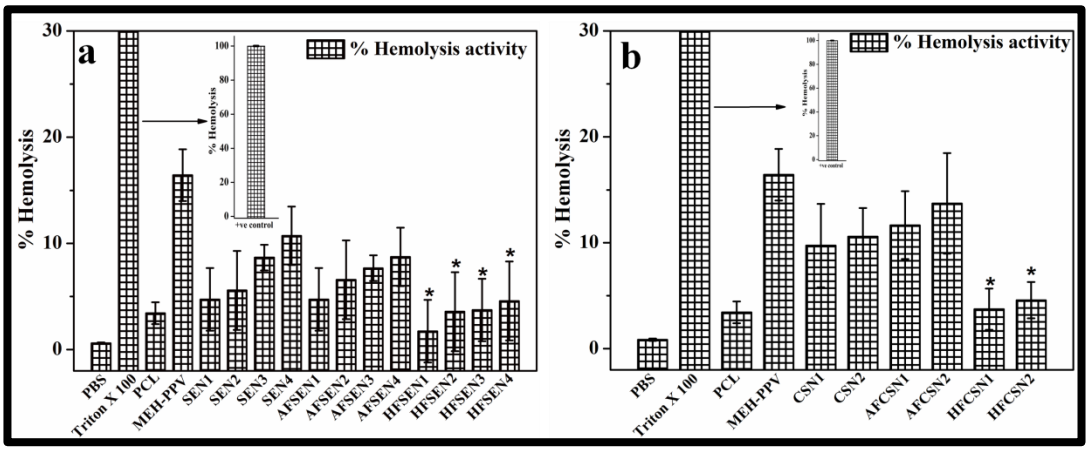

Figure 6.22. Percentage of hemolysis (Mean ± S.D, n=3) shown by the non-functionalized and functionalized (a) blended MEH-PPV:PCL electrospun meshes and (b) core-sheath electrospun meshes as compared to negative control (Phosphate buffer saline, pH= 7.4) and positive control (Triton X 100).

The non-functionalized and APTES functionalized core-sheath nanofibers have been also found to be hemolytic as they exhibit more than 5% hemolysis activity due to MEH-PPV on the sheath of the nanofibers and electrostatic interaction of the APTES functionalized surface with the RBCs. In contrast, the 1,6-Hexanediamine functionalized nanofibers have been found to be hemocompatible due to the incorporated amino groups on the surface. The hemolysis activity of HFCSN1 and HFCSN2 is statistically different from their non-functionalized counterparts at $p \leq 0.01$. It is important to note that APTES functionalized surfaces are highly oxygenated along with one amino group per APTES molecule, while 1,6-Hexanediamine functionalized surfaces possess one conjugated and one free amino groups leading to less probability of the electrostatic interaction with the cell surface.

6.3.2 MTS proliferation assay

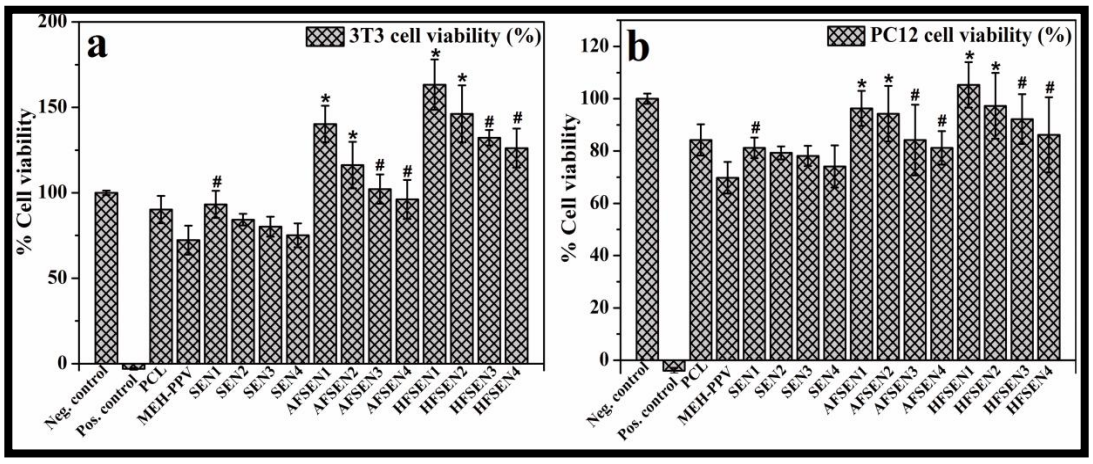

Figure 6.23. Percentage cell viability on different blended MEH-PPV:PCL electrospun meshes in direct contact after 24 h of culture as compared to tissue culture plastic (TCP) as a negative control and tert butyl maleate as a positive control. (a) viability of 3T3 fibroblasts and (b) viability of PC12 cells expressed as percentage of negative control. Data were Mean ± S.D, n=4.* and # indicate significance difference at $p \leq 0.01$ and $p \leq 0.05$ between the functionalized and non-functionalized blended electrospun meshes.

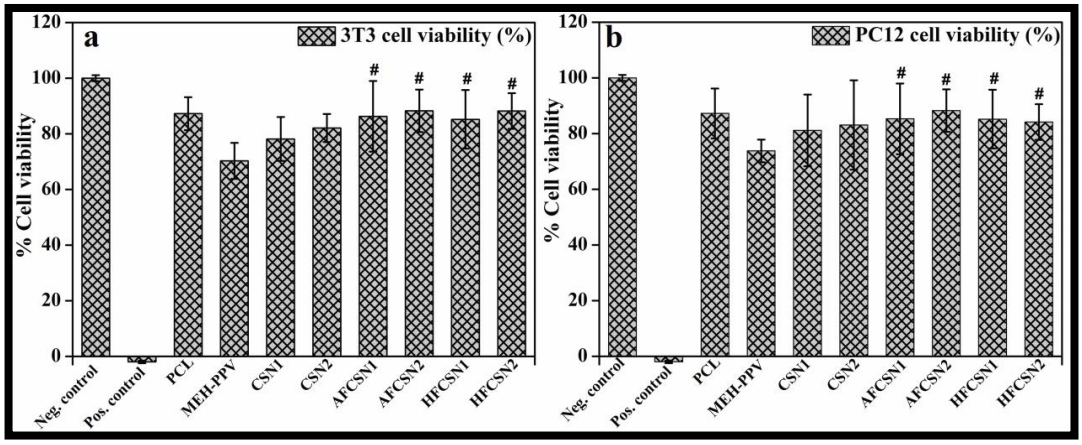

Figure 6.24. Percentage cell viability on different electrospun core-sheath MEH-PPV:PCL meshes in direct contact after 24 h of culture as compared to tissue culture plastic (TCP) as a negative control and tert butyl maleate as a positive control. (a) viability of 3T3 fibroblasts and (b) viability of PC12 cells expressed as percentage of negative control. Data were Mean ± S.D, n=4. # indicates significance difference at

$p \leq 0.01$ and $p \leq 0.05$ between the functionalized electrospun meshes and their non-functionalized counterparts.

Filipa Pires *et al.* reported the non-cytotoxic effect of extract of MEH-PPV with L929 fibroblasts [480], although cytotoxicity of MEH-PPV or its composites has not been studied in direct contact with mammalian cells. The MTS proliferation assay was performed using 3T3 fibroblasts and PC12 cells in direct contact with all the electrospun meshes including pure MEH-PPV and PCL to investigate the cytotoxic effect of these materials with mammalian cells. The pure PCL shows more than 80% of 3T3 and PC12 cell viability, whereas pure MEH-PPV demonstrate around 70% of 3T3 and PC12 cell viability indicating slightly less cytocompatibility from the accepted cell viability of 80% for biocompatible materials [**Figure 6.23 & Figure 6.24**] [411]. Intriguingly, when blended with PCL, the cytotoxic effect was reduced significantly ($p \leq 0.01$) for all the electrospun meshes. The 3T3 and PC12 cell viability on the non-functionalized blended MEH-PPV:PCL electrospun nanofibers decrease with increase in MEH-PPV concentration and with decrease in fiber diameter [**Figure 6.23 (a) & (b)**]. It is due to toxic behaviour of MEH-PPV as described above. Moreover, the fiber diameter has been reported to affect the cell viability. This observation applies to the core-sheath nanofibers as well, although core-sheath nanofibers have MEH-PPV as sheath material. However, the improved cell viability can be attributed to the nanofiber feature, which is not present in pure MEH-PPV. The non-functionalized and functionalized core-sheath electrospun meshes also exhibit nearly or more than 80% of 3T3 and PC12 cell viability [**Figure 6.24 (a) & (b)**]. After surface functionalization by APTES and 1,6-Hexanediamine, the blended nanofibers demonstrate more than 100% or nearly comparable 3T3 cell viability to the negative control. The PC12 cell viability is more than 80% on the APTES and 1,6-Hexanediamine functionalized blended MEH-PPV:PCL electrospun meshes [**Figure 6.23 (a) & (b)**]. The results suggest that the incorporated amino groups on the surface of different electrospun meshes contribute towards the improved 3T3 and PC12 cell viability. In case of the blended MEH-PPV:PCL nanofibers, this difference in cell viability on the non-functionalized and functionalized meshes is statistically significant at $p \leq 0.01$ (for SEN1 vs AFSEN1, SEN1 *vs* HFSEN1, SEN2 *vs* AFSEN2, SEN2 *vs* HFSEN2) and at $p \leq 0.05$ (for SEN3 *vs* AFSEN3, SEN4 *vs* HFSEN4, SEN3 *vs* AFSEN3, SEN4 *vs* HFSEN4). In case of the core sheath nanofibers, the difference

in cell viability on the functionalized meshes is statistically significant at $p \leq 0.01$. It has been also noted that fiber diameter has significant impact on cell viability as mentioned above. In case of blended nanofibers, the difference in cell viability on SEN1 and its functionalized counterparts, i.e., AFSEN1 and HFSEN1 is statistically different from the cell viability on SEN4 and its functionalized counterparts, i.e., AFSEN4 and HFSEN4, at $p \leq 0.01$. Similarly, the statistical difference exists between AFSEN2 vs AFSEN4, HFSEN2 vs HFSEN4, AFSEN3 v AFSEN4 and HFSEN3 vs HFSEN4 at $p \leq 0.05$. However, such significant difference does not exist in case of the core-sheath nanofibers, although they much larger fiber diameter. Here, MEH-PPV on the sheath limits the biocompatibility of the core-sheath nanofibers, although they show nearly or more than 80% of cell viability. Furthermore, the cell viability on the APTES functionalized blended electrospun meshes and 1,6-Hexanediamine functionalized blended electrospun meshes is statistically different at $p \leq 0.01$. However, in case of the core-sheath nanofibers such differences have not been observed. These results confirm that surface functionalization by both APTES and 1,6-Hexanediamine improve the biocompatibility of the electrospun nanofibers indicating their potential in tissue engineering applications.

6.4 Enhanced 3T3 fibroblast adhesion, spreading and proliferation on amine functionalized electrospun MEH-PPV:PCL nanofibers

6.4.1 Live/dead assay

Since the blended and electrospun core-sheath nanofibers alone or after surface functionalization demonstrate considerable cytocompatibility in MTS assay, it is important to study cell morphology, adhesion and spreading on those meshes to evaluate their possible use as biomaterial scaffold in tissue engineering. For that purpose, the live/dead assay was carried out to visualize the viable 3T3 fibroblasts and the changes in their morphology with time on non-functionalized and surface functionalized electrospun meshes. The fluorescent images of 3T3 fibroblasts cultured for 24 h and 48 h on different blended electrospun meshes and core-sheath electrospun meshes were acquired by confocal microscope after washing and staining the cells with calcein AM, EthD-1, and DAPI. Representative confocal images of 3T3

fibroblasts after 24 h and 48 h of culture on the different blended electrospun meshes and core-sheath electrospun meshes are shown in **Figure 6.25** and **Figure 6.26**, respectively.

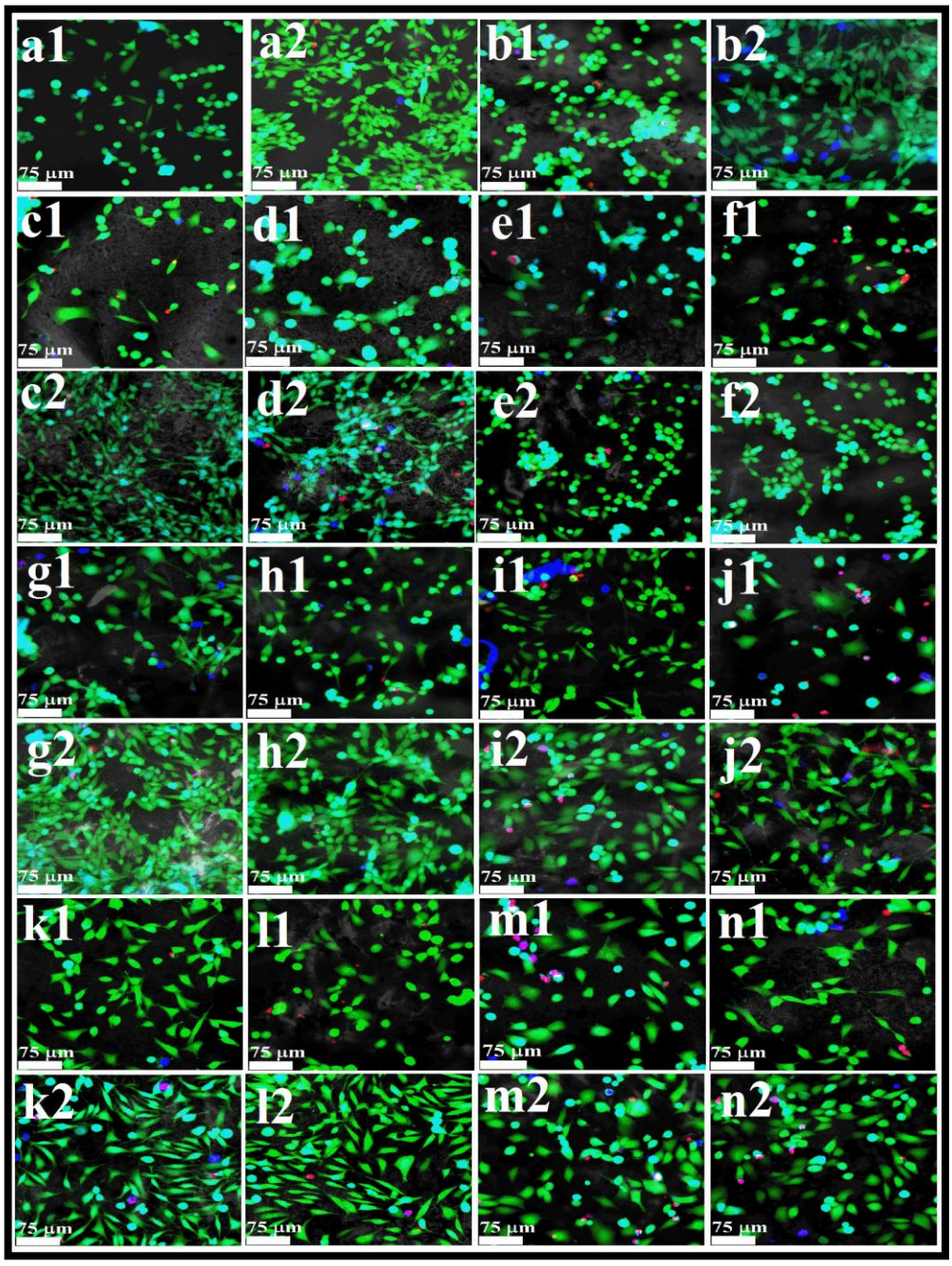

Figure 6.25. Representative confocal images with phase contrast overlay of 3T3 fibroblasts stained with calcein AM (green), EthD-1 (red) and DAPI (blue) during live/dead assay after 24 of culture on control tissue culture plastic (TCP) (a1), electrospun PCL mesh (b1), SEN1 (c1), SEN2 (d1), SEN3 (e1), SEN4 (f1), AFSEN1 (g1), AFSEN2 (h1), AFSEN3 (i1), AFSEN4 (j1), HFSEN1 (k1), HFSEN2 (l1),

HFSEN3 (m1) and HFSEN4 (n1). Similarly, representative live/dead stained confocal images of 3T3 fibroblasts after 48 of culture on control tissue culture plastic (TCP) (a2), electrospun PCL mesh (b2), SEN1 (c2), SEN2 (d2), SEN3 (e2), SEN4 (f2), AFSEN1 (g2), AFSEN2 (h2), AFSEN3 (i2), AFSEN4 (j2), HFSEN1 (k2), HFSEN2 (l2), HFSEN3 (m2) and HFSEN4 (n2) [Scale bar=75 μm].

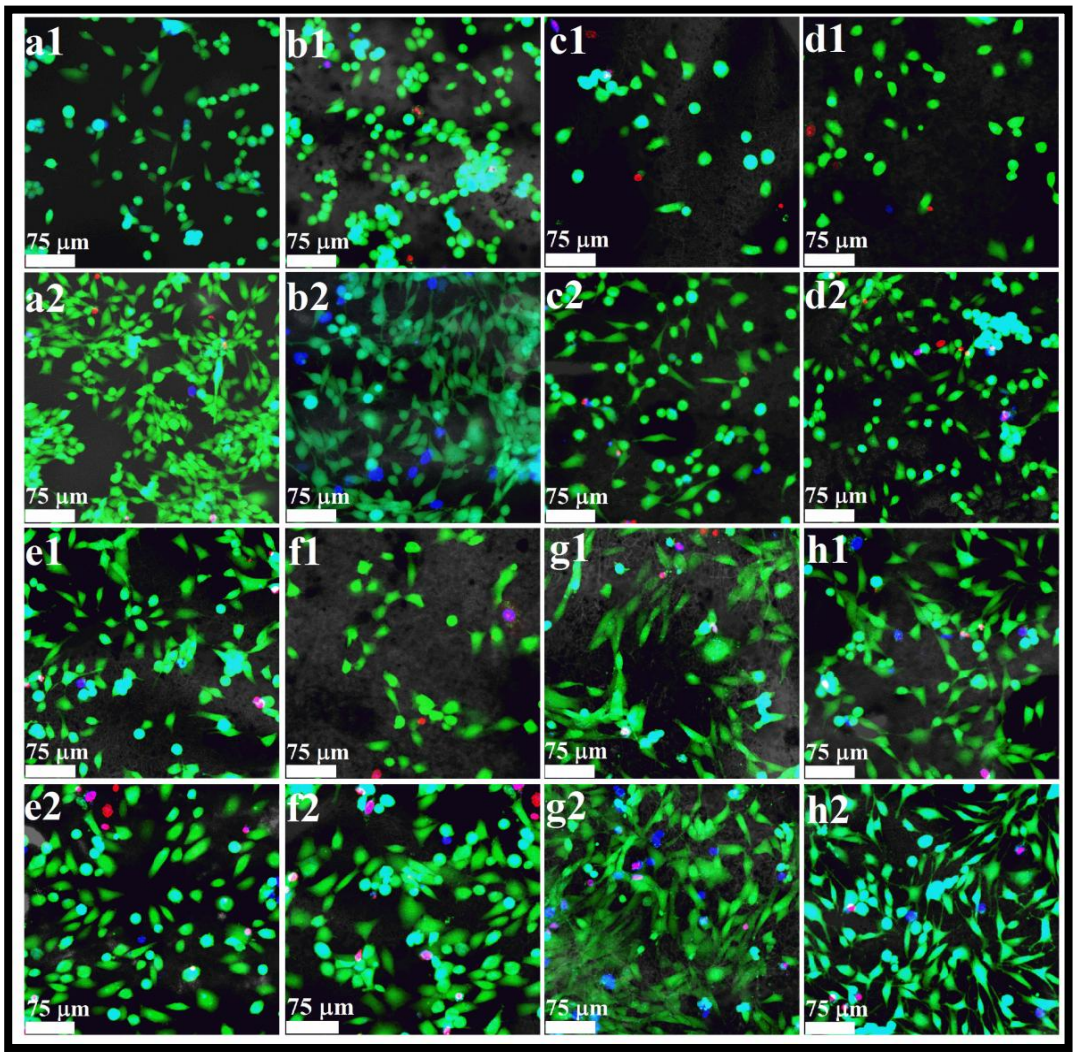

Figure 6.26. Representative confocal images with phase contrast overlay of 3T3 fibroblasts stained with calcein AM (green), EthD-1 (red) and DAPI (blue) during live/dead assay after 24 of culture on control tissue culture plastic (TCP) (a1), electrospun PCL mesh (b1), CSN1 (c1), CSN2 (d1), AFCSN1 (e1), AFCSN2 (f1), HFCSN1 (g1) and HFCSN2 (h1). Similarly, representative live/dead stained confocal images of 3T3 fibroblasts after 48 of culture on control tissue culture plastic (TCP)

(a2), electrospun PCL mesh (b2), CSN1 (c2), CSN2 (d2), AFCSN1 (e2), AFCSN2 (f2), HFCSN1 (g2) and HFCSN2 (h2) [Scale bar=75 μm].

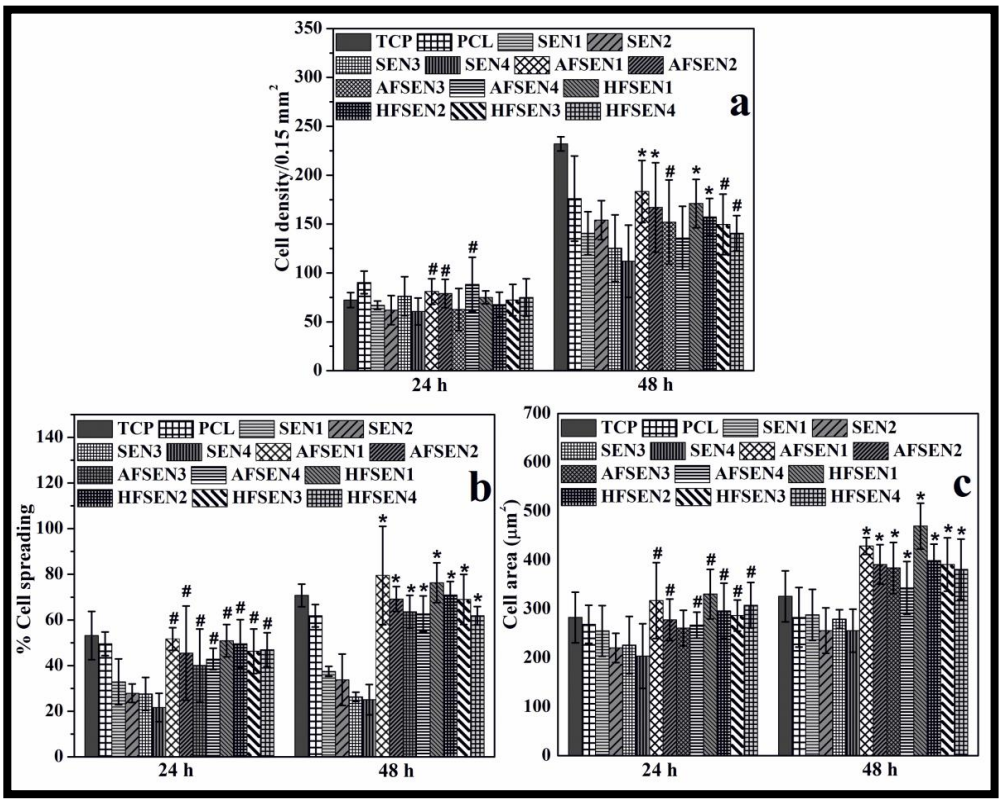

Figure 6.27. Quantitative analysis of (a) cell density per field of view, (b) cell area (average area covered by single cell) and (c) percentage of cell spreading on the non-functionalized and functionalized blended MEH-PPV:PCL electrospun meshes. Data were presented as Mean ± S.D, n=6.* and # indicate statistically significant difference at $p \leq 0.01$ and $p \leq 0.05$, respectively.

The green-fluorescent calcein AM can be visualized throughout almost all of the cell bodies seeded on different scaffolds indicating the viable cells, except few dead cells (red) [**Figure 6.25 & Figure 6.26**]. This again confirms the cytocompatibility of these electrospun meshes. The cells were also stained with DAPI for nuclei staining; however, only a few DAPI stained nuclei (blue) can be seen. This may be because of the staining of the cells were performed without fixing. It is evident from the confocal images that the cells seeded on surface functionalized electrospun meshes adopted more spreading morphology, i.e., they adopted a flattened, polygonal or elongated shape. To determine the effect of surface functionalization on different cellular

activities such as cell density, projected cell area and percentage of cell spreading were quantified using the confocal images of 3T3 fibroblasts seeded on different scaffolds with the help of ImageJ software. Cells seeded on TCP and electrospun were also analyzed and treated as control.

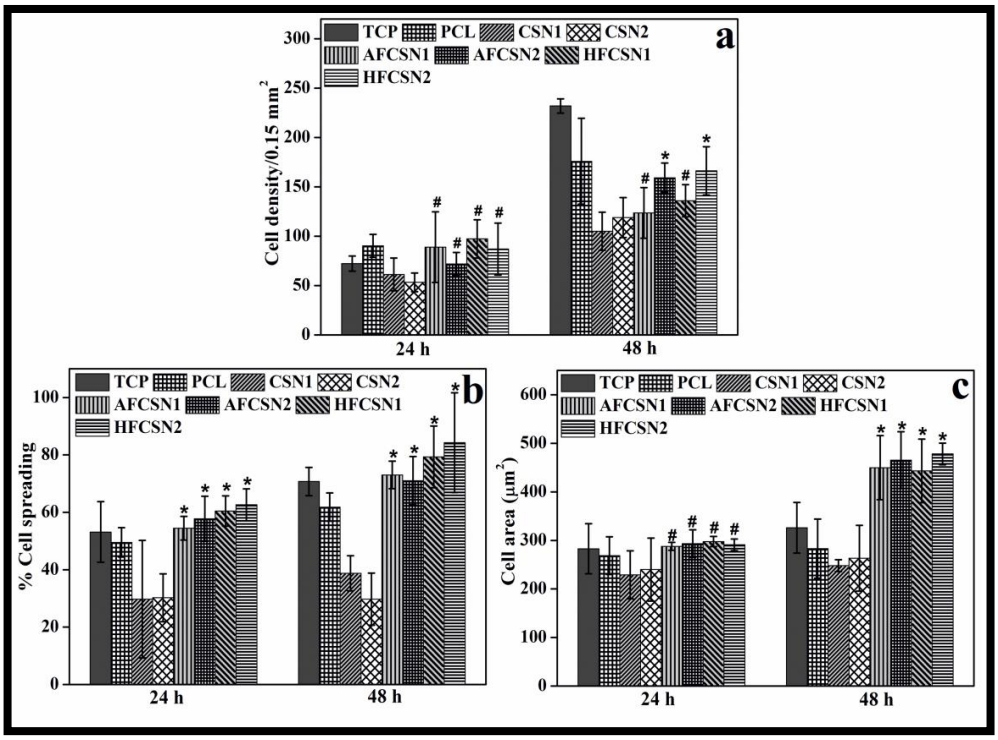

Figure 6.28. Quantitative analysis of (a) cell density per field of view, (b) cell area (average area covered by single cell) and (c) percentage of cell spreading on the non-functionalized and functionalized electrospun core-sheath MEH-PPV:PCL meshes. Data were presented as Mean ± S.D, n=6. * and # indicate statistically significant difference at $p \leq 0.01$ and $p \leq 0.05$, respectively.

Qauantitative analysis of cell density, projected cell area and percentage of cell spreading on the non-functionalized and functionalized blended MEH-PPV:PCL electrospun meshes are presented in **Figure 6.27**. **Figure 6.27 (a)** shows that the number of viable 3T3 cells after 24 h and 48 h culture on the APTES functionalized and 1,6-Hexanediamine functionalized blended electrospun meshes are greater than those on the non-functionalized blended electrospun meshes. However, after 24 h of culture, the statistically significant difference exists between SEN1 *vs* AFSEN1, SEN2 *vs* AFSEN2 and SEN1 *vs* HFSEN1 at $p \leq 0.05$. After 48 h of culture, the cell densities on the functionalized blended eletrospun meshes are significantly higher

than that of the non-functionalized meshes. Specifically, the cell densities per field of view (0.15 mm^2) on AFSEN1 (183 ± 31), AFSEN2 (167 ± 45), HFSEN1(171 ± 25) and HFSEN2 (157 ± 19) are statistically different from their non-functionalized counterparts, i.e., SEN1 (145 ± 22) and SEN2 (154 ± 20) at $p \leq 0.01$, whereas the cell density on AFSEN3 (152 ± 43), AFSEN4 (135 ± 32), HFSEN3 (149±31) and HFSEN4 (140 ± 18) is statistically significant from their non-funtionalized counterparts, i.e., SEN3 (125 ± 34) and SEN4 (112 ± 37) at $p \leq 0.05$ [**Figure 6.27 (a)**]. The average cell area of ecah 3T3 cell after 24 h of culture on each of the functionalized blended electrospun meshes is higher than that of their non-functionalized counterparts and this difference is statistically significant at $p \leq 0.05$ [**Figure 6.27 (b)**]. After 48 h of culture, the projected cell area on the functionalized blended electrospun meshes incereases significantly from their non-functionalized counterparts at $p \leq 0.01$ [**Figure 6.27 (b)**]. The pecentage of cell spreading also on the functionalized blended electrospun meshes after 24 h and 48 h of culture is significantly better than that of their non-functionalized counterparts after 24 h ($p \leq 0.05$) and 48 h ($p \leq 0.01$) of culture, respectively [**Figure 6.27 (c)**]. It is to be noted that the cell denisty, projected cell area and cell spreading on control PCL after 48 h, are significantly different from those on the surface functionalized blended electrospun meshes after 48 h at $p \leq 0.01$, whereas after 48 h, the projected cell area and cell spreading on control TCP are also statistically different from those on the surface functionalized blended electrospun meshes after 48 h at $p \leq 0.01$.

In case of the electrospun core-sheath nanofibers, cell densities, after cultured for 24 h and 48 h, on AFCSN1 (109 ± 23 and 133 ± 25), AFCSN2 (87 ± 15 and 160 ± 15), HFCSN1 (98 ± 20 and 156 ± 17) and HFCSN2 (107 ± 26 and 177 ± 27) statistically differ from that on CSN1 (61 ± 16 and 109 ± 29) and CSN2 (53 ± 11 and 103 ± 21) at $p \leq 0.05$ [**Figure 6.28 (a)**]. However, cell densities on the controls (TCP and PCL) are not significantly different from that on the surface functionalized electrospun meshes. Quantitative analysis demonstrates that the projected cell area after 24 h and 48 h of culture on surface functionalized electrospun core-sheath meshes are higher than that on the non-functionalized electrospun meshes and the control electrospun PCL mesh and presented in **Figure 6.27 (b)**. These differences are statistically significant at $p \leq 0.01$. However, the statistically significant difference in projected cell area on the control TCP and surface functionalized electrospun core-sheath meshes exists at $\alpha = 0.01$ ($p = 0.007$). Similarly, percent of cell spreading after 24

h and 48 h of culture on surface functionalized electrospun core-sheath meshes are higher than that on non-functionalized electrospun meshes and presented in **Figure 6.27 (c)** and the differences after 24 h and 48 h are statistically significant at $p \leq 0.05$ and $p \leq 0.01$, respectively. There are also significant differences in the extent of cell spreading observed on the controls (TCP and PCL) and the surface functionalized electrospun meshes after 48 h of culture at $\alpha=0.05$ ($p=0.018$). Interestingly, after 24 h also, cell spreading on surface functionalized electrospun meshes is comparable to the controls (TCP and PCL).

The results suggest the enhanced 3T3 fibroblast adhesion, spreading and proliferation on the surface functionalized electrospun meshes is attributed to the incorporation of amine functionality, leading to induce favorable interaction with the receptor proteins on the cell surface. Concurrently, 1,6-Hexanediamine functionalized electropsun meshes (both blended and core-sheath morphology) demonstrate enhanced cellular activities such as projected cell area, cell apreading and cell proliferation (cell density) than that on the APTES functionalized electropsun meshes (both blended and core-sheath morphology). There exists statistically significant difference at $p \leq 0.01$ as well.

However, in case of the blended electrospun meshes, cellular activities quantified in terms of cell density, projected cell area and cell spreading are significantly enhanced on the electrospun meshes with higher fiber diamter and these cellular activities increases in the order of SEN4<SEN3<SEN2<SEN1 (non-functionalized), AFSEN4<AFSEN3<AFSEN2<AFSEN1 (APTES functionalized) and HFSEN4<HFSEN3<HFSEN2<HFSEN1 (1,6-Hexanediamine functionalized). These differences are statistically significant at $p \leq 0.05$. However, the electrospun core-sheath meshes have not such significant impact of fiber diamter on the cellular activities.

6.4.2 3T3 cell attachment

To further confirm the results described above, 3T3 cells cultured for 3 days on the blended MEH-PPV:PCL electrospun nanofibers and electrospun core-sheath MEH-PPV:PCL nanofibers were characterized by SEM [**Figure 6.29 & Figure 6.30**]. SEM images reveal that 3T3 cells adhered and spread well on AFSEN1 [**Figure 6.29 (a2)**], AFSEN2 [**Figure 6.29 (b2)**], AFSEN3 [**Figure 6.29 (c2)**], AFSEN4 [**Figure 6.29 (d2)**], HFSEN1 [**Figure 6.29 (a3)**], HFSEN2 [**Figure 6.29 (b3)**], HFSEN3 [**Figure**

6.29 (c3)] and HFSEN4 [**Figure 6.29 (d3)**] as compared to non-functionalized SEN1 [**Figure 6.29 (a1)**], SEN2 [**Figure 6.29 (b1)**], SEN3 [**Figure 6.29 (c1)**] and SEN4 [**Figure 6.29 (d1)**]. Similarly, **Figure 6.30** demonstrates 3T3 fibroblasts enhanced attachement on the APTES functionalized core-sheath electrospun meshes (AFCSN1-**a2** and AFCSN2-**b2**) and the 1,6-Hexanedimaine functionalized core-sheath electrospun meshes (HFCSN1-**a3** and HFCSN2-**b3**) when compared to the non-functionalized core-sheath electrospun fibers (CSN1-**a1** and CSN2-**b1**).

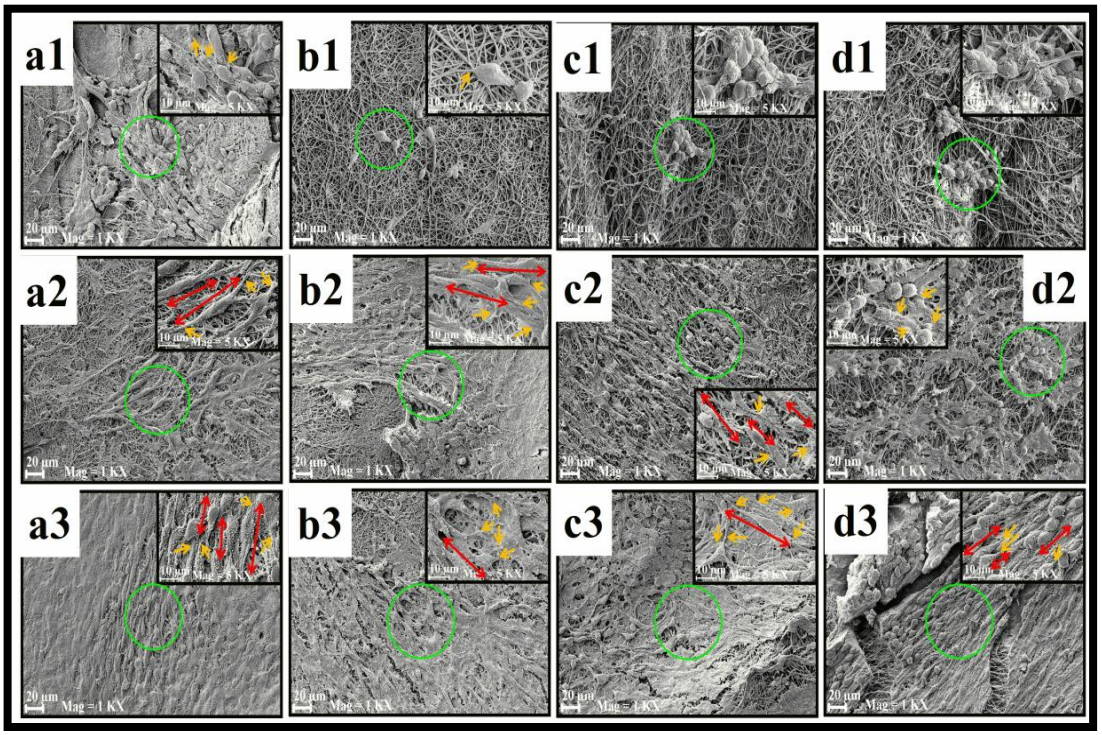

Figure 6.29. Scanning electron micrographs of 3T3 fibroblasts after 3 days culture on SEN1 (a1), SEN2 (b1), SEN3 (c1), SEN4 (d1), AFSEN1 (a2), AFSEN2 (b2), AFSEN3 (c2), AFSEN4 (d2), HFSEN1 (a3), HFSEN2 (b3), HFSEN3 (c3) and HFSEN4 (d3) [Scale bar=20 μm]. Insets of (a1-d3) show magnified image of green circled region [Scale bar=10 μm]. Red and yellow arrows indicate the direction of cell alignment and filopodia/lamellipodia like extensions, respectively.

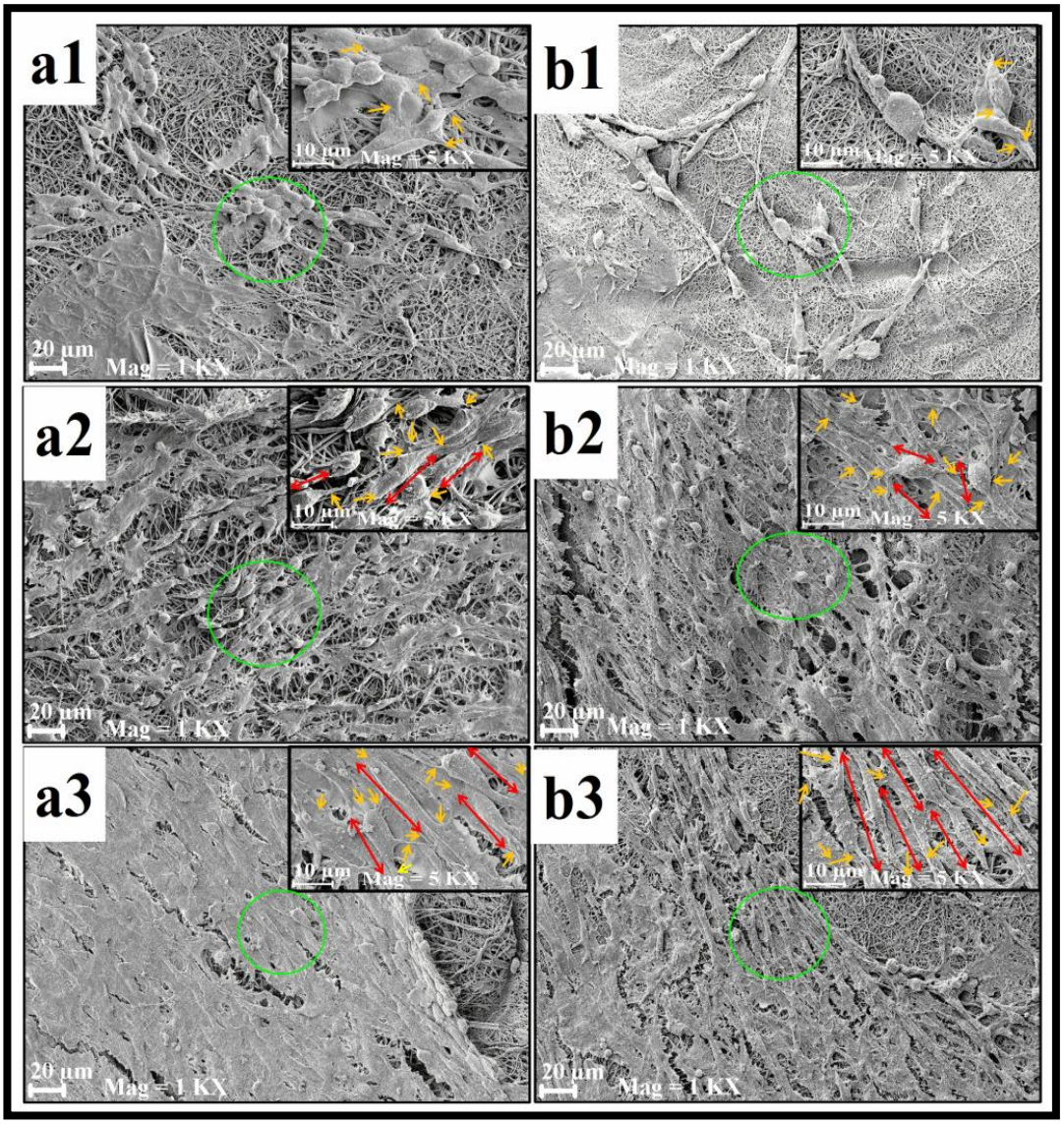

Figure 6.30. Scanning electron micrographs of 3T3 fibroblasts after 3 days culture on CSN1 (a1), CSN2 (b1), AFCSN1 (a2), AFCSN2 (b2), HFCSN1 (a3) and HFCSN2 (b3) [Scale bar=20 µm]. Insets of (a1-b3) show magnified image of green circled region [Scale bar=10 µm]. Red and yellow arrows indicate the direction of cell alignment and filopodia/lamellipodia like extensions, respectively.

Although the nanofibers are randomly oriented, the cells started to align in some particular directions on the surface functionalized meshes with simultaneous formations of filopodia and lamellipodia-like extensions, which are pointed with the help of red, and yellow arrows in the insets of **Figure 6.29 (a2-d3) and Figure 6.30 (a2-b3)**. This observation indicates that the cells on surface functionalized meshes interacted well with the surrounding fibres and started to migrate through the porous

nanofibrous network. The amine functionality on the surface functionalized meshes provides necessary binding sites to the integrin proteins on the cell surface resulting in the formation of focal adhesions; which are confirmed from the appearance of filopodia and lamellipodia-like extensions [**Insets of Figure 6.29 (a2-d3) & Figure 6.30 (a2-b3)**]. This accelerates the cell attachment, followed by cell spreading and migration. In contrast, non-functionalized meshes due to lack of bioactive binding sites show poor cell attachment and morphology as compared to surface functionalized meshes [**Figure 6.29 (a1-d1) & Figure 6.30 (a1-b1)**]. The observed cell attachment on the non-functionalized meshes may be due to the serum proteins adsorbed by the fibres, which offer limited focal adhesions for cell attachment [480].

The SEM analysis further reveal that cells cultured on 1,6-Hexanediamine functionalized electrospun meshes i.e., HFSEN1, HFSEN2, HFSEN3, HFSEN4, HFCSN1 and HFCSN2 appear to be bigger in size and adopt more elongated morphology than that on APTES functionalized electrospun meshes, i.e., AFSEN2, AFSEN3, AFSEN4, AFCSN1 and AFCSN2, which is in agreement with quantitative analysis of live-dead confocal images. These results suggest that surface functionalized electrospun meshes provide a bioactive three-dimensional nanofibrous structure for fibroblast attachment, growth, and migration through contact guidance phenomenon [482].

6.5 PC12 cell behaviour on electrospun MEH-PPV:PCL nanofibers

6.5.1 Beta (III) tubulin immunochemistry

The PC12 cells were cultured for 7 days in differentiating medium on different electrospun MEH-PPV:PCL with and without collagen I coating to investigate the suitability of these materials for neuronal applications. This cell line has been widely used as a model neuronal system. PC12 cells cultured with NGF develop long neurite outgrowth, become electrically excitable and take on many of the biochemical traits of sympathetic noradrenergic neurons [483]. Since, PC12 cells readily adhere to collagen, all the electrospun meshes were coated with collagen I. Collagen I is a fibril forming collagen present in the ECM of the peripheral nervous system (PNS) and plays an important part in the development of the peripheral nervous system as well as in the maintenance of normal peripheral nerve function during adulthood [441].

Immunolabelling with beta (III) tubulin antibody was performed to confirm PC12 cell differentiation into sympathetic neurons. The PC12 cells grown on the uncoated and coated electrospun meshes were labelled with beta (III) tubulin antibody to visualize cytoskeletal microtubules, which are dynamic polymer filaments of alpha and beta tubulin subunits that drive neurite outgrowth and control neuronal morphology [324].

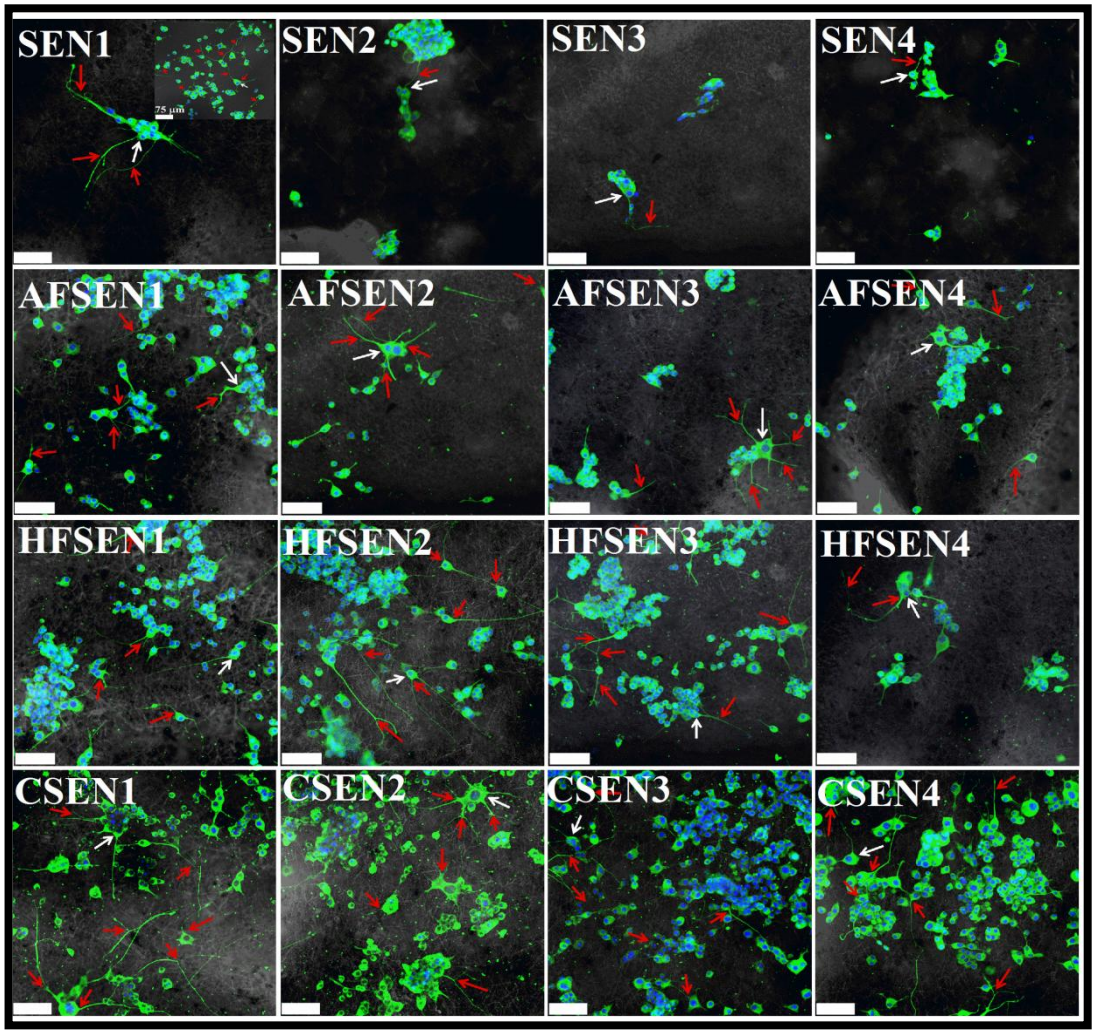

Figure 6.31. Immunolabelling of beta (III) tubulin in differentiated PC12 cells with DAPI stained nuclei after 7 days of culture on the non-functionalized blended MEH-PPV:PCL electrospun meshes (SEN1, SEN2, SEN3 and SEN4), APTES functionalized blended MEH-PPV:PCL electrospun meshes (AFSEN1, AFSEN2, AFSEN3 and AFSEN4), 1,6-Hexanediamine functionalized blended MEH-PPV:PCL electrospun meshes (HFSEN1, HFSEN2, HFSEN3 and HFSEN4), and collagen coated blended MEH-PPV:PCL electrospun meshes (CSEN1, CSEN2, CSEN3 and CSEN4). White arrows show neuronal cell bodies with at least one neurite formed. Red arrows represent neurons with long branched neurites and/or growth cones. Inset

of SEN1 shows confocal images of stained PC12 cells cultured on collagen-coated cover slip for 7 days.

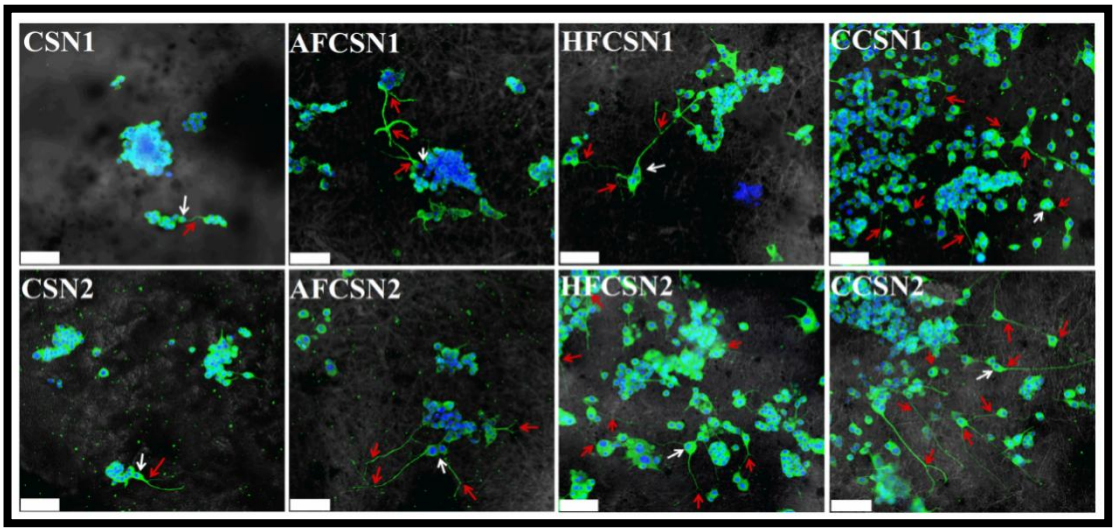

Figure 6.32. Immunolabelling of beta (III) tubulin in differentiated PC12 cells with DAPI stained nuclei after 7 days of culture on non-functionalized core-sheath electrospun meshes (CSN1 & CSN2), APTES functionalized core-sheath electrospun meshes (AFCSN1 & AFCSN2), 1,6-Hexanediamine functionalized core-sheath electrospun meshes (HFCSN1 & HFCSN2) and collagen coated core-sheath electrospun meshes (CCSN1 & CCSN2). White arrows show neuronal cell bodies with at least one neurite formed. Red arrows represent neurons with long branched neurites and/or growth cones.

The beta (III) tubulin protein staining confirms differentiation of the PC12 cells, particularly on APTES functionalized, 1,6-Hexanediamine functionalized and collagen coated electrospun meshes (both blended and core-sheath structured nanofibers) [**Figure 6.31**]. Staining can be visualized all through the cell bodies and neurites formed on uncoated electrospun meshes [AFSEN1, AFSEN2, AFSEN3, AFSEN4, HFSEN1, HFSEN2, HFSEN3, and HFSEN4 of **Figure 6.31**; AFCSN1, AFCSN2, HFCSN1 and HFCSN2 of **Figure 6.32**] and coated electrospun meshes [CSEN1, CSEN2, CSEN3 and CSEN4 of **Figure 6.31**; CCSN11, and CCSN2 of **Figure 6.32**].

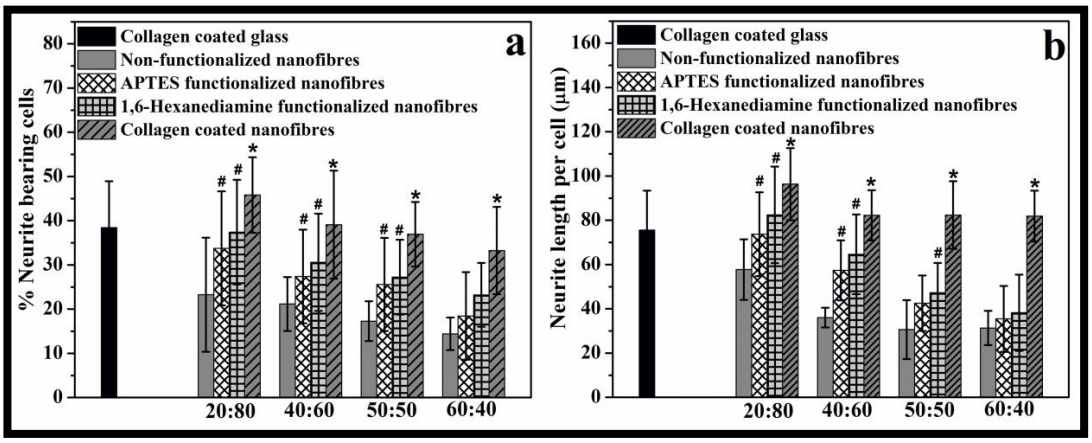

Figure 6.33. Quantitative analysis of formation and outgrowth in terms of (a) percentage of neurite-bearing cells and (b) neurite length per cell on the non-functionalized, APTES functionalized, 1,6-Hexanediamine functionalized and collagen coated blended MEH-PPV:PCL electrospun meshes along with collagen-coated glass. * and # indicate statistically significant difference from the non-functionalized electrospun meshes at $p \leq 0.01$and $p \leq 0.05$, respectively.

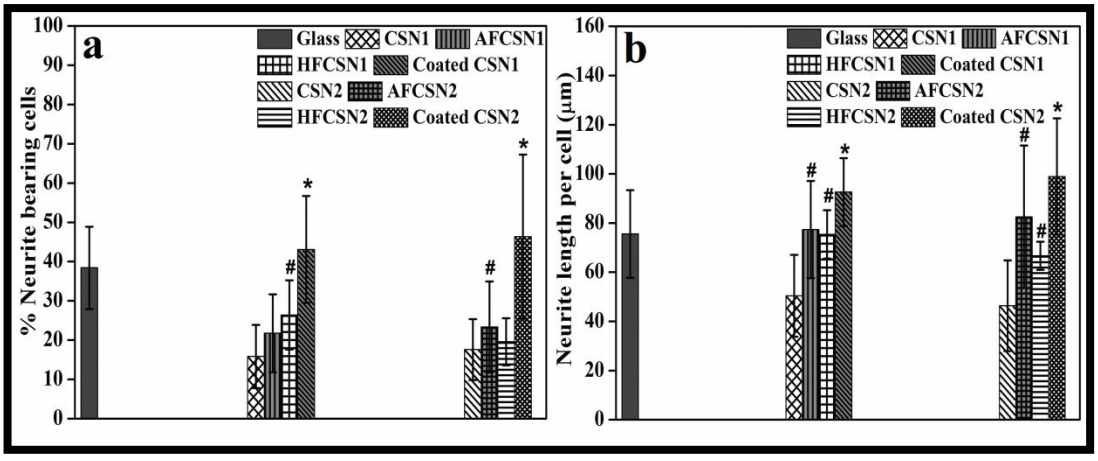

Figure 6.34. Quantitative analysis of neurite formation and outgrowth in terms of (a) percentage of neurite-bearing cells and (b) neurite length per cell on the non-functionalized, APTES functionalized, 1,6-Hexanediamine functionalized and collagen coated core-sheath MEH-PPV:PCL electrospun meshes along with collagen-coated glass. * and # indicate statistically significant difference from the non-functionalized electrospun meshes at $p \leq 0.01$and $p \leq 0.05$, respectively.

Beta (III) tubulin labeling indicated consistent neuronal morphology for the differentiated PC12 cells on all the coated electrospun meshes and glass cover slips [Inset of SEN1 in **Figure 6.31**] as compared to the uncoated electrospun meshes. The majority of the differentiated PC12 cells on the coated electrospun meshes demonstrate neuronal characteristics with long neurites with or without branches of varying complexity, round somas of variable size and many growth cones [CSEN1, CSEN2, CSEN3 and CSEN4 of **Figure 6.31**; CCSN1 and CCSN2 of **Figure 6.32**]. The APTES functionalized meshes (AFSEN1, AFSEN2, AFSEN3, AFSEN4, AFCSN1 and AFCSN2) and 1,6-Hexanedimaine functionalized meshes (HFSEN1, HFSEN2, HFSEN3, HFSEN4, HFCSN1 and HFCSN2) also support differentiation of PC12 cells with neuronal characteristics, however, the extent of neurite formation, outgrowth or branching is not consistent when compared to that of collagen coated meshes [**Figure 6.31 (& Figure 6.32**]. In contrast, cells on uncoated non-functionalized meshes (SEN1, SEN2, SEN3, SEN4, CSN1 and CSN2) form clusters with very poor & short or no neurite formation with few or no branches and growth cones [**Figure 6.31 (& Figure 6.32**].

Quantitative analysis of beta (III) tubulin immunochemistry results were performed using ImageJ software for cell counting and measurement of neurite outgrowth. Adherent cell number was counted as the total number of cells in 3 fields of view for each of three repeat samples per mesh type. Representative confocal images suggest PC12 cells formed neurite on all the electrospun meshes, however, on pristine electrospun meshes (non-functionalized and not coated with collagen I) neurite formation is very poor and collagen-coated meshes were appeared to be the best scaffold for PC12 differentiation [**Figure 6.31 & Figure 6.32**]. This is due to poor cell attachment on the pristine meshes. Cell numbers counted from DAPI-stained nuclei of the confocal images acquired at four quarters of each sample (n=3) reveal poor cell attachment on pristine SEN1 (24 ± 3 per image), SEN2 (21 ± 10 per image), SEN3 (12 ± 6 per image), SEN4 (17 ± 8 per image), CSN1 (43 ± 24 per image) and CSN2 (42 ± 17 per image) as compared to AFSEN1 (92 ± 17 per image), AFSEN2 (57 ± 23 per image), AFSEN3 (53 ± 21 per image), AFSEN4 (61 ± 19 per image), AFCSN1 (87 ± 24 per image), AFCSN2 (65 ± 20 per image), HFSEN1 (117 ± 33 per image), HFSEN2 (105 ± 27 per image), HFSEN3 (93 ± 18 per image), HFSEN4 (50 ± 24 per image), HFCSN1 (76 ± 16 per image), HFCSN2 (78 ± 34 per image), collagen

coated SEN1, i.e., CSEN1 (190 ± 26 per image), collagen coated SEN2,i.e. CSEN2 (181 ± 31 per image), collagen coated SEN3, i.e., CSEN3 (184 ± 45 per image), collagen coated SEN4, i.e., CSEN4 (144 ± 37 per image), collagen coated CSN1, i.e., CCSN1 (194 ± 23 per image) and collagen coated CSN2, i.e., CCSN2 (203 ± 54 per image). Surface functionalized electrospun meshes demonstrate better cell attachment than that on the pristine (non-functionalized and not coated with collagen I) meshes and this difference has been found to be statistically significant at $p \leq 0.05$ from one-way analysis of variance (ANOVA). The difference of cell attachment on collagen-coated electrospun meshes is also statistically significant at $p \leq 0.01$ to pristine meshes indicating their potential for neural tissue engineering applications. Moreover, the differences in cell numbers on the functionalized meshes (AFSEN1, HFSEN1, AFCSN1, HFCSN1, AFCSN2, and HFCSN2) and collagen coated meshes (CSEN1, CCSN1, and CCSN2) with nanofibers of comparatively larger diameter are statistically significant when compared to the functionalized meshes (AFSEN3, HFSEN3, AFSEN4, and HFSEN4) and collagen coated meshes (CSEN3 and CSEN4) with the smallest nanofiber diameter ($p \leq 0.01$).

At least 400 cells and 250 neurites were analyzed for quantitative analysis of neurite formation and neurite outgrowth. Due to poor attachment of PC12 cells on uncoated electrospun meshes, the number of cells analyzed was not more than 150-200 per substrate and accordingly, the number of neurites is also more than 100. The length of a neurite during this analysis is considered only when it is longer than the length of two cell bodies [155, 324]. The quantitative analysis results for neurite formation and outgrowth are displayed in **Figure 6.33** (for blended electrospun meshes) and **Figure 6.34** (for core-sheath electrospun meshes). For both blended and core-sheath electrospun meshes, quantitative analysis of beta (III) tubulin immunochemistry results showed that significantly higher neurite formation and longer neurite growth on collagen-coated electrospun meshes ($p \leq 0.01$) than the pristine meshes. The percentage of cells that formed neurite and neurite length per cell (for cells that possess at least one neurite) on CSEN1 (46 ± 9% and 96 ± 16 μm, N=557, m=332), CSEN2 (40 ± 12% and 83 ± 11 μm, N=524, m=284), CSEN3 (37 ± 7% and 82 ± 20 μm, N=489, m=265), CSEN4 (34 ± 10% and 78 ± 12 μm, N=494, m=271), CCSN1 (43 ± 14% and 93 ± 15 μm, N=542, m=346) and CCSN2 (46±20% and 99 ± 24 μm, N=628, m=324) are significantly higher than those on pristine SEN1

(23 ± 12% and 57 ± 14 μm, N=194, m=63), SEN2 (21 ± 6% and 36 ± 5 μm, N=168, m=31), SEN3 (17 ± 5% and 30 ± 13 μm, N=156, m=23), SEN4 (14 ± 5% and 31 ± 8 μm, N=132, m=21), CSN1 (16 ± 8% and 50 ± 17 μm, N=178, m=51) and CSN2 (18 ± 8% and 46 ± 19 μm, N=172, m=45), at $p \leq 0.01$, where 'N' and 'm' are number of cells and number of neurites analysed, respectively [**Figure 6.33 & Figure 6.34**]. Similarly, the differentiated PC12 cells appear to form more and longer neurites on AFSEN1 (33 ± 13% and 73 ± 19 μm, N=544, m=291), AFSEN2 (27 ± 11% and 57 ± 14 μm, N=434, m=261), AFSEN3 (25 ± 12% and 43 ± 13 μm, N=456, m=273), AFSEN4 (19 ± 10% and 36 ± 15 μm, N=458, m=253), AFCSN1 (22 ± 10% and 77 ± 20 μm, N=485, m=287), AFCSN2 (25 ± 10% and 82 ± 29 μm, N=422, m=262), HFSEN1 (37 ± 12% and 75 ± 10 μm, N=532, m=317), HFSEN2 (31 ± 11% and 75 ± 10 μm, N=473, m=283), HFSEN3 (26 ± 8% and 75 ± 10 μm, N=438, m=276), HFSEN4 (23 ± 7% and 75 ± 10 μm, N=421, m=259), HFCSN1 (27 ± 9% and 75 ± 10 μm, N=437, m=278) and HFCSN2 (20 ± 6% and 67 ± 11 μm, N=443, m=263) than those on their non-functionalized counterparts [**Figure 6.33 & Figure 6.34**]. This difference is statistically significant at $p \leq 0.05$. Moreover, cellular activity of PC12 cells is not significantly different on APTES and 1, 6-Hexanediamine functionalized meshes. It seemed that surface functionalization by both the functionalizing agents affected equally on PC12 attachment and their differentiation in presence of NGF. The overall observations suggest that both APTES and 1, 6-Hexane-diamine functionalized meshes provided more PC12 cell attachment and their differentiation to sympathetic neurons than pristine meshes. The better PC12 attachment followed by their cellular activities like neurite formation and outgrowth on surface functionalized meshes can be attributed to the incorporation of amine functionality on their surfaces enabling them to achieve favorable electrostatic interactions with negatively charged cell surfaces for cellular adhesion and differentiation. This proposition is in good agreement with previous reports [416, 436, 483]. These results further reveal that fibre features along with collagen coating on scaffold provide a better platform for neurite formation and neurite outgrowth since PC12 cells form more neurites with longer outgrowth on collagen-coated electrospun meshes than those on collagen-coated glass (38 ± 10% and 75 ± 17 μm) ($p \leq 0.01$). It was has been also noted that MEH-PPV in the sheath of the core-sheath nanofibers do not have any adverse effect

on neurite formation and outgrowth, which is in agreement with the biocompatibility of MEH-PPV in blend and core-shell format shown as discussed in previous sections.

6.5.2 PC12 cell attachment

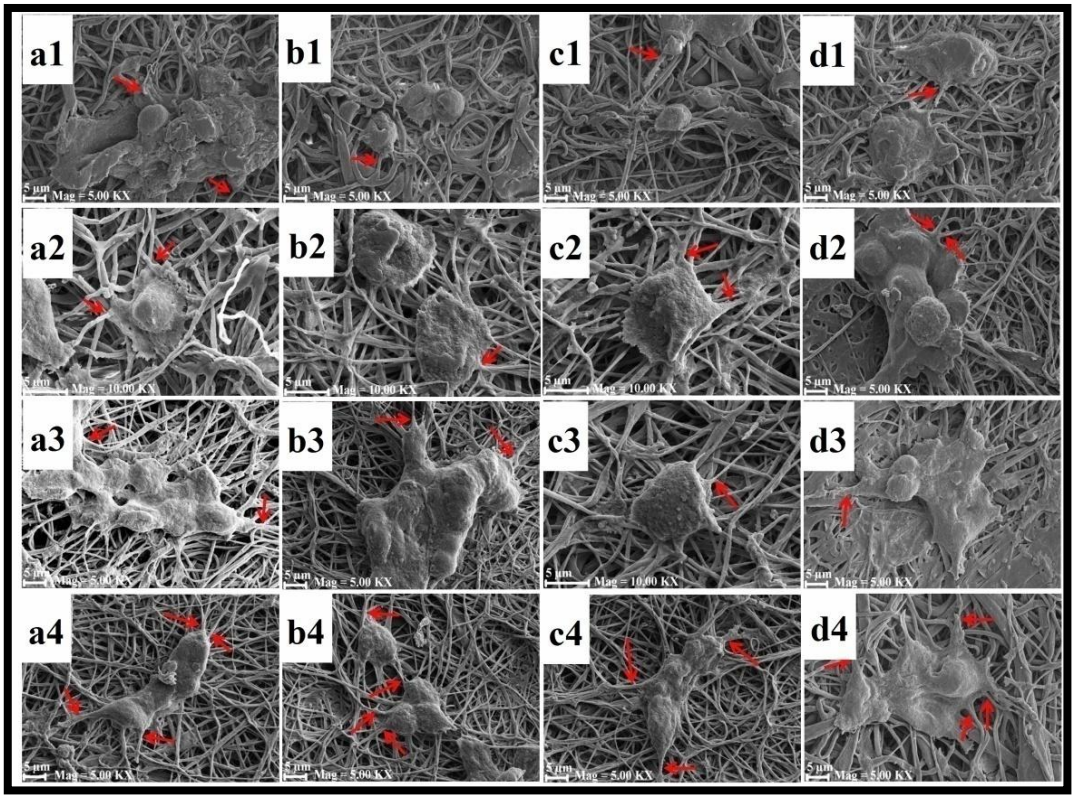

Figure 6.35. Scanning electron micrographs of PC12 cells after 7 days cultured on SEN1 (a1), SEN2 (b1), SEN3 (c1), SEN4 (d1), AFSEN1 (a2), AFSEN2 (b2), AFSEN3 (c2), AFSEN4 (d2), HFSEN1 (a3), HFSEN2 (b3), HFSEN3 (c3), HFSEN4 (d3), CSEN1 (a4), CSEN2 (b4), CSEN3 (c4) and CSEN4 (d4). Red arrows show neurite projections on different electrospun meshes. Scale bar = 5 μm.

To further confirm the attachment of PC12 cells and to study its morphology on various electrospun meshes, SEM was performed after 7 days of culture. The SEM images of PC12 cells cultured on various blended electrospun meshes and core-sheath electrospun meshes are shown in **Figure 6.35** and **Figure 6.36**, respectively, confirming the results of the immunocytochemistry.

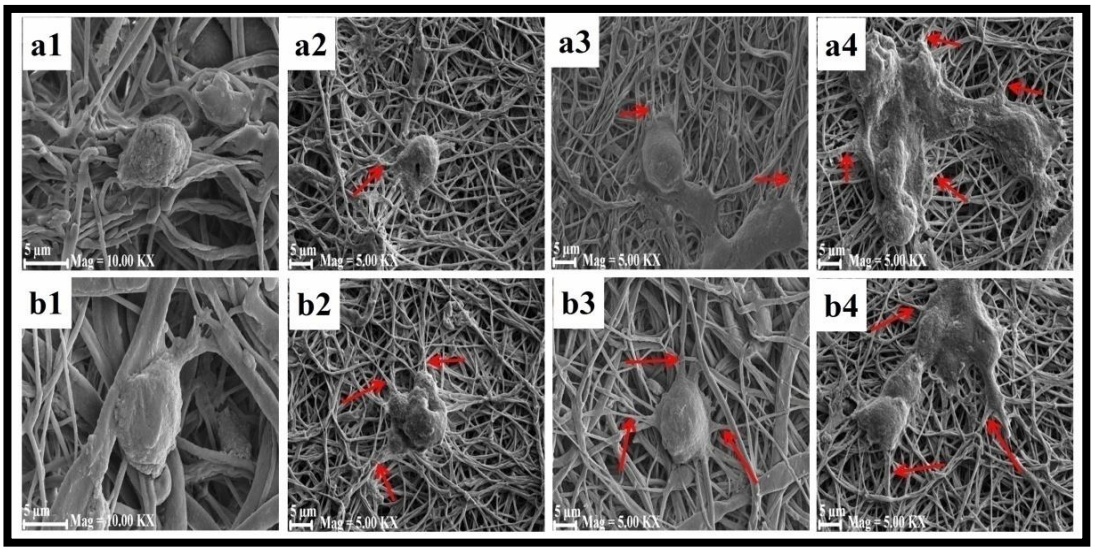

Figure 6.36. Scanning electron micrographs of PC12 cells after 7 days cultured on pristine CSN1 (a1), CSN2 (b1), AFCSN1 (a2), AFCSN2 (b2), HFCSN1 (a3), HFCSN2 (b3), CCSN1 (a4) and CCSN2 (b4). Red arrows show neurite projections on different electrospun meshes. Scale bar = 5 μm.

SEM images confirm improved cell attachment on collagen-coated electrospun meshes than functionalized meshes, whilst poor cell attachment on pristine electrospun meshes. All the electrospun meshes coated with collagen I demonstrate better cell adhesion and morphology as compared to poor cell attachment on non-functionalized electrospun meshes. PC12 cells on the functionalized and collages coated electrospun meshes (both blended and core-sheath lectrospun meshes) appeared to make contact with multiple fibres and formed more elliptical morphologies with neurite projection [**Figure 6.35 (a2-d4) & Figure 6.36 (a2-b4)**]. The cells on uncoated electrospun meshes appeared to be spherical [**Figure 6.35 (a1-d1) & Figure 6.36 (a1-b1)**] with distorted morphology and with few or no neurite projections. Although not quantified, it is also noteworthy to be noted that PC12 cells cultured on the surface functionalized meshes were bigger in size than that of cultured on pristine and collagen-coated meshes. The results confirm good cell attachment on collagen-coated electrospun meshes along with good neurite projections in random directions indicating the potential of the coated electrospun meshes for neural tissue engineering applications. The moderate enhancement in PC12 attachment and neurite

projections on surface functionalized conductive meshes also indicated the potential of these meshes for nerve repair.

6.6 Electrical stimulation of PC12 cells

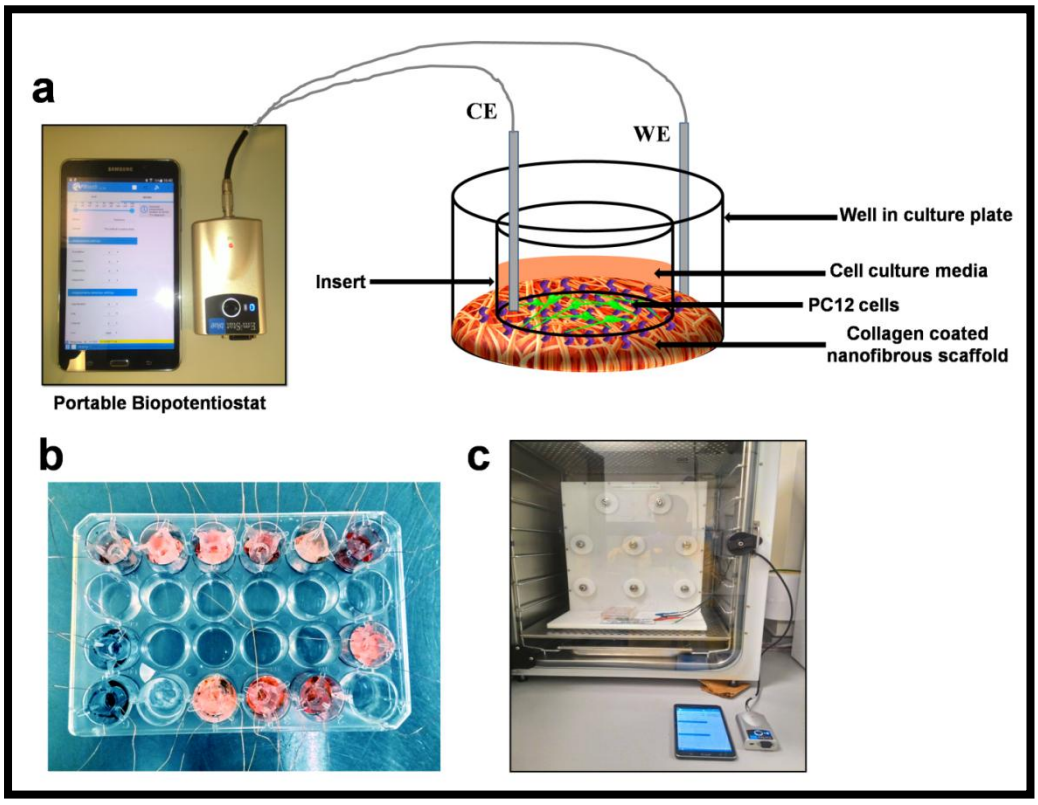

Figure 6.37. (a) Schematic illustration of the electrical stimulation experiment using a custom made electrical stimulation set up ; (b) photograph of self made cell culture plate with different electrospun MEH-PPV:PCL meshes (orange colur) fixed on it for electrical stimulation experiment; (c) photograph of the electrical stimulation experiment in situ.

To explore the potential the different amine functionalized and collagen-coated electrospun meshes (both blended and core-sheath electrospun meshes) for electrical stimulation of nerve cells as smart biomaterial scaffolds for axonal regeneration in damaged nerve, electrical stimulation of differentiated PC12 cells was accomplished as shown in the schematic in **Figure 6.37**. The effect of electrical stimulation of PC12 cells through the conductive electrospun meshes has been assessed in terms of quantitative analysis of the percentage of neurite-bearing cells, neurite per cell, neurite length per cell and median neurite lengths from the confocal images of beta

(III) tubulin stained PC12 cells on electrospun meshes as shown in **Figure 6.38** (functionalized and collagen coated blended electrospun meshes) and **Figure 6.39** (functionalized and collagen coated core-sheath electrospun meshes). PC12 cells were also cultured on electrospun meshes in the homemade electrical stimulation set up without electrical stimulation for comparison [**Figure 6.37**].

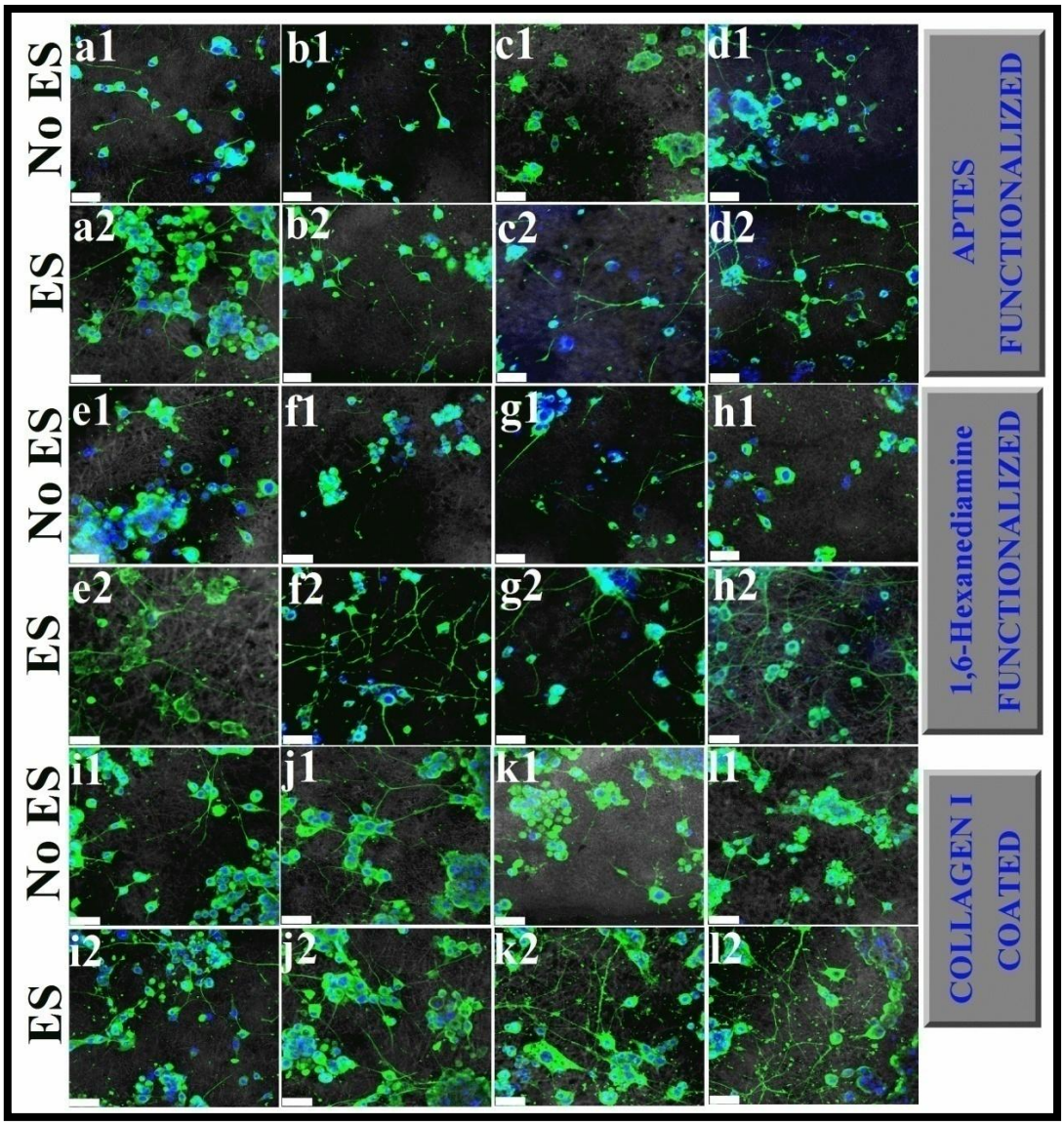

Figure 6.38. Confocal images with phase contrast overlay of beta (III) tubulin immunostained PC12 cells cultured for 7 days on the various blended electrospun meshes under no electrical stimulation (a1-AFSEN1, b1-AFSEN2, c1-AFSEN3, d1-AFSEN4, e1-HFSEN1, f1-HFSEN2, g1-HFSEN3, h1-HFSEN4, i1-CSEN1, j1-CSEN2, k1-CSEN3 and l1-CSEN4) and under electrical stimulation of 500 mV/cm for 2h/day (a2-AFSEN1, b2-AFSEN2, c2-AFSEN3, d2-AFSEN4, e2-HFSEN1, f2-

HFSEN2, g2-HFSEN3, h2-HFSEN4, i2-CSEN1, j2-CSEN2, k2-CSEN3 and l2-CSEN4) [Scale bar = 75 μm].

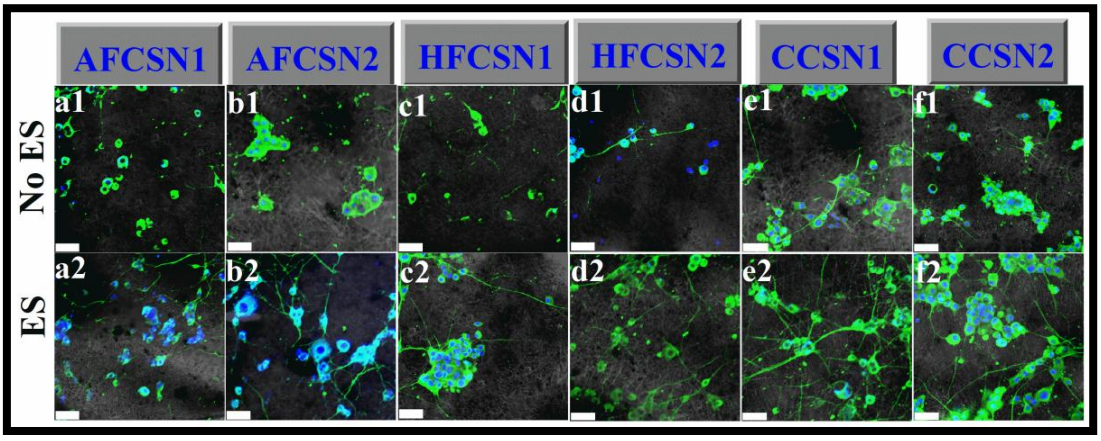

Figure 6.39. Confocal images with phase contrast overlay of beta (III) tubulin immunostained PC12 cells cultured for 7 days on the various core-sheath electrospun meshes under no electrical stimulation (a1-AFCSN1, b1-ACSN2, c1-HFCSN1, d1-HFCSN2, e1-CCSN1, f1-CCSN2) and under electrical stimulation of 500 mV/cm for 2h/day (a2-AFCSN1, b2-AFCSN2, c2-HFCSN1, d2-HFCSN2, e2-CCSN1, f2-CCSN2) [Scale bar = 75 μm].

Results indicate that the presence of MEH-PPV in the blend and core-shell formulations increases the % neurite bearing cells and the neurite length per cell following 2 h growth under electrical stimulation. The most significant effects have been seen when MEH-PPV was used in the core-sheath electrospun mesh for stimulation and was present to increase conductivity in the outer sheath. The healthy neuronal characteristics of differentiated PC12 cells including greater neurite formation, branching, and longer axonal growth have been observed on electrically stimulated cells [**Figure 6.38 (a2-l2) & Figure 6.39 (a2-f2)**] as compared to unstimulated cells [**Figure 6.38 (a1-l1) & Figure 6.39 (a1-f1)**]. The APTES and 1,6-Hexanediamine functionalized blended and core-sheath electrospun meshes, which demonstrate lower neurite formation and outgrowth under no electrical stimulation [**Figure 6.38 (a2-h2) & Figure 6.39 (a2,b2,d2,e2)**], display remarkable enhancement in the neurite formation and outgrowth under 2h of electrical stimulation at 500 mV/cm per day for three consecutive days [**Figure 6.38 (a1-h1) & Figure 6.39**

(a1,b1,d1,e1)]. The effectiveness of electrical stimulation on neuronal growth of PC12 cells has been accomplished through the quantitative analysis of the confocal images of beta (III) tubulin stained cells using ImageJ software and has been discussed below.

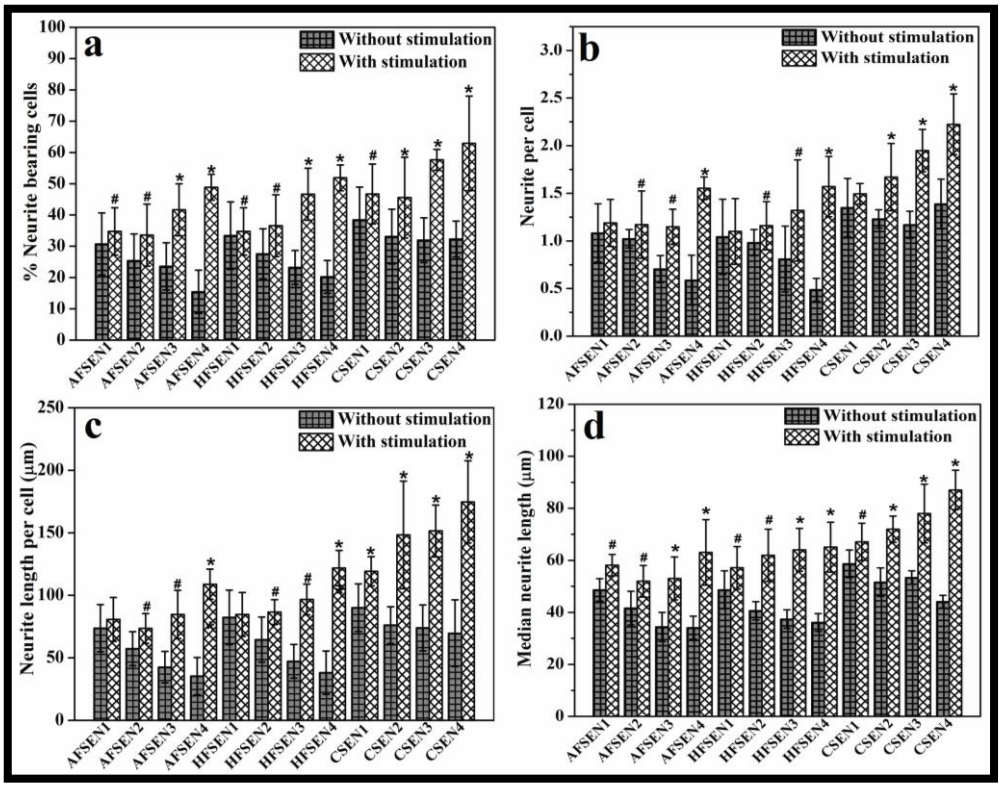

Figure 6.40. (a) Percentage of neurite bearing cells, (b) Neurite per cell, (c) Neurite length per cell and (d) Median neurite length of differentiated PC12 cells on the various blended MEH-PPV:PCL electrospun meshes without electrical stimulation and with electrical stimulation. Data were Mean ± S.D. * and $^{\#}$ indicate statistical significance difference from unstimulated PC12 cells at $p \leq 0.01$ and $p \leq 0.05$, respectively.

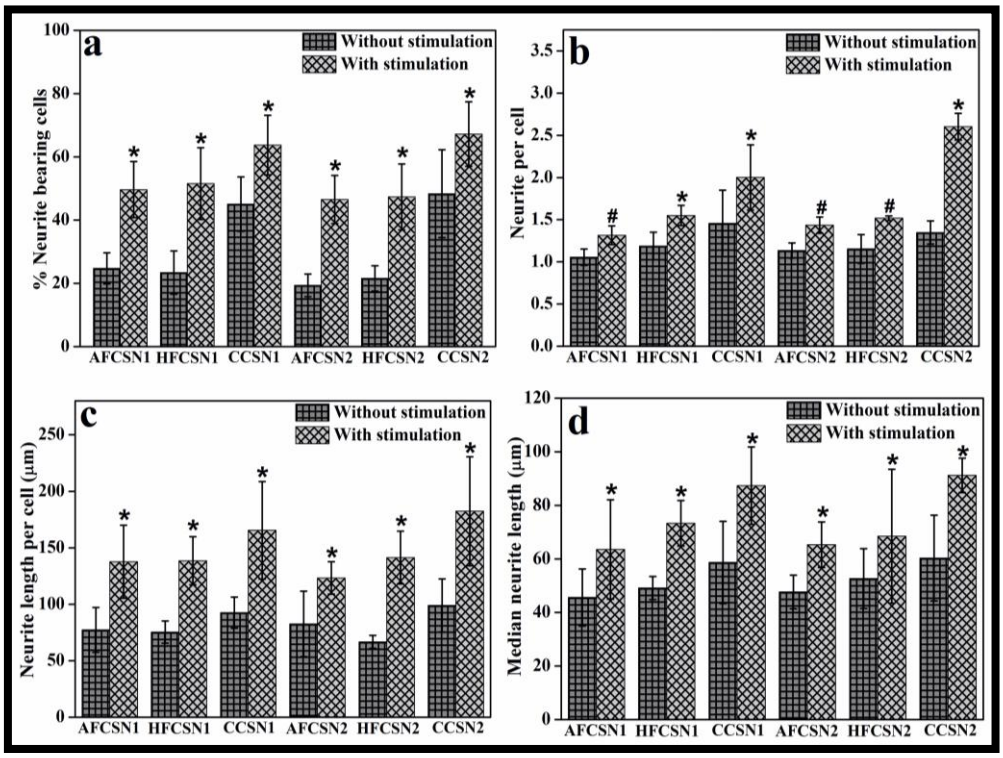

Figure 6.41. (a) Percentage of neurite bearing cells, (b) Neurite per cell, (c) Neurite length per cell and (d) Median neurite length of differentiated PC12 cells on the various core-sheath MEH-PPV:PCL electrospun meshes above without electrical stimulation and with electrical stimulation. Data were Mean ± S.D. * and # indicate statistical significance difference from unstimulated PC12 cells at $p \leq 0.01$ and $p \leq 0.05$, respectively.

Quantitative analysis indicates that enhanced neurite formation on electrically stimulated PC12 cells on AFSEN1(35 ± 8%, N=477, m=201), AFSEN2 (34 ± 10%, N=403, m=188), AFSEN3 (42 ± 9%, N=419, m=218), AFSEN4 (47 ± 5%, N=436, m=212), AFCSN1 (50 ± 8%, N=373, m=198), AFCSN2 (51 ± 7%, N=385, m=207), HFSEN1 (35 ± 9%, N=457, m=206), HFSEN2 (37 ± 10%, N=396, m=190), HFSEN3 (47 ± 8%, N=432, m=203), HFSEN4 (48 ± 6%, N=397, m=218), HFCSN1 (52 ± 12%, N=324, m=201), HFCSN2 (50± 11%, N=418, m=228), CSEN1 (47 ± 11%, N=473, m=324), CSEN2 (46 ± 13%, N=445, m=394), CSEN3 (58 ± 3%, N=409, m=341), CSEN4 (63 ± 14%, N=438, m=378), CCSN1 (64 ± 10%, N=545, m=590) and CCSN2 (67 ± 11%, N=476, m=514) than unstimulated PC12 cells on AFSEN1(31 ± 10%, N=414, m=181), AFSEN2 (25 ± 9%, N=327, m=158), AFSEN3

(24 ± 8%, N=356, m=173), AFSEN4 (15 ± 7%, N=372, m=153), AFCSN1 (25 ± 5%, N=342, m=172), AFCSN2 (19±4%, N=361, m=153), HFSEN1 (34 ± 10%, N=418, m=187), HFSEN2 (28 ± 8%, N=353, m=156), HFSEN3 (23 ± 6%, N=318, m=154), HFSEN4 (20 ± 6%, N=313, m=157), HFCSN1 (23 ± 7%, N=409, m=193), HFCSN2 (22± 5%, N=352, m=166), CSEN1 (39 ± 11%, N=481, m=232), CSEN2 (33 ± 9%, N=461, m=203), CSEN3 (32 ± 7%, N=519, m=219), CSEN4 (32 ± 6%, N=502, m=222), CCSN1 (45 ± 9%, N=604, m=450) and CCSN2 (48 ± 14%, N=566, m=331), where 'N' and 'm' denote number of cells and number of neurites analyzed [**Figure 6.40 (a) & Figure 6.41 (a)**]. The differences in the number of cells that formed neurites on AFSEN3, AFSEN4, HFSEN3, HFSEN4, CSEN2, CSEN3, CSEN4, CCSN11 and CCSN2, under electrical stimulation, are statistically significant at $p \leq 0.01$ from their unstimulated counterparts [**Figure 6.40 (a) & Figure 6.41 (a)**]. Besides, the extent of neurite formation on AFSEN1, AFSEN2, HFSEN1, HFSEN2 and CSEN1, under electrical stimulation, is statistically different from that on the same scaffolds under no electrical stimulation at $p \leq 0.05$ [**Figure 6.40 (a) & Figure 6.41 (a)**]. This observation is further evident from the fact that the PC12 cells under electrical stimulation form more neurites per cell than that formed per unstimulated cells. Analysis of neurites per cell indicate that single stimulated cell has 1.18 (AFSEN1), 1.17 (AFSEN2), 1.14 (AFSEN3), 1.55 (AFSEN4), 1.32 (AFCSN1), 1.34 (AFCSN2), 1.10 (HFSEN1), 1.16 (HFSEN2), 1.32 (HFSEN3), 1.57 (HFSEN4), 1.35 (HFCSN1), 1.42 (HFCSN2), 1.49 (CSEN1), 1.67 (CSEN2), 1.94 (CSEN3), 2.22 (CSEN4), 2.01 (CCSN1) and 2.61 (CCSN2) neurites on average as compared to 1.08 (AFSEN1), 1.02 (AFSEN2), 0.7 (AFSEN3), 0.58 (AFSEN4), 1.05 (AFCSN1), 1.13 (AFCSN2), 1.04 (HFSEN1), 0.98 (HFSEN2), 0.81 (HFSEN3), 0.48 (HFSEN4), 1.19 (HFCSN1), 1.15 (HFCSN2), 1.35 (CSEN1), 1.23 (CSEN2), 1.17 (CSEN3), 1.38 (CSEN4), 1.46 (CCSN1) and 1.34 (CCSN2) neurites per unstimulated cells [**Figure 6.40 (b) & Figure 6.41 (b)**]. However, the number of neurites per stimulated cell has been found to be statistically different only for AFSEN4, HFSEN4, CSEN2, CSEN3, CSEN4, CCSN1 and CCSN2 from that formed per unstimulated cell at $p \leq 0.01$, while the same is statistically significant at $p \leq 0.05$ for AFSEN2, AFSEN3, HFSEN2 and HFSEN3, except AFSEN1, HFSEN1 and CSEN1 [**Figure 6.40 (b) & Figure 6.41 (b)**].

Quantitative analysis to determine the effect of electric field on axonal growth reveals that the neurite lengths per cell and median neurite lengths of electrically stimulated cells are more on AFSEN1 (80 ± 18 and 58 ± 4 μm), AFSEN2 (74 ± 12 and 52 ± 6 μm), AFSEN3 (85 ± 20 and 53 ± 8 μm), AFSEN4 (109 ± 12 and 63 ± 13 μm), AFCSN1 (138 ± 32 and 63 ± 18 μm), AFCSN2 (124 ± 14 and 65 ± 8 μm), HFSEN1 (85 ± 17 and 57 ± 8 μm), HFSEN2 (87 ± 10 and 62 ± 10 μm), HFSEN3 (97 ± 12 and 64 ± 8 μm), HFSEN4 (122 ± 14 and 65 ± 10 μm), HFCSN1 (138 ± 21 and 73 ± 9 μm), HFCSN2 (141 ± 23 and 68 ± 25 μm), CSEN1 (120 ± 11 and 67 ± 7 μm), CSEN2 (148 ± 43 and 72 ± 6 μm), CSEN3 (152 ± 43 and 78 ± 11 μm), CSEN4 (174 ± 32 and 87 ± 8 μm), CCSN1 (165 ± 43 and 87 ± 14 μm) and CCSN2 (182 ± 48 and 91 ± 6 μm) than those of unstimulated cells on AFSEN1 (73 ± 17 and 48 ± 5 μm), AFSEN2 (57 ± 14 and 42 ± 7 μm), AFSEN3 (42 ± 12 and 34 ± 6 μm), AFSEN4 (37 ± 14 and 34 ± 4 μm), AFCSN1 (77 ± 20 and 46 ± 11 μm), AFCSN2 (83 ± 29 and 72 ± 6 μm), HFSEN1 (82 ± 21 and 48 ± 7 μm), HFSEN2 (65 ± 18 and 41 ± 4 μm), HFSEN3 (47 ± 14 and 37 ± 4 μm), HFSEN4 (39 ± 13 and 36 ± 4 μm), HFCSN1 (75 ± 10 and 49 ± 5 μm), HFCSN2 (70 ± 7 and 48 ± 6 μm), CSEN1 (90 ± 21 and 58 ± 6 μm), CSEN2 (76 ± 15 and 52 ± 6 μm), CSEN3 (74 ± 18 and 53 ± 3 μm), CSEN4 (69 ± 26 and 44 ± 2 μm), CCSN1 (93 ± 14 and 59 ± 15 μm) and CCSN2 (99 ± 24 and 62 ± 16 μm) [**Figure 6.40 (c & d) & Figure 6.41 (c & d)]**. The differences in neurite length per stimulated cell on AFSEN4, AFCSN1, HFCSN2, HFSEN4, HFCSN1, HFCSN2, CSEN1, CSEN2, CSEN3, CSEN4, CCSN1 and CCSN2 are statistically significant at $p \leq 0.01$ from that of the stimulated cells on the same scaffolds. Furthermore, the neurite lengths per stimulated cell on AFSEN2, AFSEN3, HFSEN2 and HFSEN3 are also significantly different from that of the unstimulated cells at $p \leq 0.05$. However, there are no significant differences in neurite length per cell for AFSEN1 and HFSEN1. The median neurite lengths on AFSEN3, AFSEN4, AFCSN1, AFCSN2, HFSEN3, HFSEN4, HFCSN1, HFCSN2, CSEN2, CSEN3, CSEN4, CCSN1 and CCSN2, under electrical stimulation, are significant at $p \leq 0.01$ from those on the same scaffolds without electrical stimulation. Besides, such differences are significant at $p \leq 0.05$ for AFSEN1, AFSEN2, HFSEN1, HFSEN2 and CSEN1.

Turning onto the analysis of the impact of surface functionalization and collagen coating on neurite formation and outgrowth under electrical stimulation, it

has been demonstrated from one way ANOVA analysis that electrical stimulation through both the blended and core-sheath electrospun meshes in conjunction with collagen coating exhibits significant contribution towards the excellent neurite formation and axonal growth of the differentiated PC12 cells when compared to that grown on the surface functionalized electrospun meshes (both blended and core-sheath electrospun meshes) under the same condition ($p \leq 0.01$). There are no significant differences observed in neurite formation and outgrowth of electrically stimulated PC12 cells grown on APTES and 1,6-Hexanediamine functionalized electrospun meshes, whether those have been prepared by simple electrospinning or coaxial electrospinning process at $\alpha = 0.01$ or 0.05 ($p=0.12$). In addition, one way ANOVA analysis demonstrate significantly improved neurite formation and neurite outgrowth on the functionalized and collagen coated core-sheath electrospun meshes under electrical stimulation than those on the functionalized and collagen coated blended electrospun meshes ($p \leq 0.01$). The results suggest that electrically conductive MEH-PPV present on the sheath of core-sheath nanofibers provide better option for electrical stimulation of PC12 cells within safe limit than the blended electrospun meshes prepared by simple electrospinning process from a blend of MEH-PPV and PCL, mixed at different volume ratio. This proposition has been further supported by the significant differences in neurite formation and outgrowth on the functionalized and collagen coated blended electrospun meshes ($p \leq 0.01$) under constant electrical stimulation, as demonstrated by one way ANOVA analysis. It has been observed that under application of a constant electric field of 500 mV/cm for 2h/day, the parameters such as neurite bearing cells, neurite per cell, neurite length per cell and median neurite length on amine functionalized SEN4 (AFSEN4 and HFSEN4) and collagen coated SEN4 (CSEN4), having highest concentration of MEH-PPV in the blend, are significantly greater than those on AFSEN1, AFSEN2, AFSEN3, HFSEN1, HFSEN2, HFSEN3, CSEN1, CSEN2, CSEN3 and CSEN4 ($p \leq 0.01$), which have relatively lower concentration of MEH-PPV than different variations of SEN4 [**Figure 6.40 (a-d)**].

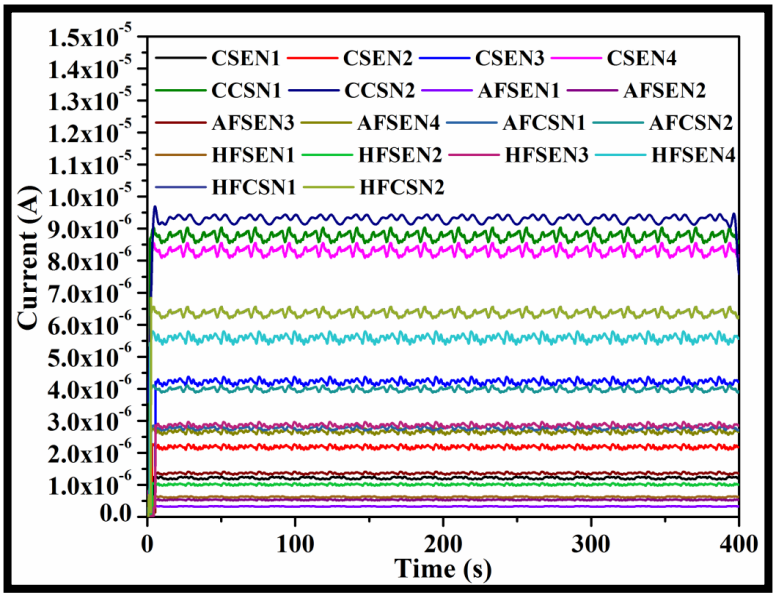

Figure 6.42. Current signal recorded (upto 400 s) during electrical stimulation of PC12 cells through various blended MEH-PPV:PCL electrospun meshes and core-sheath MEH-PPV:PCL electrospun meshes under a constant potential of 500 mV/cm for 2 h, applied in chronoamperometric technique in pulsed mode (pulse duration 1 ms).

The parameters to define the degree of neurite formation and outgrowth such as neurite bearing cells, neurite length per cell, median neurite length and neurite per cell under electrical stimulation increase with increasing concentration of conductive MEH-PPV in the case of blended nanofibers produced by simple electrospinning process. Similarly, the core-sheath electrospun meshes with $FeCl_3$ doped MEH-PPV as sheath material have better conductive properties than the electrospun meshes prepared by simple electrospinning process and showed more neurite formation and longer neurite outgrowth over all ($p \leq 0.01$). These observations reveal that electrospun meshes having lower sheet resistance and higher density of free charge carriers (particularly, CSN1, CSN2 & SEN4) showed more neurite formation and longer neurite outgrowth under electrical stimulation [**Section 6.2.4**]. The current signal applied by chronoamperometric method in pulse mode for stimulation of PC12 cells through different electrospun meshes were shown in **Figure 6.42**. The degree of neurite formation and outgrowth increases almost systematically with increase in current signal (upto 8-9 μA) through the conductive electrospun scaffolds during

stimulation (CCSN2>CCSN1>CSEN4>HFCSN2>HFCSN1>HFSEN4>CSEN3>AFCSN2>HFSEN3>AFCSN1>AFSEN4>AFSEN3>CSEN2>CSEN1>HFSEN2>AFSEN2>HFSEN1>AFSEN1) [**Figure 6.42**]. Moreover, it has been also observed that surface functionalized meshes reveal enhanced PC12 adhesion under electrical stimulation as the number of cells available for analysis under electrical stimulation has been found to be greater than that available for analysis under no electrical stimulation. Our finding is in agreement with the fact reported by Zhang *et al.* that more neurite-bearing PC12 cells were observed below 10 μA and promotion of neurite formation diminished as currents increased above 10 μA [485]. Under the application of electrical stimulation, the availability of free charge carriers in the conductive electrospun meshes (more in CSN1, CSN2 and SEN4) results more charge-transport between the scaffold and the cell membrane. This charge-transport process changes the resting membrane potential of differentiated PC12 cells. Under constant electrical potential for 2 h, the cell membrane undergoes an intensity-dependent depolarization resulting action potential, which is responsible for axonal growth. This change in cell membrane potential is also believed to activate growth-controlling transport processes across the plasma membrane and cause redistribution of cytoplasmic materials [120, 196, 415-417]. According to Patel *et al.*, electrical stimulation causes electrophoretic accumulation of surface molecules on the working electrode (scaffold). All these are likely to be responsible for longer neurite growth or cell-substratum adhesion [415].

6.7 Summary

We have shown the synthesis and optimization of electrically conductive, porous, mechanically strong and bioactive MEH-PPV:PCL nanofibers with blended form with variation in the volume ratio of the constituents by simple electrospinning process and core-sheath morphology with variation in diameter with varying flow rate by coaxial electrospinning along with post-synthesis surface functionalization using APTES and 1,6-Hexanediamine. We have carried out physico-chemical and biological characterization of the blended electrospun meshes and confirmed that increasing concentrations of MEH-PPV in a PCL blend improve biocompatibility of MEH-PPV alone, reduced nanofibrillar diameter and tensile strength but increased conductivity and subsequent differentiated neuronal growth characteristics on cell seeded surface functionalized and collagen coated meshes under electrical stimulation. We have shown that a core-shell synthesis route with MEH-PPV shell increased fibrillar

diameter and tensile strength characteristics whilst improving conductive growth stimulus characteristics for neurite outgrowth on surface functionalized and collagen coated meshes. Electrospun meshes prepared by simple electrospinning and coaxial electrospinning demonstrate enhanced 3T3 fibroblasts adhesion, spreading, proliferation and migration after surface functionalization by APTES and 1,6-Hexanediamine, separartely. Briefly, the synergistic effect of nanofiber feature, surface functionalization of electrospun MEH-PPV based materials and electrical stimulation in neuronal growth has been investigated for potential application of these materials in neural tissue engineering. The major results of this study have been summarized below.

Coaxial electrospinning produces uniform nanofibers with larger diameters and better conductive and mechanical properties than the electrospun nanofibers produced by simple electrospinning process as confirmed by SEM, TEM and tensile strength measurements. The core-sheath electrospun meshes exhibit improved *I-V* characteristics than the nanofibers prepared by simple electrospinning of blend of MEH-PPV and PCL, which can be attributed to the presence of conductive $FeCl_3$ doped MEH-PPV in the sheath of core-sheath nanofibers. No significant changes in conductive properties of the electrospun meshes after surface functionalization by APTES and 1,6-Hexanediamine have been noticed indicating that functionalization has been performed without much affecting the conductive properties of MEH-PPV. Analysis of *I-V* measurements results reveal that all the core-sheath nanofibers with $FeCl_3$ doped MEH-PPV in the shell of the core-sheath nanofibers and all the blended electrospun nanofibers with higher MEH-PPV concentration possess lower values of critical voltage (V_c) due to higher density of free charge carriers *(p)*. Furthermore, the non-linear behaviour of the *I-V* characteristics of all the electrospun meshes has been explained with the help of *Kaiser Equation*, which also demonstrate easier hopping of charge carriers in the electrospun core-sheath nanofibers and blended electrospun nanofibers with higher MEH-PPV concentration.

The highly porous electrospun meshes exhibit higher mechanical properties such stiffness constant *(E)* and ultimate tensile strength (UTS). Surface functionalized meshes demonstrate enhanced stiffness constant *(E)* and UTS as compared to their non-functionalized counterparts due to the cross-linking between the polymers chains occurred after functionalization. The core-sheath nanofibers are mechanically strong

when compared to the nanofibers prepared from a blend of MEH-PPV and PCL, which is assigned to larger diameter of the core-sheath fibers.

Stability test results suggest that all the electrospun nanofibers have been found to be stable enough in physiological solution due to the non-degradable nature of MEH-PPV and slow degradation rate of PCL, where fibrillar diameter and sheet resistance (R_s) have been found almost constant after 45 days incubation in PBS (pH=7.4). However, surface functionalization electrospun meshes demonstrate slightly enhanced weight loss as compared to that of the non-functionalized electrospun meshes without affecting the conductive properties.

FTIR and XPS show successful incorporation of amine functionality after surface functionalization by APTES and 1,6-Hexanediamine. XPS results support higher doping levels in the core-sheath nanofibers leading to better conductive properties which also confirm the presence of MEH-PPV in sheath.

Hemolysis activity assay demonstrates the improved hemocompatibility of the 1,6-Hexanediamine functionalized electrospun meshes than that of the APTES functionalized and non-functionalized electrospun meshes. The surface functionalized electrospun meshes showed significant improvement in viability of 3T3 fibroblasts and a neuronal model rat pheochromocytoma 12 (PC12) cells as confirmed by MTS proliferation assay. Live-dead assay and cell adhesion study by SEM demonstrate that 3T3 fibroblasts adhered, spread, proliferated and migrated well on the surface functionalized electrospun meshes as compared to non-functionalized meshes. It is worthy to be noted that surface functionalization by 1,6-Hexanedamine slightly more effective in the modulation of 3T3 cell behavior, however, this effect is not significant with PC12 cells. PC12 cells were found to adhere and differentiated well on collagen I coated meshes followed by surface functionalized meshes as compared to non-functionalized meshes, as demonstrated by beta (III) tubulin immunochemistry and cell adhesion test (by SEM).

Electrical stimulation of PC12 cells through the electrically conductive electrospun nanofibers under the potential of 500 mV/cm for 2 h for 3 consecutive days demonstrates significant improvement in neurite formation and outgrowth than the unstimulated PC12 cells. However, the effect of electrical stimulation on PC12 cells cultured on core-sheath nanofibrous meshes has been found to be more prominent owing to their better conductive properties than the nanofibers prepared from blended MEH-PPV with PCL. It is also noteworthy that surface amination of the

core-sheath nanofibers along with electrical stimulation comes out as a promising scaffold to replace the need of coating the scaffold with costly biomolecules such as collagen, laminin, fibronectin etc.

The results indicate the potential of MEH-PPV based biomaterial scaffolds in fabrication of nerve guidance channels to bridge the gap for directive growth of damaged nerves in peripheral nervous system (PNS) as an alternative to conventional nerve grafts such as autograft and allograft. It also provides a new additional option using CPs in neural tissue engineering applications as an alternative to widely investigated PPy, PAni and PEDOT. The poor solubility exhibited by these polymers inhibits nanofibril formation by electrospinning whereas MEH-PPV with PCL has been shown to produce nanofibrous scaffolds with varying morphology for potential neuronal stimulation.